Three-dimensional mapping of electrical propagation in the heart: experimental and mathematical model based analysis

Darren Anthony Hooks

Supervised by Dr Ian J. LeGrice, Associate Professor Bruce H. Smaill, and Professor Peter J. Hunter

A thesis submitted in partial fulfilment of the requirements

for the degree of Doctor of Philosophy

Bioengineering Research Group
Departments of Physiology &
Engineering Science
The University of Auckland
New Zealand

November 2001

The University of Auckland

Thesis Consent Form

This thesis may be consulted for the purpose of research or private study provided that due acknowledgement is made where appropriate and that the author's permission is obtained before any material from the thesis is published.

I agree that the University of Auckland Library may make a copy of this thesis for supply to the collection of another prescribed library on request from that Library; and

1. I agree that this thesis may be photocopied for supply to any person in accordance with the provisions of Section 56 of the Copyright Act 1994

Or

2. This thesis may not be photocopied other than to supply a copy for the collection of another prescribed library

(Strike out 1 or 2)

Signed:…….

Date:……

To my parents

Abstract

In this thesis, mathematical modelling, instrumentation development and experimental studies are combined to effect two advances in the study of cardiac electrophysiology. Firstly, we outline a method that will enable microstructural information gathered using extended confocal microscopy to be incorporated into whole heart models of electrical propagation. A structured finite element technique is used to solve the bidomain equations on a realistic representation of myocardial architecture. The effects of intercellular gaps in the tissue on electrical propagation, and the response of myocardium to defibrillation-strength shocks, are examined. It is shown that myocardium is not a transversely isotropic electrical medium as has been widely assumed. Instead it is most appropriately viewed as orthotropic, with different electrical properties assigned to three microstructurally defined orthogonal axes. It is also concluded that the intercellular tissue gaps provide a likely mechanism for activation of a critical volume of tissue during defibrillation.

Secondly, a novel imaging system is presented which enables transmembrane potentials to be recorded simultaneously at multiple sites through the heart wall. While heart surface optical recordings of transmembrane potential have been widely used in studies of normal and pathological heart rhythms, it is difficult to obtain information about propagation processes deep within the heart wall. A probe constructed from optical fibers is used to deliver excitation light to and collect fluorescence from 6 tissue sites each spaced 1mm apart. For individual channels, excitation is provided by the 488nm line of a water-cooled argon-ion laser, while the fluorescence of a voltage-sensitive dye is split at 600nm and imaged into separate photodiodes for later signal ratioing. The system has been sucessfully used to record intramural action potentials in the isolated rabbit heart and is designed to be easily expandable to accommodate multiple optical probes. The fluorescence collection volume of the fibre-optic probe has been characterised in rhodamine solution using two-photon microscopy. These data are compared with corresponding results obtained with two flat cleaved optical fibres in solution and in stained heart tissue. The results demonstrate that the effective collection depth in cardiac

tissue for our optrodes was 100µm, but that this is dependent on the type of optical fibre used to fabricate the optrode.

These techniques developed in this research provide a basis for more systematic study of the initiation and termination of reentrant electrical activity in the heart. Future research that builds on the original findings presented in this thesis is discussed.

Preface

The research outlined in this thesis comprises two major bodies of original work: (i) development and analysis of a bidomain model of electrical propagation which incorporates accurate data about the microscopic architecture of the heart, (ii) development and characterisation of a novel experimental technique for measuring transmembrane potential at multiple sites through the heart wall. This work involved three seperate studies which form the basis of manuscripts that are currently published, submitted, or in preparation for peer reviewed scientific journals. These are:

D.A. Hooks, K.A. Tomlinson, S. Marsden, I.J. LeGrice, A.J. Pullan, B.H. Smaill, and P.J. Hunter. Cardiac microstructure: implications for electrical propagation and defibrillating the heart. *In preparation for Circulation Research.*

D.A. Hooks, I.J. LeGrice, J.D. Harvey, B.H. Smaill. 2001. Intramural multisite recording of transmembrane potential in the heart. *Biophys. J.* 81:2671-2680.

D.A. Hooks, D.A. Wardle, C. Soeller, I.J. LeGrice, B.H. Smaill, M. Cannell. Spatial point response function of fibre optic probes determined by two-photon microscopy. *In preparation for Applied Optics.*

These three manuscripts form the basis of chapters 2, 3 and 4, in this thesis. Additional explanation and background information has been added in these chapters where this was judged to be necessary. The work involved inputs from a number of people and this is acknowledged in the authorship of the manuscripts. Further detail of the valuable assistance which I have received is provided below. However, I was the principal investigator in each of the three studies, coordinating and directing most aspects of the work.

Chapter 1 provides an overview of the general field addressed in this thesis. *Chapter 2* presents the mathematical formulation of the bidomain equations used in a discontinuous structural model of electrical propagation in the heart. Results of the model in both propagated and shock induced cases are examined. The transmural volume image of the left ventricle was obtained by Young et al. (1988) and initial segmentation was done by Scott Marsden as part of a final year project in Engineering Science. Together with Dr. Karl Tomlinson, we developed a finite element technique that enabled structural discontinuities to be represented as no flux boundaries within the context of a bidomain formulation. Results of the model in both propagated and shock induced cases are examined. *Chapter 3* presents a novel method which utilises the voltage-sensitive dye di-4-ANEPPS, and a novel recording system and probe *(optrode)* to make simultaneous measurements of transmembrane potential through wall of the rabbit left ventricle. The optrode concept was developed by myself, and Dr. David Wardle of the Physics Department had input toward the overall design of the optical system. *Chapter 4* follows with characterisations of the depth of fluorescence collection of the optrode and other fibre based probes. Dr. Cristian Soeller gave instruction and advice on the two-photon microscope. Finally, future directions for all aspects of the work are presented in *Chapter 5*.

Acknowledgements

There are many people to thank for their encouragement toward, and input into, this body of work. Firstly, a huge thank you to my supervisors, Ian LeGrice, Bruce Smaill, and Peter Hunter. Ian, you have been always supportive, knowledgeable, and have cleared the way ahead numerous times. You always made time to fit in those experiments, even in a busy schedule. Thank you Bruce for all your help, tireless efforts in reviewing manuscripts, and your always useful insights. You have taught me a great deal. Also, Peter, it has been great taking advantage of the infrastructure that you have built up at Bioengineering. You steered the modelling in the right directions, and were always ready to give help. I look forward to working with you all in the future.

I wish to thank in particular David Wardle for endless support and help toward the optical parts of the thesis. Your enthusiasm and wisdom was always much appreciated. The optical set-up and methods also benefited greatly from the wisdom and support of Christian Soeller, John Harvey, and Mark Cannell. Also, thanks to Karl Tomlinson, for his excellent assistance in the modelling part of the thesis, along with the great help of Scott Marsden in coding the model. From the beginning, I enjoyed the company of Socrates Dokos, who could always offer insights on just about any topic, and Gregory Sands who has kept a watchful eye on proceedings throughout. Thanks Adele for providing new inspiration to the lab, and Dean Tai for tiding us over with beautifully constructed optrodes.

I have enjoyed the company of many fellow students and postdocs working at Bioengineering over the past year – you have certainly been better company than the basement dark lab had to offer! Those who have helped me along the way numerous times include Andrew Taberner, Carey Stevens, David Nickerson, Martin Buist, Richard Boyes, Warren Hedley, Kevin Augenstein, and Leo Cheng. To the graphics guys – Richard Cristie and Shane Blackett – thanks for all those tips, hope my figures do you justice. Thanks to Andrew Cantell for always being around to help with those computer

geeky things. A big thanks also to the UnEmap team – David Bullivant, Duane Malcolm, and Jim Williams - I'm sure I gave you a few late nights, and tormented you often enough with phone calls from the lab. You can now rest. Thanks to Rob Kirton for telling it like it is. I hope you shake the hell out of those trabs and can write up soon. Good luck also to Marie Ward – you can't be far off, and I promise I wont leave a mess around the weigh balance ever again. To Arthur Burgess, I know you are pleased I have finished … no need to cry ooohh noooo again. I am training Adele in the ways of nagging though – watch out.

Finally, to all those outside of work who have walked with me along this PhD path. Goddy, Albert, Sally, Karla, Brian – I have to say you have not really shown much interest in the content of the research, but have always been most concerned as to when it will finish. Well, it has. Yes Brian, I know I said I only had 2 weeks to go about this time last year.

Most of all, thank you to my parents to whom this thesis is dedicated. They have never faltered in their support for whatever I turn my hand to. Thanks Mum for hurrying me along at the end (sorry I couldn't have beaten you though), and thanks Dad for always understanding more than any other non-scientist!

Contents

Chapter 1 **Introduction** **1**

1.1 Background 2

1.1.1 Cellular Electrophysiology 2

1.1.2 A Functional Anatomy of Cardiac Electrical Propagation 4

1.1.3 Cardiac Arrhythmia, Fibrillation and Defibrillation 7

1.1.4 Cardiac Mapping 9

1.1.5 Computer Modelling 15

1.2 Summary 20

Chapter 2 **Influence of the discontinuous laminar organization of cardiomyocytes on electrical propagation and response to cardioversion** **21**

Abstract 21

2.1 Introduction 22

2.2 Methods 24

2.2.1 Structural Representation 24

2.2.2 Discontinuous bidomain model formulation 26

2.2.3 Part I: Propagated response 34

2.2.4 Part II: Shock-induced response 34

2.2.5 Model parameters 36

2.3 Results 37

2.3.1 Part I 37

2.3.2 Part II 42

2.4 Discussion 43

2.4.1 Implications for Propagation 43

2.4.2 Implications for Defibrillation 48

2.4.3 Limitations of the study 50
2.4.4 Conclusions 52

Chapter 3 **Intramural multisite recording of transmembrane potential in the heart** **53**

Abstract 53
3.1 Introduction 54
3.2 Methods 55
3.2.1 Optics 55
3.2.2 Optrode 58
3.2.3 Optical Fibres 59
3.2.4 Signal acquisition and processing 60
3.2.5 Experimental preparation 62
3.3 Results 63
3.3.1 System Efficiencies 63
3.3.2 Fibre bundle alignment 64
3.3.3 Fluorescence collection characteristics of the optrode 64
3.3.4 Directionality of the optrode 67
3.3.5 System noise 69
3.3.6 Animal experiments 71
3.4 Discussion 74
3.4.1 Limitations of the present study and recording technique 75
3.4.2 Extracellular potential mapping 76
3.4.3 Optical mapping of transmembrane potential on the heart surfaces 77
3.4.4 Optical mapping with fibre optics 77

Chapter 4 **Spatial point response function of fibre optic probes determined by two-photon microscopy** **79**

Abstract 79
4.1 Introduction 80
4.2 Theory 81

4.3 The 2P method for determining the SPRF 82
4.4 Validation of the 2P method 84
4.5 SPRF of two fibre types in solution and tissue 86
4.6 SPRF of the optrode in solution 86
4.7 Discussion 89

Chapter 5 **Future Directions** **93**

Abstract 93
5.1 Microstructurally based propagation modelling 94
5.1.1 Validation of the model results of Chapter 2 96
5.2 Optical Mapping System 101
5.2.1 Beyond the heart - wider applications of a multi-optrode system 101
5.2.1.1 Electrical activity of the brain 101
5.2.1.2 Other fluorescence indicators 103
5.2.1.3 Blood flow measurements 103
5.2.2 Further system characterisation 104
5.2.3 Technical issues of a multi-optrode recording system 106
5.2.3.1 Methods of efficient and uniform coupling of excitation light into optrode fibres 107
5.2.3.2 Systems for detection 112
5.2.3.3 Systems for illumination 119
5.3 Conclusions 120

Appendix **CMISS Command Files** **121**

References **127**

List of Figures

1.1 Basis of the cardiac action potential…….. 3
1.2 Myocyte connectivity……..… 5
1.3 Model of the development of re-entrant arrhythmia……. 8
1.4 Activation modelling on the Auckland Heart Model…… 18

2.1 Laminar architecture of porcine ventricular myocardium..…….. 23
2.2 Structural representation of cleavage plane geometries.…….. 25
2.3 The discontinuous finite element method……..… 33
2.4 Extension of the rat image volume…… 35
2.5 Comparison of models…….. 38
2.6 Extracellular potential signals……... 41
2.7 Response to cardioversion……. 45
2.8 Response to cardioversion – discontinuous model…… 46
2.9 Transmembrane potential profile comparison – discontinuous and continuous models…….. 46

3.1 The optical recording system…… 56
3.2 The optrode…… 58
3.3 Coupling of the laser beam into the tissue fibre bundle…… 65
3.4 Depth collection characteristics of optrode in rhodamine……. 66
3.5 Optrode directionality characterisation …… 68
3.6 Bevelled fibre fluorescence collection directionality …….…….. 69
3.7 Noise characteristics of the system……... 70
3.8 Membrane potential-dependent signals……. 71
3.9 Effects of 2,3-BDM on the signals…… 72
3.10 Decay of signal quality with time ……. 73

4.1 Schematic of the two-photon microscopy set-up ……. 83
4.2 Two-photon image reconstruction …… 85
4.3 Validation of the two-photon method……... 87
4.4 SPRF for two types of fibre in solution and tissue……..…….. 88
4.5 Determination of SPRF for a F-MCB-T fibre ptrode……... 90

5.1 Imaging system schematic……. 96
5.2 Locations of extracellular electrodes within myocardium…… 97
5.3 Activation maps following point stimulation…… 98
5.4 Effect of laminar architecture of myocytes on propagation…….. 99
5.5 Extracellular potential recordings……. 100
5.6 Spiral wave propagation and the effects of optrode insertion……... 106
5.7 The flattened beam profile…… 107
5.8 Coupling of laser beam into a bundle of 61 optical fibres…… 109
5.9 The fibre-splitter cascade……... 110
5.10 Fibre to fibre imaging system…… 111
5.11 Membrane potential-dependent optical signal…….. 112
5.12 Current versus voltage relationship for photodiodes……. 117
5.13 Comparison of optically recorded action potentials…….. 119

Chapter 1

Introduction

The rhythmic and synchronised contraction of the heart is crucial in sustaining life. A typical heart beat is driven by a wave of excitation which starts at the sinoatrial node, and propagates through the atria, atrioventricular node, Purkinje system, and, finally, through the bulk of the ventricles. In almost all deaths, the last few moments of life are characterised by a lack of spatial coherence in this propagating wave. The study of electrical propagation in the heart is motivated by three main concerns. Firstly, we seek to understand how organised electrical propagation is sustained in the healthy heart. Secondly, we wish to explore how disorganised propagation may eventuate. Finally, we aim to deduce methods of restoring disorganised propagation to its organised form.

Within this context, two distinct approaches have been used to study cardiac electrical propagation. Computer modelling and experimental cardiac mapping are both used to reconstruct the three-dimensional spread of electrical activation in the heart. Computer modelling relies on high speed computers to solve continuum mechanics problems over the geometry of the heart. On the other hand, cardiac mapping records time varying potentials simultaneously at different locations on the heart. Both approaches are necessarily informed by *a priori* knowledge of cardiac cellular electrophysiology and of anatomic factors that affect electrical propagation at a more macroscopic level.

The remainder of this chapter provides a brief overview of the field and outlines the objectives of the research described in this thesis.

1.1 Background

1.1.1 Cellular Electrophysiology

The basis of the cardiac action potential is outlined in a number of monographs and reviews. For a more detailed account, the reader is referred to Zipes & Jalife (2000). At any instant in time, the potential difference across the cardiac cell membrane is determined by intra- and extra-cellular concentrations of potassium, sodium and calcium ions and on the status of specialised channels that carry these ions across the cell membrane. For the great majority of heart muscle cells that are not spontaneously active, the potassium ion channel I_{K1} contributes most of the transmembrane permeability at rest. Hence resting membrane potential is approximately -90mV, which is close to the potassium equilibrium potential E_K. At the potassium equilibrium potential the outward potassium ion flux due to the chemical potential gradient exactly matches an inward potassium ion flux due to an electrical potential gradient.

Cellular activation is triggered when the membrane potential is reduced rapidly to around -50mV. The voltage-dependent activation gates of fast sodium channels open allowing sodium ions to enter the cell and depolarize the cell membrane (Fig. 1.1). This process is terminated within a few milliseconds with inactivation of the sodium channels. Depolarization is sustained throughout the prolonged plateau phase of the action potential because the efflux of potassium ions is reduced (the permeability of I_{K1} decreases with depolarization) and is offset by inward current flux due to the voltage-dependent opening of slow L-type calcium channels. The activation and inactivation gates of the sodium channels cannot be reset until membrane potential falls below -50mV and therefore the cardiac cell is absolutely refractory (cannot be reactivated) during the plateau phase of the action potential. Repolarization is initiated by the late opening of a further potassium ion channel I_K, the delayed rectifier (Fig. 1.1). With the progressive resetting of sodium

channels during repolarization activation becomes possible and the cell is said to be relatively refractory.

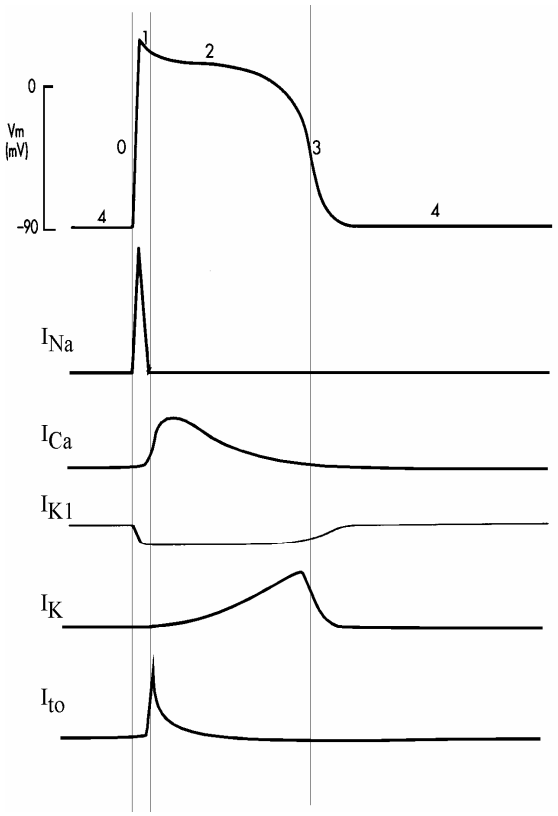

Fig. 1.1 *Basis of the cardiac action potential*

Top trace: a typical ventricular cardiac action potential, with the five phases of the action potential labelled. The upstroke is phase 0, notch is phase 1, plateau is phase 2, repolarization is phase 3, and resting potential is phase 4. The lower traces depict the time courses of the major ionic currents involved in the development of the action potential. An increase in the ionic current is shown as an upward deflection in the traces, regardless of the membrane current direction.

[Based on: Sperelakis, N. and R.O. Banks. 1996. Essentials of Physiology, 2nd edn. Little Brown & Co. p253]

1.1.2 A Functional Anatomy of Cardiac Electrical Propagation

Issues relating to the propagation of electrical activity in the heart will now be reviewed a little more fully. Again the reader is referred to a source such as Zipes & Jalife (2000) for a more detailed outline.

Under normal circumstances, cardiac activation is driven by the automatic activity of a cluster of specialised cells within the sino-atrial (SA) node, located on the upper surface of the right atrium close to its junction with the superior vena cava. These pacemaker cells have a low density of I_{K1} channels and exhibit an unstable membrane potential during diastole, thought to be due to the interaction of the delayed rectifier I_K, an inward leak of sodium ions via the I_f channel, activation of T-type calcium channels, and net inward charge movement associated with activation of the membrane sodium/calcium exchanger (Lipsius et al., 2001). SA nodal cells are excited when threshold is reached and L-type calcium channels are opened.

Activation spreads through the atrial chambers at a velocity of 1-2 m/s. The fibrous atrio-ventricular (AV) valve ring prevents direct electrical coupling between atrial and ventricular myocardium; the only pathway for ventricular activation is via the atrio-ventricular (AV) node and AV bundle. Decremental conduction markedly delays propagation through the AV node and bundle. Electrical activation then spreads swiftly through the interventricular septum via the His bundle, and right and left bundle branches, while the endocardial surfaces of right and left ventricles are excited in a rapid and co-ordinated fashion through the Purkinje fibre network. This specialised conduction system is characterised by relatively rapid propagation at 5-10 m/s, while activation spreads through working ventricular muscle at a velocity of 1-2 m/s.

Activation is spread between heart cells via gap junctions. These microchannels connect adjacent cardiomyocytes end-to-end, or side-to-side, and act as low-resistance electrical pathways, allowing diffusion of the ions involved in the activation process from cell-to-cell. Gap junction communication between cells allows the heart to function in a co-

ordinated fashion, and has given rise to the term “syncytium” (Latin: *syn*, together; *cytium*, cell) to describe both the structure and function of the heart. In the healthy heart, the spread of activation across cells is typically thought of, and modelled as, a continuous process. Gap junctional resistance is lumped together with cytosolic resistance to give a continuous intracellular space, and an associated intracellular resistance. In various states of ageing, disease, and ischaemia it is recognised that activation spreads throughout the ventricles in a much more discontinuous fashion, largely due to the uncoupling of cardiomyocytes via gap junction block or degradation (Spach and Dolber, 1986; Ellis et al., 1995).

Cardiomyocytes vary in shape and size, depending on their location and function in the heart. Atrial myocytes are typically elliptical and measure about 20x6µm. Purkinje cells are significantly larger, at about 200x40µm. Ventricular myocytes are long and narrow in shape and typically of dimension 100x15µm. As depicted in Fig. 1.2, ventricular

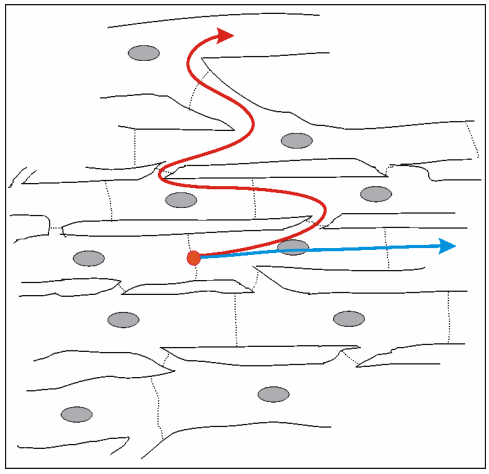

Fig. 1.2 *Myocyte connectivity*
Schematic drawing of the connectivity of a group of cardiomyocytes. Cell-to-cell communication is via gap junctions located on intercalated discs shown as light grey lines. Electrical propagation from a point stimulus is faster along cells (blue line) than across them (red line).

myocytes form networks in which the cell axes at any point are aligned in a common direction. Within a group of connected cardiomyocytes, the elongated shape of the heart cell favours more rapid activation along the cell axis than transverse to it. This is due to the lower number of gap junctions per unit length that a wavefront must traverse in the direction of the cell axis, together with the circuitous path of diffusion that is required for a wavefront to travel transverse to the myocyte axis.

At most locations in the heart the dominant orientation of cardiomyocytes is visible with the naked eye. This orientation is often termed “fibre angle” (Streeter and Bassett, 1966) and has been meticulously measured at closely spaced points throughout the ventricles of the dog heart by LeGrice and co-workers (LeGrice, 1992). In a gross sense, fibres are oriented parallel to the endocardium and epicardium, and spiral around the heart. Fibre angle varies smoothly through the ventricular wall from around -75° below the circumference at the epicardial surface to +75° at the endocardial surface. Although cardiomyocytes were long thought to be uniformly coupled transverse to their longitudinal axis, recent research has shown that within the ventricles there are regular planes across which myocyte-to-myocyte connections are absent (LeGrice et al., 1995; Young et al., 1998). These so called “cleavage planes” reflect the organization of ventricular myocardium as a branching, “laminar” structure, in which the average thickness of cellular layers or "sheets" is 4-5 myocytes, or ~50μm.

It has been widely assumed that propagation of electrical activity in the ventricles is isotropic in the plane orthogonal to fibre direction and, under these circumstances, specification of fibre angle is sufficient to define the anisotropy of conduction velocity. (Frazier et al., 1988). However, this assumption is at odds with our current view of ventricular myocardium as structurally orthotropic. It seems reasonable to expect that activation perpendicular to myocardial layers across cleavage planes should be slower than activation transverse to the fibre direction within layers. In other words, we hypothesise orthogonal anisotropy of conduction velocity in the heart that reflects tissue microstructure. Structure-based electrical anisotropy of this kind could play a significant

role in the genesis of arrhythmia (see below), but the hypothesis has yet to be adequately addressed.

1.1.3 Cardiac Arrhythmia, Fibrillation and Defibrillation

Under normal circumstances, cardiac electrical activation is highly synchronised. There is co-ordinated activation of the cardiac chambers via the specialised conduction (Purkinje) system and the heart exhibits prolonged and spatially homogeneous refractory properties. A defect in the synchrony of activation or repolarization may alter cardiac rhythm (give rise to an arrhythmia). Re-entrant arrhythmias are a particularly important class of arrhythmia, in which the wavefront periodically re-enters previously excited tissue. Re-entry may lead to sustained tachycardia and complete degeneration of cardiac rhythm into fibrillation.

The concept of re-entrant electrical activation is associated with the propagation of a wavefront around some central obstacle. The nature of this obstacle leads to a classification of re-entry into *anatomic* or *functional* re-entry. Anatomic obstacles which may facilitate re-entry include blood vessels, infarct scars, or branches of the Purkinje system. In functional re-entry, the wavefront propagates around a central region of unexcited tissue which would nevertheless be activated during a normally propagated event. Various mechanisms for functional re-entry have been proposed, however current thinking centres on the spiral wave model of re-entry. Spiral waves are continuously rotating ‘spiral’ wavefronts. The centre of rotation is termed the spiral core, and whilst this region is excitable, it remains unexcited during spiral wave rotation, due to the high curvature of the wavefront at the spiral tip, which reduces the amount of current available to depolarize this region (Baxter, 1999). Spiral waves are observed in a number of excitable media, including slime moulds and the Belousov-Zhabotinsky reaction (Winfree et al., 1996). Three-dimensional spiral waves are termed “scroll” waves, and have cores which extend as lines (“filaments”) in space. These filaments may drift, anchor to structural discontinuities, enlarge, or shrink. Filaments may also fragment, giving rise to multiple daughter filaments (Gray, 1998). This process may lead to

multiple sustained re-entering wavefronts, or fibrillation, in which activation throughout the ventricles proceeds in a chaotic fashion, and coordination at the whole heart level is lost.

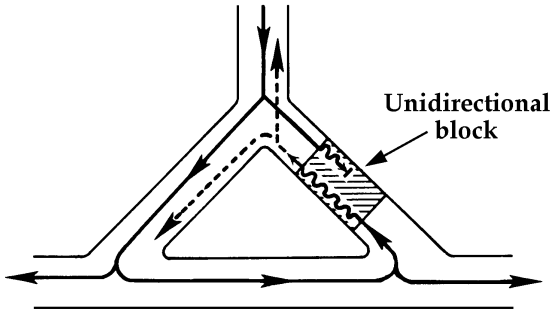

Fig. 1.3 *Model of the development of re-entrant arrhythmia*
A propagating wavefront enters from above the circuit. Propagation is blocked on the right limb of the circuit by an ischaemic (hatched) region, whilst propagation is safely transmitted down the left limb. The wavefront re-enters the top of the circuit following slow propagation through the ischaemic region.

Figure 1.3 shows a schematic model for the development of re-entry. In addition to a central obstacle, re-entrant arrhythmias require (i) a triggering event (ii) unidirectional block and (iii) an appropriate circuit length. The triggering event may be of varied origin. Automaticity may develop out of usually non-automatic tissue during ischaemia. For example, partial depolarization caused by ischaemia predisposes Purkinje fibres to automaticity due to a pacemaker current (Opie, 1998). Early and late after-depolarizations in ventricular myocytes due to long action potentials or excessive catecholamine levels may also act as a trigger event (Clancy and Rudy, 1999).

Unidirectional block may be caused by asymmetrically depressed conduction, which is common in diseased hearts. For example, infarct scars contain regions of sparsely

coupled cellular tracts, where conduction in one direction may be blocked due to current-to-load mismatches (Rohr et al., 1997).

For a re-entrant circuit to become established, it is necessary for any one region within the circuit to recover from the absolute refractory period before the wavefront may re-enter that region. The region of fully recovered tissue ahead of the wavefront is termed the "excitable gap". Reducing the excitable gap is one approach of anti-arrhythmic pharmacological therapy. A large excitable gap is facilitated by a long circuit length, or by slowed propagation through the circuit. There are many mechanisms by which propagation may be slowed. One of the most simple is ischaemia induced depolarization leading to partial inactivation of fast sodium channels within the circuit.

The most effective means of quickly restoring ordered activation to the heart during fibrillation is the application of a large potential gradient (~10V/cm) across the heart for a brief (~10ms) period. One of the earliest successful uses of such electrical defibrillation (cardioversion) was made by Claude Beck in 1947 at the Case Western Reserve University (Paradis et al., 1996). Today, the implantable cardioverter-defibrillator is recognised as one of the most important means for prevention of sudden cardiac death. However, the mechanisms by which a shock applied to the heart restores synchronous activation are still largely unknown. There is evidence that for defibrillation to be successful a large volume of tissue distant from the shock electrodes must be simultaneously reset (Trayanova, 1999). An understanding of how such "far-field" stimulation of tissue occurs is critical if the efficacy and efficiency of defibrillation is to be improved.

1.1.4 Cardiac Mapping

Electrical Mapping:

Experimental cardiac mapping may be defined as the discipline in which the spatio-temporal variation of electrical activity in the heart is reconstructed from potential

recordings. In many ways cardiac mapping is a mature field. It is rather sobering to realise that the first systematic mapping of activation on the dog ventricle was completed by Sir Thomas Lewis in 1915 (Shenasa et al., 1993). Moreover, as early as 1914, much of what we know about re-entrant propagation had already been published (Mines, 1914; Garrey, 1914). For instance, it had been shown that both unidirectional block and involvement of a critical mass of tissue were required for the development of re-entry, and that re-entry could occur without the involvement of an anatomical obstacle. Many of these early observations were made with no more sophisticated an instrument than the naked eye. Later, the mapping of extracellular potential waveforms on the heart began in earnest, forming the basis of cardiac electrical mapping. Many years were devoted to understanding and interpreting the extracellular action potential. Early on Lewis wrote the perceptive comment on the extracellular potential waveform: “There are deflections which result from arrival of the excitation process immediately beneath the contacts [electrode]; … there are also deflections which are yielded by the excitation wave, travelling in distant areas of muscle” (Lewis, 1915). In 1953, Durrer et al. were the first to use transmural plunge electrodes to reconstruct the activation sequence in isolated human hearts. Measurements were made from as many as 870 intramural terminals, which is heroic even in terms of current technologies. Earliest epicardial breakthrough of activation was shown to usually occur on the RV, above the insertion of the anterior papillary muscle, 20-25ms after the start of ventricular activity.

The first clear demonstration of functional re-entry came from Allessie et al. (1977) who used dense surface electrode arrays to map the spread of activation on the atrial surfaces. They introduced the “leading circle concept” of functional re-entry, in which a re-entrant circuit exists in the smallest possible pathway such that the wavefront is just able to excite relatively refractory tissue ahead of it.

During the late 1970s and early 1980s Spach and co-workers laid the foundations for the bidomain model of electrical propagation, by investigating the relationships between transmembrane and extracellular potentials (Spach et al., 1979). Moreover, the relationship between structural discontinuity such as age-induced side-to-side uncoupling

of myocytes, and extracellular potential measurements, was the subject of several studies (Spach et al., 1986).

The effect of fibre rotation through the ventricular wall on propagation was studied with dense plunge electrode arrays by Frazier et al. (1988). It was concluded that following point stimulation, activation isochrones were elliptical, with the major axes of the ellipses oriented along the mean fibre direction between the pacing site, and the recording plane. This is consistent with the assumption that conduction in myocardium is transversely isotropic.

Eighty years since the inception of cardiac electrical mapping, multisite recording of extracellular potential still forms the basis of most cardiac mapping both experimentally and clinically. Conventional electrical mapping techniques have a number of limitations however. Extracellular recordings reflect the integrated effects of ionic currents over a relative large volume of tissue. As such, distant electrical events are often difficult to distinguish from near events, and a combination of distant and near events leads to a fractionated extracellular electrogram in which the local activation time is difficult to discern. The timing of repolarization is also difficult to assess in extracellular recordings. Additional limitations arise from the requirement to limit tissue damage associated with high density plunge electrode arrays. Finally, extracellular potential cannot be recorded during a defibrillating shock because of the very high field strengths applied.

Optical Mapping:

Over the past ten years extracellular potential based cardiac mapping has been supplemented by “optical mapping”, in which high resolution optical recordings of transmembrane potential are made on the surfaces of the heart. This technique has provided new insights into the mechanisms of fibrillation (Gray et al., 1998) and defibrillation (Efimov et al., 1998). Hearts are stained with a voltage-sensitive fluorescent dye which exhibits a linear fluorescence response to changes in membrane potential (Fluhler et al., 1985). Traditionally free space lenses have been employed to image the

fluorescence emitted from the surface of the heart onto CCD or photodiode arrays, or photomultiplier tubes.

There have been several land-mark studies which have utilized optical mapping. Amongst these was the first demonstration of spiral wave re-entrant propagation in the heart (Davidenko et al., 1992). Also of significance was the visualisation of virtual cathode and anode regions during shock application to the epicardial surface (Knisley, 1995). Both of these studies sought to confirm the presence of phenomena which had been previously predicted in theoretical models of cardiac propagation.

Beyond the heart surfaces

Despite extensive use of optical mapping in cardiac rhythm laboratories over the last 10 years, our knowledge of the mechanisms of re-entrant arrhythmia and fibrillation is still insecure. Electrical activation can be recorded with high spatial and temporal resolution at the heart surface. However, re-entrant arrhythmia and fibrillation are three-dimensional events that involve relatively large tissue volumes and surface activation patterns do not fully reflect the intramural processes that underlie these rhythm disturbances. The possibility of extending optical techniques beyond measurements of epi- or endo- cardial potential is one of the most exciting challenges that remains for optical mapping. The ability to access transmembrane potential at sites deep within the heart wall is clearly of enormous interest. The ‘Holy Grail’ of cardiac mapping would be to record transmembrane potential throughout the entire three-dimensional beating heart, although the laws of physics make this an extremely difficult proposition.

Wavefronts of mechanical deformation have been mapped in three-dimensions using tagged MRI, and these maps may be used as surrogates for electrical activation (Augenstein, 2001). The maps offer relatively poor temporal and spatial resolution however, and require several cardiac cycles for reconstruction. Moreover, electrical activation can be but loosely linked to the myofibre strain fields that tagged MRI produces.

The past decade has seen an explosion in the use of confocal microscopy in the biological sciences, which has revolutionised the depth resolution of fluorescence indicators. This has made it possible to study tissue structure and function in three dimensions. Moreover, two-photon microscopy, a close analogue of confocal microscopy, is becoming increasingly popular amongst biologists. In principle, confocal or two-photon microscopy could be used to track cardiac electrical activation at sites below the surface of the epicardium, using voltage-sensitive dyes. Both of these techniques, however, have limited depth penetrations, and are hence inappropriate as a means of detecting transmembrane potentials deep within myocardium. The techniques rely on detecting photons which have escaped from the tissue mass. Such escape is limited to shallow depths due to photon scattering and absorption. In confocal microscopy the pinhole configuration limits placement of the detector to the same side of the tissue as the illumination. Two-photon microscopy does not require a pinhole, and conceivably the detector can be placed in any direction from the tissue. Indeed, one may wish to completely surround the tissue with detectors to detect any photons which make it to the tissue surface and beyond. Unfortunately, however, the two-photon excitation effect itself, whereby two photons of long wavelength (~1000nm) combine to excite a fluorochrome, is limited also to shallow depths of tissue (see *Chapter 4*).

It has been suggested that a possible approach to recording transmembrane potential at multiple sites through the heart wall would be to use intense illumination, and a form of optical tomography (Holden, 1998). Optical tomography has been used to reconstruct the three-dimensional spatial organisation of rotating scroll waves in chemical media (Winfree, et al., 1996). In this context, spatial variations in the opacity of the medium to visible light provides a means of reconstructing excitation waves by filtered backprojection. Myocardium is much less transparent than the gel medium used in these experiments however. As with confocal microscopy, obtaining sufficient signal from deep layers of myocardium is the major obstacle to this approach. The basis of a standard filtered backprojection technique is the ability to project a shadow of a semi-opaque sample onto a detector array by transilluminating the sample with parallel beams of light

from several directions. The profile of the shadow intensity recorded from a two-dimensional sample may be expressed as

$$P(\phi,t) = \frac{e^{\int \mu(x,y)dS}}{I_o} \tag{1.1}$$

where φ is the angular direction of the projection, t is the position within the shadow, μ is the spatially varying attenuation coefficient of the sample, S is the straight line of light travel through the sample, and I_o is the intensity of light incident on the sample. Using the shadows of the sample recorded from many directions of trans-illumination, one may reconstruct the sample *f(x,y)* (Russ, 1995). A three-dimensional sample, represented by *f(x,y,z)* may be similarly reconstructed by simply stacking a number of two-dimensional reconstructions *f(x,y)*. It is conceivable that tomography could be applied to imaging, in three-dimensions, the excitation processes in myocardium. Such a technique would either require the use of dyes which undergo light absorption changes with response to membrane potential (e.g. dye RH-155; Molecular Probes Inc.), or the backprojection of fluorescence images from, say, di-4-ANEPPS. By using fluorescence probes, some degree of spatial depth resolution is possible from projection in only one angle (φ) (Baxter et al., 2001), whereas this is not the case with absorption dyes. Tomography with fluorescence dyes would necessitate a new method of backprojection which took into account this single angle spatial information. On the other hand, absorption dyes are as yet untested on the heart.

Baxter et al. (2001) showed that trans-illumination of right ventricular myocardium is a viable approach to imaging fluorescence from deep within myocardium. They used di-4-ANEPPS in combination with both trans-illumination and epi-illumination to gather signals that could be assigned with weightings to depth ranges in their right ventricular slab preparation. For example, it was estimated that 90% of their trans-illumination signal originated from a 4mm thick layer of myocardium, near to the illuminated surface. Without combining trans-illumination with optical tomography, however, this spatial resolution in the axis through the heart wall is very poor, and images have a very high degree of spatial blurring both in this axis, and laterally in the plane of the epicardial

surface (Baxter et al., 2001). It may be possible to correct some of the lateral spatial blur in the activation sequences of Baxter et al. with appropriate use of deconvolution techniques (Pawley, 1995). Tomography and deconvolution are both processes which degrade signal-to-noise ratio of an image – this is inherent in their capacity to improve spatial resolution. Unfortunately, it seems unlikely that further reduction in fidelity of the trans-illumination signals presented in Baxter et al. (2001) could be tolerated.

In summary, although cardiac mapping experiments have been carried out for over 80 years, there remain several limitations in terms of the data able to be gathered in these experiments. In order to make further advance in this field, a robust method for visualising and reconstructing excitation in three-dimensional tissue is required. The candidate methods discussed, namely MRI, confocal microscopy, and optical tomography all offer such limited efficacy as to motivate a completely new approach. Optical fibres offer the ability to carry excitation light to, and fluorescence from, tissue sites deep within the ventricular wall of the heart. By using such fibres, the problems of scattering and absorption of the voltage-dependent signal that limit the utility of confocal microscopy, tomography, and trans-illumination type techniques in tracking three-dimensional propagation might be overcome. The development and characterisation of a novel fibre-optic based experimental technique to probe transmembrane potential at multiple sites through the heart wall was undertaken *(Chapter 3).*

1.1.5 Computer Modelling

Over the past decade, there has been a paradigm shift from experimental to computer model based analysis of propagation in the heart. The large effort required to perform experiments under controlled conditions, the physical limits of recording apparatus such as electrode size/density/impedence, the difficulties of making experimental recordings without altering the physiological processes under examination, and the inability to experimentally alter just one component of the enormous range of variables present in a piece of tissue, have all contributed to this shift. As computers have grown in capacity and speed, it has become practical to obtain three-dimensional solutions to the equations

governing electrical propagation over the entire geometry of the heart. The outputs of such models are an experimentalist's dream. Any variable in the model may be interrogated at any point in the solution domain, at any time. Further, any parameter input to the model may be adjusted, and the effect on the model solution examined. Interpretation of computer model results must always proceed with caution, however, as models are inevitably a gross simplification of the huge complexity of biological systems. Current research sees experimental results being used to suggest appropriate frameworks for mathematical models, as well as suitable parameter values for input to these models. In turn, the models provide feedback to experimental work, allowing experimenters to direct their investigations toward aspects of critical significance to the model outcome, and to carry out work verifying model based predictions.

The theoretical basis for interpretation of cardiac mapping experiments currently rests with the bidomain model. The bidomain model of propagation approximates cardiac tissue as two interpenetrating domains – the intra- and extra- cellular spaces. The concept was first proposed by Schmitt (1969), and mathematical formulations of bidomain models began in earnest in the late 1970's and early '80s (Spach et al., 1979; Geselowitz et al., 1982; Plonsey and Barr, 1987). Much early work concentrated on exact mathematical solutions to the equations in simplified (often cylindrical) domains. The bidomain model has now been well validated in a number of experimental studies (see Henriquez, 1993 for review). The current state of the art is large scale solutions to the bidomain equations over anatomically realistic geometries, using numerical techniques such as finite elements and finite differences, and fast computers (Sands, 1996).

The bidomain framework describes diffusion of ions in both extracellular and intracellular spaces, and leaves access for additional cellular level models to describe the ion flux across the cellular membrane. These are "insertable" models which describe the membrane kinetics of the cardiomyocyte. Such "ionic current models" fall into two broad categories: *biophysical* or *simplified* models. Biophysical models attempt to describe all the behaviour of a myocyte. They tend to be large and complex, requiring much computational resource to solve. Simplified models aim to reproduce the key features of

the more complex models, such as activation or recovery, with a minimum of parameters. These models are small and fast to solve, but are not derived directly from physiological observation.

Two different ionic current models are utilized in this thesis: a modified version of the Beeler Reuter (BR) model, and a cubic model of activation. Firstly, the BR model (Beeler and Reuter, 1977) is one of the most simple biophysically based ionic current models. It describes four ionic currents: a sodium inward current I_{Na}, a calcium inward current I_{Ca}, a background potassium current I_{K1}, and a plateau potassium current I_K. Hence the total transmembrane current I_{ion} is the sum of these four components:

$$I_{ion} = I_{Na} + I_{Ca} + I_{K1} + I_K \tag{1.2}$$

The BR model also carries a description of intracellular calcium concentration $[Ca^{2+}]_i$. Hodgkin-Huxley type rate equations are used to describe the kinetics of the various currents. For example, the sodium current is described by

$$I_{Na} = (\overline{g_{Na}} m^3 hj + g_{NaC})(V_m - E_{Na}) \tag{1.3}$$

where $\overline{g_{Na}}$ is the maximum sodium channel conductance, g_{NaC} is a steady-state sodium conductance, E_{Na} is the sodium reversal potential, V_m the membrane potential, m is an activation variable, and h and j are inactivation variables. The time course of variables m, h, and j are described by first-order differential equations with membrane potential dependent rate constants.

Activation can also be modelled in a simpler fashion using a single polynomial to describe the upstroke of the action potential. The cubic model of activation fits a cubic function to the activation process, but does not describe repolarisation, and hence cannot be used for studies of re-entrant arrhythmia. The general form of the model is

$$I_{ion} = \overline{g_m} V_m \left(1 - \frac{V_m}{V_t}\right)\left(1 - \frac{V_m}{V_p}\right) \tag{1.4}$$

where $\overline{g_m}$ is a conductance equal to the slope of the cubic function at the origin, V_t is the threshold potential, and V_p the plateau potential.

The Auckland Heart Model

The Auckland Bioengineering Research group has developed a realistic finite element model of cardiac anatomy which incorporates detailed information about ventricular geometry and myocyte architecture from dog hearts (Hunter et al., 1997; LeGrice et al.,1995). The Auckland heart model has been used by several research groups world-wide to study cardiac activation (Holden, 1998). Issues currently being addressed in whole heart simulations include the spatio-temporal evolution of fibrillation, and progression of activation during and following defibrillation.

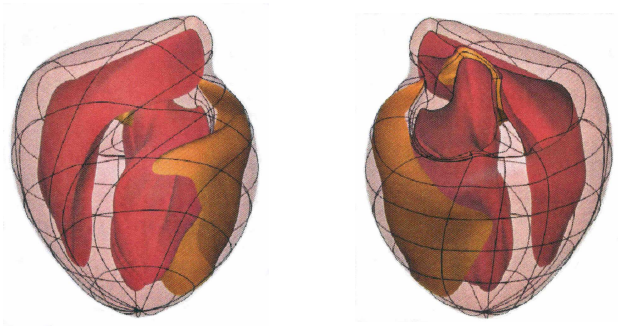

Fig. 1.4 *Activation modelling on the Auckland Heart Model*

The heart model is shown from anterior (left) and posterior (right) aspects, with pink surfaces representing the epicardium, and red surfaces the endocardium. A propagating wavefront is shown as an isosurface coloured gold. Reproduced with permission from: Tomlinson, K.A. 2000. *Finite element solution of an eikonal equation for excitation wavefront propagation in ventricular myocardium*. PhD Thesis, University of Auckland.

The Auckland Bioengineering Research group has successfully used a bidomain approach with this anatomic model to simulate the propagation of electrical activation throughout the right and left ventricles (Fig. 1.4). Prior to this, a simpler “monodomain” model was used in simulations. This model limits description of ion fluxes to intracellular and transmembrane compartments by setting the extracellular potential to be uniformly zero. The monodomain model is not suitable for analysing defibrillation, as current cannot be applied to the extracellular domain. In analysis of propagation, however, the monodomain model provides a reasonable estimate of the results obtained with a full bidomain model (Buist, 2001).

From global geometry to microstructure

There are ongoing deficits in aspects of computer modelling of electrical propagation in the heart. At present the fibrous and laminar architecture of the heart is incorporated into the model by a continuous description of fibre and sheet angle matched with an orthotropic conductivity tensor for both intra- and extra- cellular domains. However, the relationship between observed microstructural anisotropy and electrical activation remains uncertain. Whether in fact the heart behaves in an electrically orthotropic fashion, or whether propagation is isotropic in the plane orthogonal to fibre direction is contested. Moreover, the extent to which a continuum model can provide an adequate description of the effects of local structural discontinuities is unclear. There is an urgent need for more detailed investigation of these issues particularly within the context of electrical propagation from an ectopic stimulus and response of the heart to defibrillation. These effects are studied in detail in *Chapter 2* of this thesis. For this purpose, combination of extended confocal microscopy to reconstruct tissue volumes at high resolution (Young et al., 1998), and finite element modelling, promises to open an entirely new field of research. Combination of these techniques was investigated, and the results bear significance for functional modelling studies in a number of biological organs.

1.2 Summary

The motivation for embarking on the research outlined in this thesis was to understand the influence of cardiac structure on normal and abnormal electrical propagation in the heart. From the discussion in this chapter, it is evident that complimentary use of 3D electrical mapping and computer modeling is necessary to make major advances in the area, particularly within the context of arrhythmia, fibrillation and defibrillation. However, it is also clear that existing electrical mapping methods and computer models of cardiac electrical activation have significant deficiencies which must be addressed before significant further progress can be made.

In particular, it is necessary:

(1) To determine the extent to which microstructural discontinuities influence the propagation of normal and abnormal electrical propagation in the heart, and to develop realistic and computationally tractable methods for incorporating these effects into models of cardiac electrical activation.

(2) To develop new techniques for mapping three-dimensional intramural electrical activity in the heart. Ideally, this methodology should faithfully reproduce the cardiac action potential, address relatively small tissue volumes, be minimally invasive and capable of scaling to a relatively large number of channels.

These requirements define the objectives of the research described in this thesis. The modeling section of the thesis *(Chapter 2)* describes results of significance to the biological function of the heart, whilst the experimental section *(Chapters 3 and 4)* develops a new technique which promises to yield further insights into myocardial function in the future.

Chapter 2

Influence of the discontinuous laminar organisation of cardiomyocytes on electrical propagation and response to cardioversion

(submitted to *Circulation Research*, February 2002)

Abstract

Extended laser scanning confocal microscopy has recently been used to reconstruct the discontinuous laminar organisation of cardiomyocytes in a block of rat left ventricle. The confocal data allowed delineation of intercellular clefts or cleavage planes which coursed through the tissue block. This study describes a finite element model of electrical propagation which permitted the accurate incorporation of the structural discontinuity apparent in the tissue reconstruction. The effects of the cleavage planes on propagation from focal activation in the midwall, and on the response to a defibrillation-strength shock were examined. It is concluded that the laminar organisation of myocytes may lead to orthogonal anisotropy of electrical properties about microstructurally defined axes. In addition, structural discontinuity gave rise to complex polyphasic extracellular potentials, and asymmetric propagation from a focal activation. During application of shock, the cleavage planes acted as a substrate for far field stimulation, which was responsible for activation of the bulk myocardium within the duration of the applied current.

2.1 Introduction

There is now a considerable body of evidence from diverse sources to suggest that cardiomyocytes are arranged in a discontinuous laminar fashion throughout the right and left ventricles of the heart. Sections cut from the ventricles reveal extensive intercellular clefts (see Fig. 2.1), particularly in the midwall region (Robb and Robb, 1942; Fenesis, 1943; Weitz, 1951; Hort, 1960; Spotnitz et al., 1974). Thick longitudinal ventricular sections have a layered appearance due to the numerous cleavage planes between myocyte laminae, which run radially across the wall (Fenesis, 1943; Weitz, 1951; Hort, 1957; Hort, 1960; Spotnitz et al., 1974). Work carried out in our laboratory (LeGrice et al., 1995; Young et al., 1998) has confirmed myocardium to be a branching sheet structure, rather than a branching syncytium (Streeter and Bassett, 1966).

The implications of various forms of structural discontinuity for both electrical propagation, and the myocardial response to cardioversion, have been investigated in a number of studies (Fast and Kleber, 1995; Fast et al., 1998; Gillis et al., 1996; Krassowska et al., 1990). Neonatal rat myocyte cultures have been used to determine the effects of discontinuous structures on propagation velocity (Kucera et al., 1998), and the safety of conduction (Rohr et al., 1997). Furthermore, the development of “secondary sources” of excitation during defibrillation: their dependence on discontinuity (Fast et al., 1998), and their evolution during shock has been investigated (Fast et al., 2000). It has been suggested that discontinuity provided by cell-to-cell gap junctional coupling, as well as collagenous septae, and blood vessels may be important in the activation of a critical mass of tissue during shock application (Trayanova, 1996; Fast et al., 1998; Gillis et al., 1996; Trayanova, 1999; Gillis et al., 2000).

To date however, understanding of the role these effects have in a structurally accurate representation of intact three-dimensional myocardium has remained elusive. In the present study, this question is approached using the tools of computer modelling. This is necessary due to the lack of an experimental technique able to examine three-dimensional

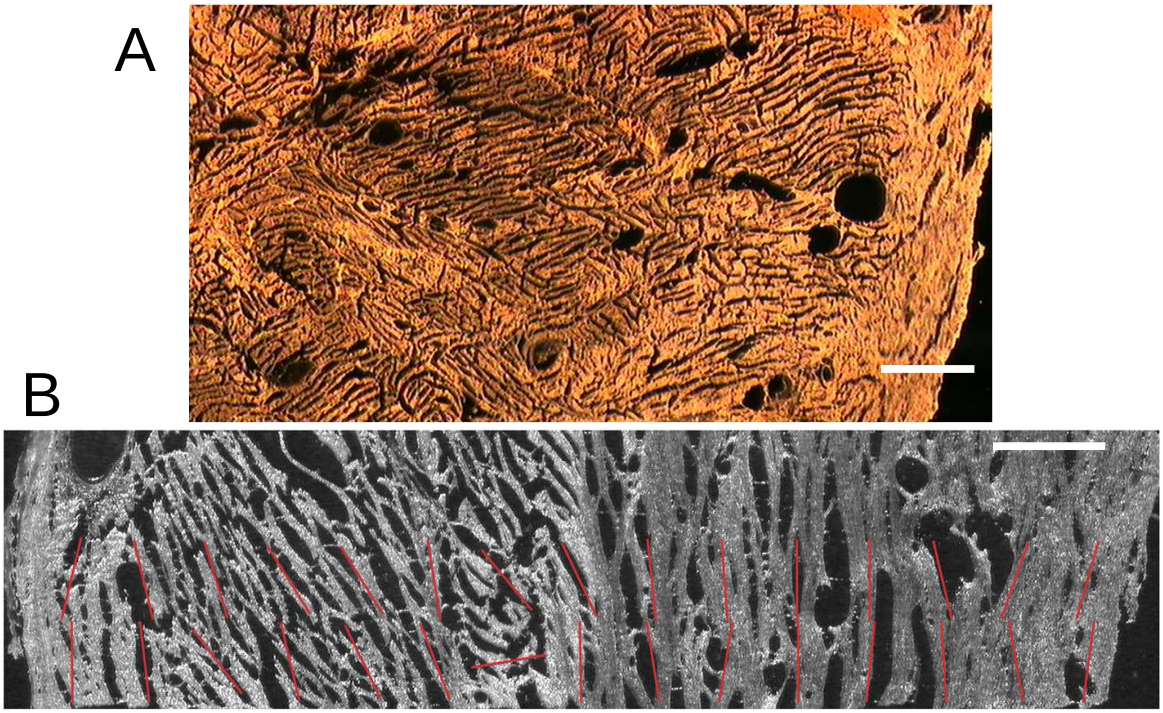

Figure 2.1 *Laminar architecture of porcine ventricular myocardium*

(A) Photograph of a 20μm thick section of myocardium. Tissue slice has been left to dry for ~1hr after cryo-sectioning to allow separation of adjacent myocyte laminae. Circular holes in section toward the epicardial surface (right side) are blood vessels. There are regions within the midwall where adjacent pockets of myocyte laminae lie in orthogonally opposed orientations. Note the thin section allows fine detail of the laminar structure to be resolved (compare (B) below). (B) 100μm frozen section depicting the laminar architecture at more coarse resolution. The myocyte laminae orientation may be assigned by automated vector placement (red lines) across the image (Hodgets, 1996) to allow rapid fitting of a mathematical model of the laminar structure (LeGrice, 1992). Scale bars indicate 1mm.

electrical events at high resolution. This chapter describes a model of electrical propagation solved in a structurally discontinuous domain, which accurately represents the measured three-dimensional microstructure of tissue taken from the free-wall of the

rat left ventricle. The governing equations are the bidomain equations, which have been well validated in a number of experimental studies (for review see Henriquez, 1993). The model is used to address the hypotheses that (1) early propagation from a focal activation can only be accurately described by a discontinuous model of the myocardium, (2) that the laminar organization of myocytes determines unique electrical properties in three microstructurally defined directions at any point in myocardium, and (3) that intercellular clefts, or "cleavage planes" provide a substrate for secondary source formation during defibrillation.

2.2 Methods

2.2.1 Structural Representation

A block of rat left ventricular myocardium, of dimension 0.8 x 0.8 x 3.01mm was imaged using the technique of extended confocal microscopy (Young et al., 1998). The raw data consisted of a total of 5.06×10^8 cubic voxels, each with 1.56μm sides. The data revealed the complex three-dimensional branching laminar organisation of ventricular myocytes. For further analysis, the volume was reduced to a stack of 18 transmural images each with square pixels of side dimension 4.69μm. One of these images is shown in Fig. 2.2. These images were used to reconstruct the three-dimensional geometries of the intercellular clefts, or cleavage planes (LeGrice et al., 1995) which coursed through the tissue volume, separating myocyte laminae. A network of bilinear finite elements (Zienkiewicz and Taylor, 1994) describing the cleavage plane geometries was generated from the image stack by manual assignment of element nodes to regions devoid of myocyte-to-myocyte connections. Each finite element spanned a distance of 47μm in the *z* direction (see Fig. 2.2), which was the distance between successive images in the stack. In total, 1,540 elements, and 2,803 nodes were required for the accurate geometrical description of the cleavage planes (Fig. 2.2).

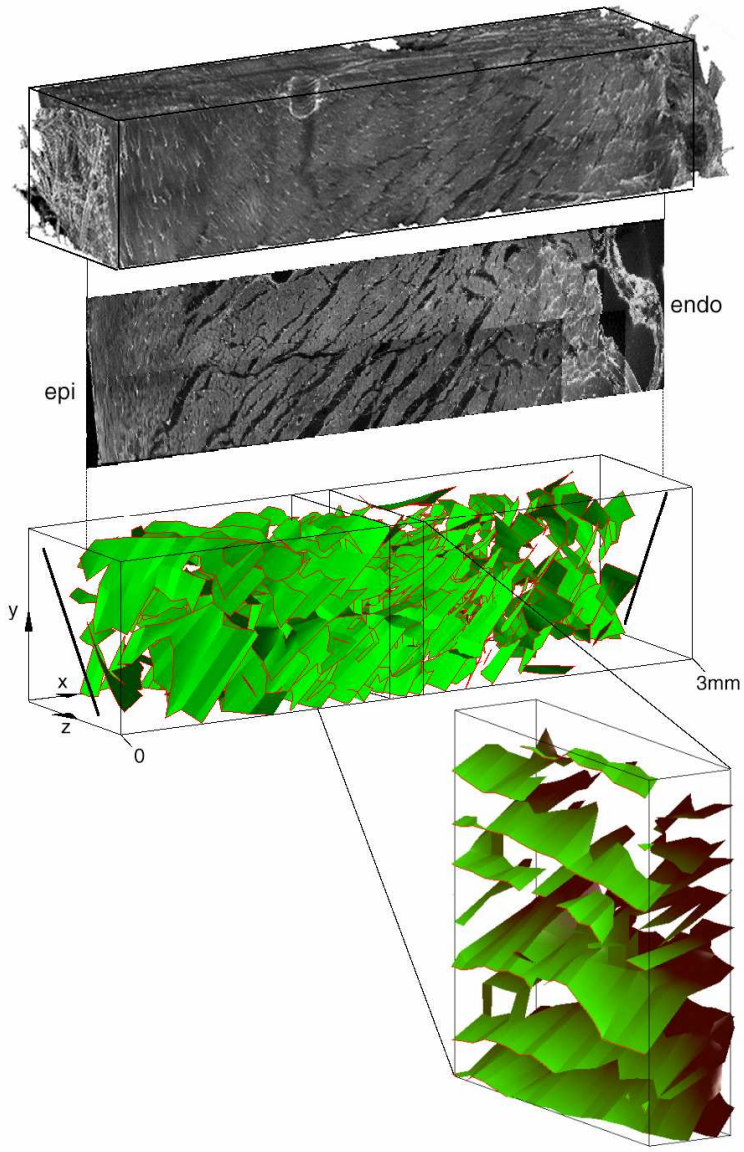

Figure 2.2 *Structural representation of the cleavage plane geometries* *Upper:* reconstructed volume of rat left ventricular free-wall myocardium. *Middle:* transmural slice from the reconstructed volume showing a complex network of cleavage planes which course between myocyte laminae. *Lower:* the bilinear finite element geometrical description of the cleavage planes through the entire rat tissue block, and a smaller midwall subsection. Myofibre orientation is shown on the epi- *(epi)*, and endo- *(endo)* cardial surfaces.

2.2.2 Discontinuous bidomain model formulation

The bidomain model describes cardiac tissue as consisting of two inter-penetrating spaces: the intracellular and extracellular domains (Henriquez, 1993).

The governing equations for the active bidomain model are:

$$i_{ion} + c_m \partial V_m / \partial t = \nabla \bullet (G^i \nabla (\phi_e + V_m)) \tag{2.1}$$

$$-\nabla \bullet (G^i \nabla V_m) = \nabla \bullet ((G^i + G^e) \nabla \phi_e) + i_{app} \tag{2.2}$$

where V_m is the transmembrane potential, Φ_e the extracellular potential, c_m the membrane capacitance, i_{ion} the transmembrane ionic current per unit volume, and i_{app} the current applied from an external source to the extracelluar domain. If we define three orthogonal unit vectors $\boldsymbol{a_l}$, $\boldsymbol{a_t}$, and $\boldsymbol{a_n}$ such that $\boldsymbol{a_l}$ is parallel to the myofibres (longitudinal), $\boldsymbol{a_t}$ is transverse to the fibres but in the plane of myocyte laminae, and $\boldsymbol{a_n}$ is normal to these laminae, the conductivity tensors G^i and G^e of Eqs. 2.1 and 2.2 may be described by:

$$G^i = \begin{bmatrix} \boldsymbol{a_l} & \boldsymbol{a_t} & \boldsymbol{a_n} \end{bmatrix} \begin{bmatrix} g_{il} & 0 & 0 \\ 0 & g_{it} & 0 \\ 0 & 0 & g_{in} \end{bmatrix} \begin{bmatrix} \boldsymbol{a_l}^T \\ \boldsymbol{a_t}^T \\ \boldsymbol{a_n}^T \end{bmatrix} \qquad G^e = \begin{bmatrix} \boldsymbol{a_l} & \boldsymbol{a_t} & \boldsymbol{a_n} \end{bmatrix} \begin{bmatrix} g_{el} & 0 & 0 \\ 0 & g_{et} & 0 \\ 0 & 0 & g_{en} \end{bmatrix} \begin{bmatrix} \boldsymbol{a_l}^T \\ \boldsymbol{a_t}^T \\ \boldsymbol{a_n}^T \end{bmatrix} \tag{2.3, 2.4}$$

where g_{il}, g_{it}, g_{in} are the effective intracellular, and g_{el}, g_{et}, g_{en} the effective extracellular conductivities in the three microstuctural directions (Hunter et al., 1997). The common bidomain model formulation (Muzikant and Henriquez, 1998; Entcheva et al., 1998; Knisley et al., 1999) treats each domain as a continuum, and simulations are made with the assumption of isotropic intracellular conductivities transverse to fibre direction (ie. $g_{it} = g_{in}$), without consideration of cleavage plane obstructions to intracellular current flow. A solution to the bidomain equations was sought, which allowed the accurate spatial representation of cleavage planes, in order to apply conditions of zero intracellular flux across these planes. A Galerkin finite element solution to the active bidomain equations was made on a mesh of trilinear elements, as outlined below.

In the following analysis we change notation for the membrane potential from V_m *to* ν for clarity. Equations (2.1) and (2.2) are coupled, and both must be solved at every time step. First we deal with equation (2.1). Rather than solving (2.1) directly, the finite element method forms the weighted residual

$$\int_{\Omega} \left(\nabla \bullet G^i \nabla \nu + \nabla \bullet G^i \nabla \phi_e - c_m \partial \nu / \partial t - i_{ion} \right) \omega d\Omega = 0 \tag{2.5}$$

where ω is a weighting function.
Using the Green-Gauss theorem,

$$\int_{\Omega} \nabla \bullet G^i \nabla \nu \omega d\Omega = -\int_{\Omega} (G^i \nabla \nu) \bullet \nabla \omega d\Omega + \int_{\Gamma} \nabla \nu \bullet G^i \boldsymbol{n} \omega d\Gamma \tag{2.6}$$

$$\int_{\Omega} \nabla \bullet G^i \nabla \phi_e \omega d\Omega = -\int_{\Omega} (G^i \nabla \phi_e) \bullet \nabla \omega d\Omega + \int_{\Gamma} \nabla \phi_e \bullet G^i \boldsymbol{n} \omega d\Gamma \tag{2.7}$$

we may reduce the order of derivatives in (2.5) from two to one (***n*** is the outward pointing normal to the domain boundary). Substituting (2.6) and (2.7) into equation (2.5) we obtain

$$-\int_{\Omega} (G^i \nabla \nu) \bullet \nabla \omega d\Omega - \int_{\Omega} c_m \frac{\partial \nu}{\partial t} \omega d\Omega =$$

$$-\int_{\Gamma} \nabla \nu \bullet G^i \boldsymbol{n} \omega d\Gamma - \int_{\Gamma} \nabla \phi_e \bullet G^i \boldsymbol{n} \omega d\Gamma + \int_{\Omega} i_{ion} \omega d\Omega + \int_{\Omega} (G^i \nabla \phi_e) \bullet \nabla \omega d\Omega \tag{2.8}$$

The finite element method dissects the large solution domain into a number of smaller elements. The functions $v(\boldsymbol{x})$ and $\Phi_e(\boldsymbol{x})$ are represented by storing global nodal values of these variables (v^n, Φ_e^n *(nodal index(n)*=1..*total number of nodes))*. Within each element an element-local coordinate system is defined (ξ). Interpolation or *basis* functions are

used to interpolate the functions over the domain Ω. Here we use *trilinear* Lagrange basis functions, such that $\nu(\boldsymbol{x}(\boldsymbol{\xi})) = \nu^n \psi^n(\boldsymbol{\xi})$ (2.9), and $\phi_e(\boldsymbol{x}(\boldsymbol{\xi})) = \phi_e{}^n \psi^n(\boldsymbol{\xi})$ (2.10), where

$$\begin{aligned}
&\psi^1(\xi_1\xi_2\xi_3) = (1-\xi_1)(1-\xi_2)(1-\xi_3) && \psi^2(\xi_1\xi_2\xi_3) = \xi_1(1-\xi_2)(1-\xi_3)\\
&\psi^3(\xi_1\xi_2\xi_3) = (1-\xi_1)\xi_2(1-\xi_3) && \psi^4(\xi_1\xi_2\xi_3) = \xi_1\xi_2(1-\xi_3)\\
&\psi^5(\xi_1\xi_2\xi_3) = (1-\xi_1)(1-\xi_2)\xi_3 && \psi^6(\xi_1\xi_2\xi_3) = \xi_1(1-\xi_2)\xi_3\\
&\psi^7(\xi_1\xi_2\xi_3) = (1-\xi_1)\xi_2\xi_3 && \psi^8(\xi_1\xi_2\xi_3) = \xi_1\xi_2\xi_3
\end{aligned} \tag{2.11}$$

There is no attempt to ensure continuity of derivative in the v and Φ_e fields, as would be achieved with the use of higher order cubic Hermite basis functions.

The Galerkin finite element method puts $\omega = \psi^m$. Substituting (2.9) and (2.10) into the LHS of equation (2.8) gives

$$\begin{aligned}
LHS &= -\int_\Omega G^i{}_{ij} \frac{\partial(\nu^n\psi^n)}{\partial x_j}\frac{\partial\psi^m}{\partial x_i}d\Omega - \int_\Omega c_m \frac{\partial(\nu^n\psi^n)}{\partial t}\psi^m d\Omega\\
&= -\nu^n \sum_e \int_{\Omega_e} G^i{}_{ij} \frac{\partial\psi^n}{\partial\xi_k}\frac{\partial\xi_k}{\partial x_j}\frac{\partial\psi^m}{\partial\xi_d}\frac{\partial\xi_d}{\partial x_i} J d\boldsymbol{\xi} - \sum_e \left(\frac{\partial\nu}{\partial t}\right)^n \int_{\Omega_e} c_m \psi^n\psi^m d\xi
\end{aligned} \tag{2.12}$$

where J is the Jacobian of the transformation from $\boldsymbol{x}$ coordinates to $\boldsymbol{\xi}$ coordinates. Equation (2.12) may be written more simply

$$LHS = \boldsymbol{K}\boldsymbol{v} + \boldsymbol{M}\left(\frac{d\boldsymbol{v}}{dt}\right) \tag{2.13}$$

where $\boldsymbol{K}$ and $\boldsymbol{M}$ are known as the global stiffness and mass matrices respectively, and $\boldsymbol{v}$ is a vector of global nodal unknown transmembrane potentials. All that remains is to discretise the time domain to approximate *d/dt.* In doing so, (2.13) becomes

$$LHS = \boldsymbol{K}\left[\theta\boldsymbol{v}^{i+1} + (1-\theta)\boldsymbol{v}^i\right] + \boldsymbol{M}\left(\frac{\boldsymbol{v}^{i+1}-\boldsymbol{v}^i}{\Delta t}\right) \tag{2.14}$$

where θ is a weighting factor satisfying $0 < \theta < 1$, and i indicates the i^{th} time step Δt. For $\theta = 0.5$ the method is known as the *Crank-Nicolson-Galerkin* method and errors arising

from the time discretisation method are $O(Dt^2)$. Equation (2.14) may be rearranged to separate terms in v^{i+1} and v^i as

$$LHS = \boldsymbol{K}\left[\boldsymbol{M}+\theta\Delta t\boldsymbol{K}\right]\boldsymbol{v}^{i+1} - \left[\boldsymbol{M}-(1-\theta)\Delta t\boldsymbol{K}\right]\boldsymbol{v}^{i} \tag{2.15}$$

We now deal with the RHS of equation (2.8). Term 3 may be re-written as

$$\int_{\Omega} i_{ion}\omega d\Omega = {i_{ion}}^{n}\sum_{e}\int_{\Omega}\psi_n\psi_m J d\xi = \boldsymbol{L}\boldsymbol{i}_{\boldsymbol{ion}} \tag{2.16}$$

whilst term 4 becomes

$$\int_{\Omega}(G^i\nabla\phi_e)\bullet\nabla\omega d\Omega = \boldsymbol{K}\boldsymbol{\varphi}_{\boldsymbol{e}} \tag{2.17}$$

Substituting (2.15), (2.16), and (2.17) into (2.8), and approximating $\boldsymbol{i}_{\boldsymbol{ion}}$ and $\boldsymbol{\Phi}_{\boldsymbol{e}}$ by their values at the i^{th} time step, we may write

$$\left[\boldsymbol{M}+\theta\Delta t\boldsymbol{K}\right]\boldsymbol{v}^{i+1} = \left[\boldsymbol{M}-(1-\theta)\Delta t\boldsymbol{K}\right]\boldsymbol{v}^{i} + \boldsymbol{K}{\boldsymbol{\varphi}_{\boldsymbol{e}}}^{i} + \boldsymbol{L}{\boldsymbol{i}_{\boldsymbol{ion}}}^{i} - \int_{\Gamma}\nabla V\bullet G^i\boldsymbol{n}\omega d\Gamma - \int_{\Gamma}\nabla\phi_e\bullet G^i\boldsymbol{n}\omega d\Gamma \tag{2.18}$$

where the final two integral terms are equal to zero in the case of Neumann (no-flux) boundary conditions. We may use the conjugate gradient method to obtain a solution to the above system of equations in $\boldsymbol{v}^{i+1}$. Having obtained the $(i+1)^{th}$ solution to the transmembrane potential, we now use this field in the solution of equation (2.2). Forming the weighted residual, and using the Green-Gauss theorem as above, we form an equation from (2.2) which is similar in form to (2.8)

$$\int_{\Omega}((G^i+G^e)\nabla\phi_e)\bullet\nabla\omega d\Omega =$$

$$-\int_{\Omega}(G^i\nabla v)\bullet\nabla\omega d\Omega + \int_{\Omega} i_{app}\omega d\Omega + \int_{\Gamma}\nabla v\bullet G^i\boldsymbol{n}\omega d\Gamma + \int_{\Gamma}\nabla\phi_e\bullet(G^i+G^e)\boldsymbol{n}\omega d\Gamma$$

which may be written in the form

$$\boldsymbol{Q\varphi_e}^{i+1} = -\boldsymbol{K\nu}^{i+1} + \boldsymbol{Li_{app}}^{i} + \int_{\Gamma} \nabla\nu \bullet G^{i}\boldsymbol{n}\omega d\Gamma + \int_{\Gamma} \nabla\phi_e \bullet (G^{i} + G^{e})\boldsymbol{n}\omega d\Gamma \tag{2.19}$$

where

$$\boldsymbol{Q} = \sum_{e} \int_{\Omega_e} (G^{i}{}_{ij} + G^{e}{}_{ij}) \frac{\partial\psi^{n}}{\partial\xi_k} \frac{\partial\xi_k}{\partial x_j} \frac{\partial\psi^{n}}{\partial\xi_d} \frac{\partial\xi_d}{\partial x_i} Jd\boldsymbol{\xi}$$

As in (2.18) the boundary integrals are equal to zero under boundary conditions of zero-flux, and the conjugate gradient method may be used to obtain the solution to the field $\boldsymbol{\Phi}_e$.

Disruption of cellular connections across cleavage planes was achieved by the uncoupling of adjacent nodes and application of the Neumann boundary condition $\nabla\varphi_i \bullet n = 0 \; on \; \Gamma$ (where $\varphi_i = \nu + \varphi_e$), along internal boundaries of the intracellular space. A two-dimensional example is illustrated in Fig. 2.3A, where a discontinuity described in space by one-dimensional linear elements (yellow lines) is introduced into a bilinear element mesh in the intracellular domain, resulting in a piecewise square approximation to the original discontinuity. No-flux boundaries are shown in red (Fig. 2.3A). In a similar fashion, the present three-dimensional study used a two-dimensional bilinear element description of discontinuity to disrupt a trilinear mesh. This process is illustrated in Fig. 2.3B, where a cross-section through the bilinear element network (yellow lines) is superimposed upon the transmural slice of Fig. 2.2. The resulting regions of uncoupled nodes are shaded in green, whilst the inset shows no-flux boundaries as red lines as in part *A* of the figure.

The exact criterion for the uncoupling of adjacent nodes is outlined below. The nodal points of the trilinear finite element solution mesh are indexed by *n* (*n*=1..*total number of nodes*). The $\boldsymbol{x}$ locations of the four nodes of a single cleavage plane finite element may be written as $\boldsymbol{x}^1$, $\boldsymbol{x}^2$, $\boldsymbol{x}^3$, $\boldsymbol{x}^4$. Projection in direction $\pm x_i$ (i=1..3) of solution mesh node point *n* was made onto each cleavage plane element in turn. The $\boldsymbol{\xi}$ positions (in terms of the local

coordinates of the cleavage plane finite element) of the projected points (indexed by *p*) were calculated as follows:

$$\xi_1{}^p = \begin{cases} \dfrac{-\delta \pm \sqrt{\delta^2 - 4\lambda\gamma}}{2\lambda} & \text{when } \lambda \neq 0 \\ -\dfrac{\gamma}{\delta} & \text{when } \lambda = 0 \end{cases} \tag{2.20}$$

where

$$\left.\begin{aligned} \lambda &= (x_j{}^2 - x_j{}^1)(x_k{}^1 - x_k{}^2 - x_k{}^3 + x_k{}^4) \;-\; (x_k{}^2 - x_k{}^1)(x_j{}^1 - x_j{}^2 - x_j{}^3 + x_j{}^4) \\ \delta &= (x_k{}^n - x_k{}^1)(x_j{}^1 - x_j{}^2 - x_j{}^3 + x_j{}^4) \;-\; (x_j{}^n - x_j{}^1)(x_k{}^1 - x_k{}^2 - x_k{}^3 + x_k{}^4) \\ &\quad + (x_j{}^2 - x_j{}^1)(x_k{}^3 - x_k{}^1) \;-\; (x_k{}^2 - x_k{}^1)(x_j{}^3 - x_j{}^1) \\ \gamma &= (x_j{}^3 - x_j{}^1)(x_k{}^n - x_k{}^1) \;-\; (x_k{}^3 - x_k{}^1)(x_j{}^n - x_j{}^1) \end{aligned}\right\}$$

(j, k=1..3; $i \neq j \neq k$)

$$\xi_2{}^p = \frac{(x_k{}^n - x_k{}^1) \;-\; (x_k{}^2 - x_k{}^1)\xi_1{}^p}{(x_k{}^3 - x_k{}^1) + (x_k{}^1 - x_k{}^2 - x_k{}^3 + x_k{}^4)\xi_1{}^p} \tag{2.21}$$

Two adjacent node points n_1 and n_2 were disconnected where the following conditions were satisfied: $0 < \xi_1{}^p < 1$ and $0 < \xi_2{}^p < 1$ (ie. the projected point *p* lay within the cleavage plane element boundary) and $[x_i(n_1) - x_i(p)][x_i(n_2) - x_i(p)] < 0$ (ie. the two adjacent node points straddled the cleavage plane). Equations (2.20) and (2.21) may be readily derived from rearrangement of the basic finite element interpolation equation $x_i = \psi^n x_i{}^n$.

A finite element solution of the bidomain equations was used in preference to a finite difference approximation (Keener, 1988), as the Neumann condition could be maintained exactly at all internal intracellular boundaries, with a minimum number of degrees of freedom. Two sets of bidomain simulations were carried out to investigate both the

response of the tissue to propagation following point stimulation *(Part I, below)*, and the response to cardioversion *(Part II)*. In both parts the results of the discontinuous structural model described above were compared to a fully orthotropic continuous model, which incorporated a continuum description of both the transmural variation of fibre orientation and cleavage plane angle. Hereafter, these two models are referred to as the discontinuous and continuous models respectively. Both models incorporated a linear variation of fibre angle (α) through the ventricle wall based on angle measurements from the confocal data, giving

$$\alpha(x) = 0.83x - 1.28 \quad \text{(radians; see Fig. 2.2 for direction of } x\text{)} \tag{2.22}$$

The assumption that $g_{it} = g_{in}$ was applied across the entire domain in the discontinuous model, since any possible anisotropy of conductivity transverse to the fibre direction was implicitly modelled by the inclusion of the cleavage plane discontinuities. The continuous model incorporated the following cubic approximation of the transmural variation of cleavage plane angle β (defined in Hunter et al., 1997),

$$\beta(x) = -0.0892x^3 + 0.5595x^2 - 0.8114x + 0.8669 \quad \text{(radians)} \tag{2.23}$$

and the assumption $g_{it} = g_{in}$ was relaxed in order to best approximate the discontinuous solution.

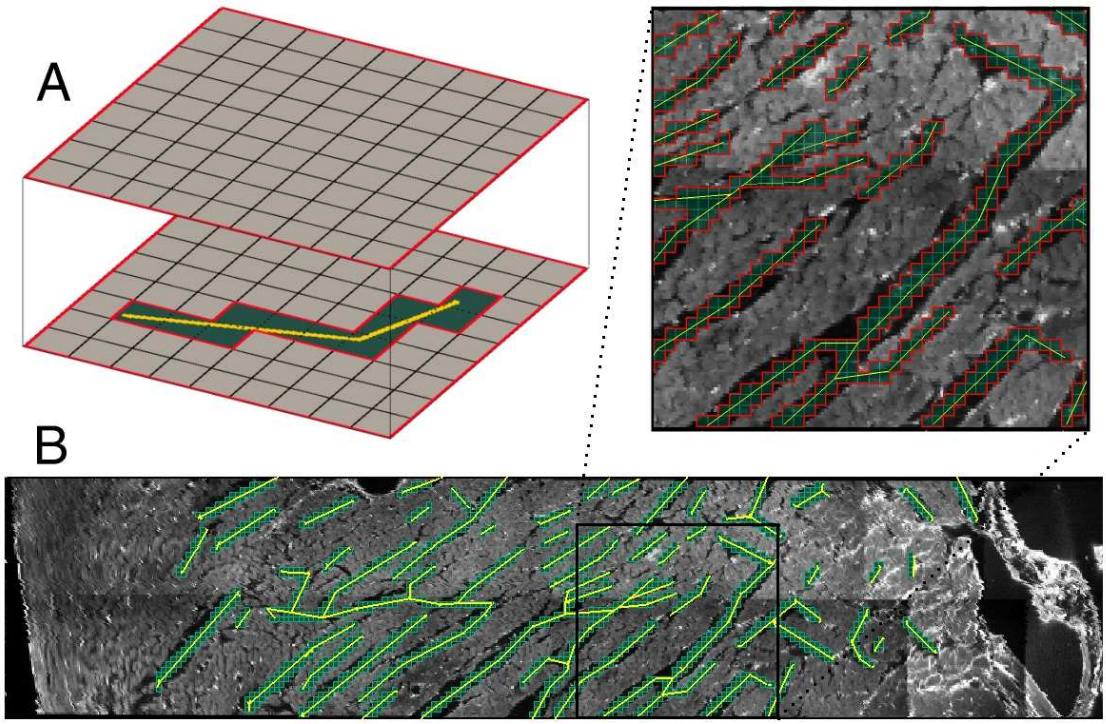

Figure 2.3 *The discontinuous finite element method*

(A) The discontinuous finite element method. The bidomain model describes two domains which co-exist in space – the intracellular (lower plane) and extracellular (upper plane) domains. A discontinuity represented by the yellow lines is introduced into the intracellular domain by the uncoupling of adjacent nodes. Regions of uncoupled nodes are shown in green. No-flux boundary conditions are applied at the perimeter of each domain, as well as internally in the intracellular domain (red lines). (B) Superimposed upon the tissue slice of Fig. 2.2 is a cross-section through the bilinear element description of cleavage planes (shown in yellow) with the corresponding regions of uncoupled nodes (shown in green). Inset shows sub-region at higher magnification, with red lines indicating internal no-flux boundaries as in part A.

2.2.3 Part I: Propagated response

The bidomain equations were solved over a domain extending to the limits of the confocally imaged rat tissue volume. The transmembrane current was described by a simple cubic model (Hunter et al., 1975) to reduce computational expense. In this model, transmembrane ionic current is a cubic function of transmembrane potential, with the function defined by three parameters: resting, threshold, and plateau membrane potentials. The model does not describe any of the features of repolarisation, and can therefore only be used to study activation processes. Neumann boundary conditions were applied along all external boundaries in both intracellular and extracellular domains, and Φ_e was measured relative to position *{x=3,y=0,z=0.8}*, (see Fig. 2.2). The myocardium was stimulated via application of transmembrane current at the centre of the domain, and the propagated response followed in time, until full activation of the volume (~18ms). The discontinuous model was solved on a mesh consisting of 483,840 nodes. In comparison, the continuous model required only 15,360 nodes. Solution time for the discontinuous model was ~85hrs CPU time when running on 8 processors of an SGI Origin 2000 computer, comprising 32 MIPS R10000 CPU units running at 250MHz. For comparison to the results of the discontinuous model (see Fig. 2.5), g_{in} in the continuous model was set at the value (g_{in}^{MIN}) which minimised the *rms* difference between the continuous and discontinuous solutions. For the minimisation the *rms* difference in solutions was plotted against g_{in}, and a cubic function fitted to these data.

2.2.4 Part II: Shock-induced response

A defibrillation strength shock was applied for 10ms duration across the tissue volume. Constant current was applied to the extracellular domain over the epicardial (cathodal) and endocardial (anodal) surfaces of the slab, with uniform density (14mA/cm^2). This induced a large-scale extracellular potential gradient of approximately 1V/mm across the ventricle wall. During the shock, the transmural (not epi- or endo- cardial) boundaries of the rat tissue volume acted to re-distribute current between the extra- and intra- cellular spaces, due to the oblique angle of approach of the myocyte laminae to these boundaries.

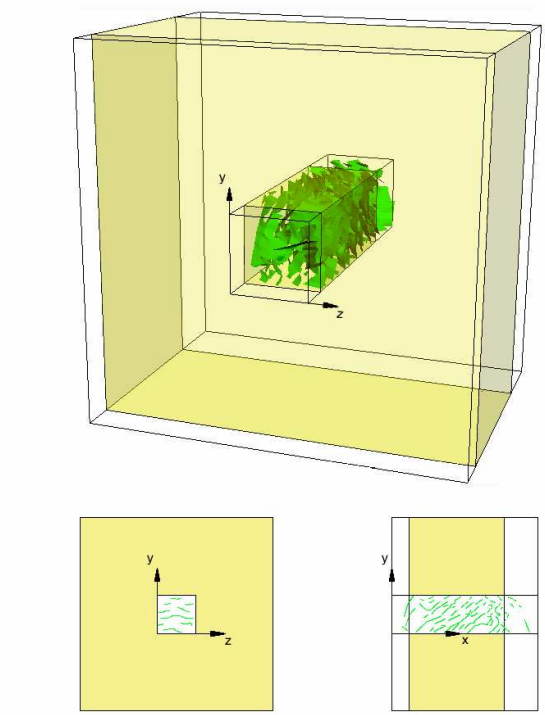

Figure 2.4 *Extension of the rat image volume*

Extended domain used in *Part II* to reduce boundary effects in the vicinity of the cleavage planes. Regions outside of the central rat tissue volume incorporate a continuum description of the transmural cleavage plane angle variation. g_{in}^{MIN} is applied in all yellow regions to best match the conductivity anisotropy present in the central region. The transverse isotropy assumption $g_{it} = g_{in}$ was applied elsewhere, consistent with the observation that there is a much reduced density of cleavage planes in the subepi- and subendo-cardial regions.

To distance the boundary effects from the cleavage plane region, the domain used in *Part I* was expanded as shown in Fig. 2.4. The goal was to allow continuity of current at the transmural boundaries. A continuum description of the myocyte laminae was included in the region outside the rat tissue volume *(outer region)*, whilst the discontinuous description remained in the central region (Fig. 2.4). The optimised cross-laminar conductivity g_{in}^{MIN} determined in *Part I* was applied to the midwall portion of the *outer region* (region shown in yellow in Fig. 2.4), in order to best eliminate any discontinuity in conductivity anisotropy between regions, whilst the assumption $g_{it} = g_{in}$ (transverse isotropy) was applied elsewhere. g_{in}^{MIN} was only applied across the mid-wall section to account for the relative sparsity of cleavage planes in the subepi- and subendo- cardial regions. The simulation utilised the Drouhard-Roberge modified Beeler-Reuter ionic current model (BRDR) (Beeler and Reuter, 1977; Drouhard and Roberge, 1982) which included the revisions of Skouibine et al. (1999). The modifications aimed to stabilise the model at the high transmembrane potentials which develop during shock application. Solution time for the 10ms shock was ~12 hours CPU time.

2.2.5 Model parameters

The necessary conductivity parameters, g_{il}, g_{it}, g_{el}, and g_{et} were selected according to the ratio suggested in the review by Roth (1997). This review is of experimental determinations of g_{il}, g_{it}, g_{el}, and g_{et} which do not pay due attention to the laminar structure of myocardium (Clerc, 1976; Weidmann, 1970; Kléber and Riegger, 1987; Roberts and Scher, 1982). It is not immediately clear whether the suggested values of g_{it} should be applied to g_{it} or g_{in} in our model. Review of the experimental protocols used in determining this parameter, however, suggests that we should apply literature values for g_{it} directly to g_{it} in our model, leaving g_{in} as a free parameter. This is because estimates of g_{it} have been based on potential recordings from the surfaces of various preparations, where cleavage plane discontinuities are absent. All model parameters are given in Table 2.1.

Parameters	Value
General	
g_{il}	0.263 *S/m*
g_{it}	0.0263 *S/m*
g_{in}	variable
g_{el}	0.263 *S/m*
g_{et}	0.1087 *S/m*
g_{en}	0.1087 *S/m*
c_m	10^{-5} *mF/mm²*
cell surface-to-volume ratio	0.2×10^{-3}
resting V_m	-85 *mV*
Cubic Model	
plateau V_m	15 *mV*
threshold V_m	-75 *mV*
membrane conductivity	0.4×10^{-2} *mS/mm²*
BRDR model	
E_{Na}	50 *mV*
g_{Na}	0.04 *mS/mm²*
g_{NaC}	0.3×10^{-4} *mS/mm²*
g_s	0.9×10^{-3} *mS/mm²*

Table 2.1 *Model parameters*

2.3 Results

2.3.1 Part I

The activation sequence following point stimulation at the centre of the rat tissue volume is shown for the discontinuous and continuous models in Fig. 2.5 (A and B respectively). Transmembrane potentials are mapped on seven planes through the heart wall at 2.7ms time increments following stimulation. The discontinuous propagation around the cleavage plane obstacles is evident in Fig. 2.5A from the irregularity in isopotential lines (black lines). Important qualitative differences between the two models are apparent. Firstly, activation in the discontinuous model is markedly asymmetric about the site of stimulation in its early stages. Specifically, comparing both models at 5.4ms, activation

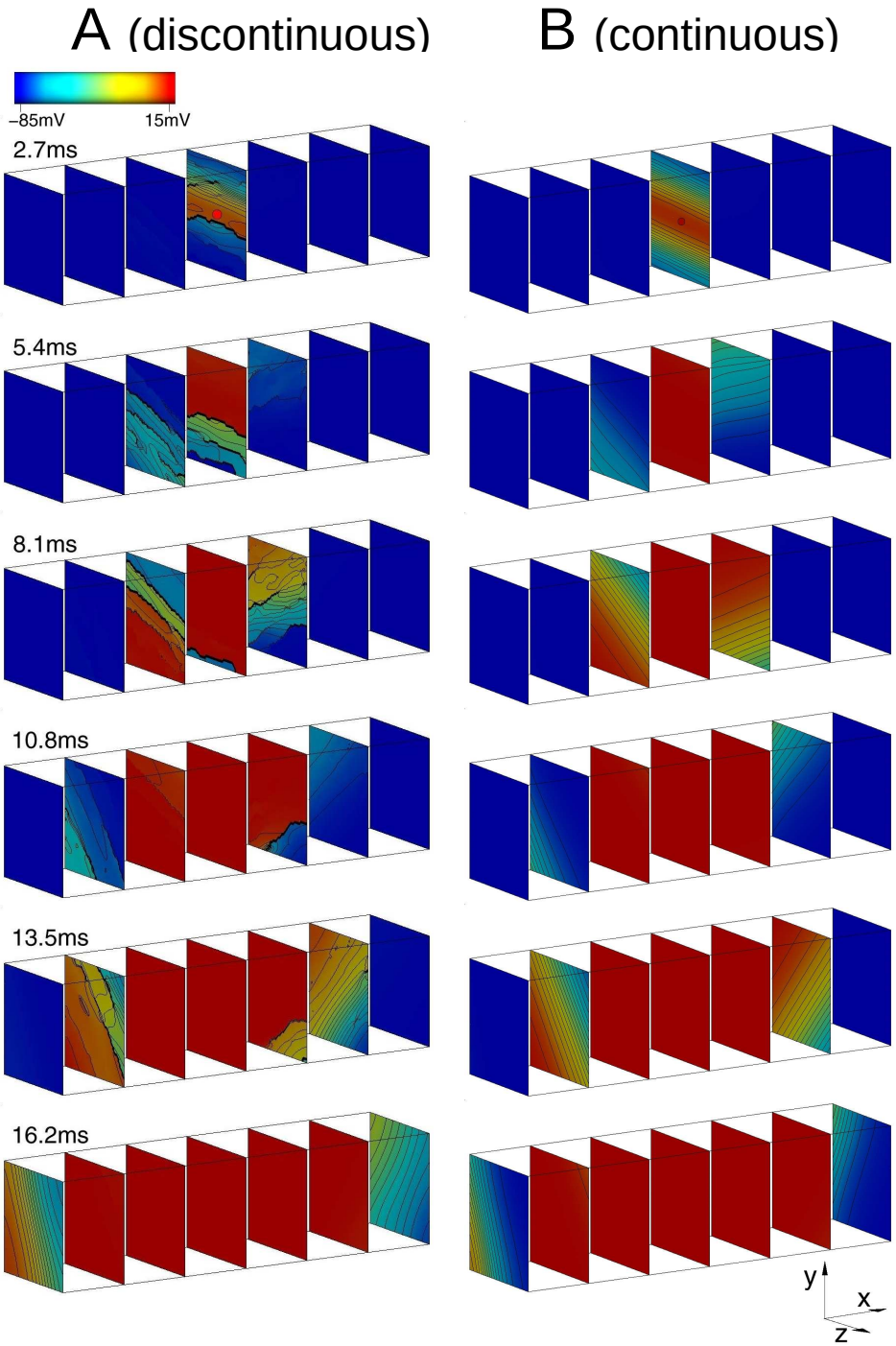

Figure 2.5 *Comparison of models*

Discontinuous model (A) and continuous model (B) activation sequences: transmembrane potentials are mapped on seven equally spaced surfaces through the rat tissue volume. Isopotential lines at 5mV intervals are shown in black. Point of stimulation is shown with the red dot at centre of volume. The cleavage plane obstacles in (A) lead to a highly discontinuous and initially asymmetric form of propagation.

proceeds preferentially upward in the discontinuous model, whereas activation is symmetric about the point of stimulation in the continuous model. Secondly, the insulating boundaries formed by cleavage planes allow the frequent juxtaposition of fully depolarised and non-depolarised tissue regions (see 10.8ms of Fig. 2.5A for an example).

The ability of the continuous model to reproduce the global pattern of excitation is clear in Fig. 2.5B. The conductivity parameter g_{in}^{MIN} used in the continuous model shown in Fig. 2.5B was that which minimised the *rms* difference between the continuous and discontinuous solutions over the 18ms required for full activation of the tissue block. g_{in}^{MIN} was determined to be 0.0107*S/m* giving the ratio g_{it}/g_{in}^{MIN} of 2.44, and a minimised *rms* difference of 5.2mV between the two models. In the optimisation procedure values of g_{in} were applied uniformly over the block in the continuous model. It was apparent however that there were less cleavage planes in the subepi-and subendo-cardial regions compared with the midwall, indicating that the value of g_{in}^{MIN} may be an over-estimate of conductivity normal to myocyte laminae in the midwall. Accordingly, excluding the final 6ms of propagation, (where the wavefront enters subepi- and subendo- cardial regions), from the optimisation procedure acted to reduce the computed value of g_{in}^{MIN} to 0.0080*S/m*, (g_{it}/g_{in}^{MIN} = 3.25, minimised *rms* difference = 4.95mV).

It is well recognised that non-uniformity of wavefront propagation may lead to complex polyphasic (fractionated) extracellular potential recordings (Spach and Dolber, 1986; Steinhaus, 1989; Ellis et al., 1995). To investigate the possibility of fractionation in extracellular recordings from ventricular tissue, extracellular potential waveforms were plotted at 28 sites throughout the rat tissue volume. The signals from the discontinuous and continuous models are shown in Fig. 2.6 (upper and lower panels respectively). All signals are referenced to the point *{x=3,y=0,z=0.8}* and hence approximate unipolar recordings that might be obtained in real tissue. The distance of each recording location from the central site of stimulation is given by the signal colour (red indicating close, and blue indicating far; see Fig. 2.6 legend), whilst the *y* and *z* coordinates of the recording locations are shown above the traces in parentheses. Several observations can be made from these traces. Firstly, nearly all signals from the discontinuous model show some

degree of fractionation. The degree of fractionation appears highest in signals recorded closest to the site of stimulation, a view which is consistent with the activation maps shown in Fig. 2.5. Secondly, it is evident that the downstroke duration (time over which signal derivative is negative) of signals recorded close to the stimulus site is considerably longer in the discontinuous model, than in the continuous model. Downstroke duration was measured by the time required for the downstroke to change from 90% to 10% of its maximum amplitude. The mean duration across red and yellow signals was 7.25 and 2.81*ms* for the discontinuous and continuous models respectively. A comparable difference in transmembrane potential upstroke duration (measured by the time required for the upstroke to change from 10% to 90% of its maximum amplitude) was not seen at the same recording locations (mean times were 3.23 and 2.77*ms* for discontinuous and continuous models).

Traditionally the time of maximum negative slope ($-V'_{max}$) of a unipolar extracellular recording is used to pick the time of activation at the site of measurement (Spach et al., 1972). In the fractionated recordings of Fig. 2.5 there often exists two distinct regions of similar negative slope. To test the ability of $-V'_{max}$ to discern local activation time, we compared the time at $-V'_{max}$ (open circles, Fig. 2.6) with the time of maximum positive slope of the transmembrane potential recording from the same site (closed circles, Fig. 2.6). The two markers of activation are shown on each trace where time differences were greater than the interval used in the slope calculation (0.1ms). Local time of activation was correctly assigned by $-V'_{max}$ in all but two traces of the continuous model. There were comparatively more cases of inaccurate assignment in the discontinuous model, but in only two cases was the error greater than 0.6ms.

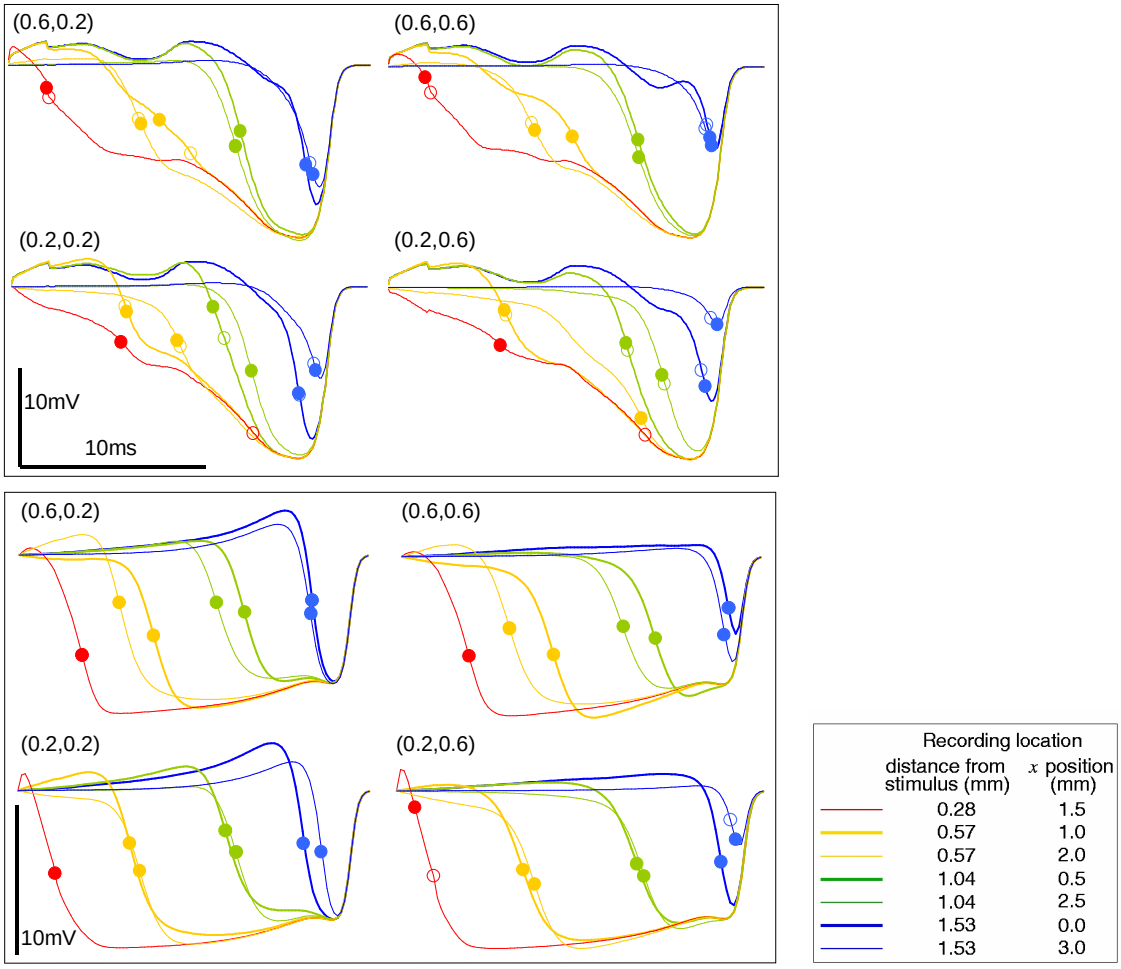

Figure 2.6 *Extracellular potential signals*

Plots of extracellular potential versus time for the discontinuous model (*upper panel*) and continuous model (*lower panel*). Signals are grouped according to their *y*, *z* locations (shown in millimeters, in parentheses above traces). Within each group, the distance from the recording point to the central stimulus site is noted by signal colour (see legend). Open circles indicate the activation time defined by the maximum negative slope of the extracellular potential signal, whereas solid circles indicate the local activation time defined by the maximum positive slope of the transmembrane potential signal from the same site. Where the open circle is not visible it is co-incident with the solid circle. The time scale is the same for both upper and lower panels, however the potential scale varies, as indicated by the scale bars.

2.3.2 Part II

The activation sequence during the shock delivered to the discontinuous model is shown in Fig. 2.7A. Transmembrane potentials are mapped on a single plane ($z=0.4mm$) at each time step, and the colour spectrum scaled to easily distinguish depolarised from hyperpolarised regions. Numerous secondary sources of activation are formed on the endocardial side of the cleavage plane discontinuities. These secondary sources are responsible for activation of the bulk myocardium within the 10ms duration of the applied shock. The results may be compared to those obtained when the transmural shock is applied to a continuous model (Fig. 2.7B). In this case, the optimised cross-laminar conductivity g_{in}^{MIN} determined in *Part I* was applied uniformly throughout the model volume, with the same cleavage plane description used as in the continuous model of *Part I*. Fig. 2.7B shows that the transmembrane potential varies smoothly in the continuous model, and most of the tissue volume remains hyperpolarized during the shock.

The results of the two models may be further examined. Fig. 2.8 shows the three-dimensional architecture of secondary sources in the discontinuous model, 2.5ms into the shock period, by plotting surfaces on which transmembrane potential is equal to –60mV. Fig. 2.9 plots transmembrane potentials along a line drawn through the centre of the reconstructed tissue volume (from epi- to endo- cardium), for both discontinuous and continuous models, at 6ms into the shock. In this graph the full range of transmembrane potentials present in the tissue volume is evident. The transition from depolarised to hyperpolarised regions is smooth in the continuous model. An activation wavefront moving away from the depolarised epicardium is located at ~1mm depth (Fig. 2.9). It is clear from figures 2.7-2.9 that cleavage plane discontinuities facilitate the synchronous activation of a large volume of myocardium during shock application through the formation of localised (secondary) regions of depolarisation.

It is interesting to note that the largest region of secondary depolarisation in the discontinuous model arises at the junction between midwall and sub-endocardial regions

(see Fig. 2.7A, 4ms), where there can be maximal redistribution of current from intra- to extra-cellular spaces due to the lack of further discontinuity towards the endocardium.

2.4 Discussion

Cardiac excitation and contraction have been successfully modelled on global representations of cardiac anatomy for a number of years in our laboratory (Hunter et al., 1997). In this study the well established finite element numerical solution technique was extended to investigate how excitation processes could be influenced by structure at a much finer level. To obtain an accurate representation of the ventricular microstructure for use in the model, it was necessary to image a large volume of myocardium at high resolution. A block of rat ventricular tissue was sequentially imaged and milled to build up the large volume of data required (Young et al., 1998). The data confirmed the growing body of literature pointing to a laminar organisation of myocytes throughout the ventricles. Application of the bidomain equations to the finite element representation of the microstructure yielded interesting insights into the effects that the discontinuities associated with myocyte laminae have on excitation.

This study contributes two observations of primary importance to cardiac electrophysiology. Firstly, it is evident that myocardium may not be electrically isotropic transverse to myofibre direction, as has been uniformly assumed in past studies. Secondly, we have observed that the discontinuities associated with myocyte laminae may be of primary importance in the mechanisms by which fibrillation can be terminated by application of shock to the heart.

2.4.1 Implications for Propagation

Based on pictures of myocardial structure, and measurements of the pathlength a propagating wave might take to traverse cleavage planes, our group has previously conjectured that myocardium may demonstrate orthogonal anisotropy of conductivity

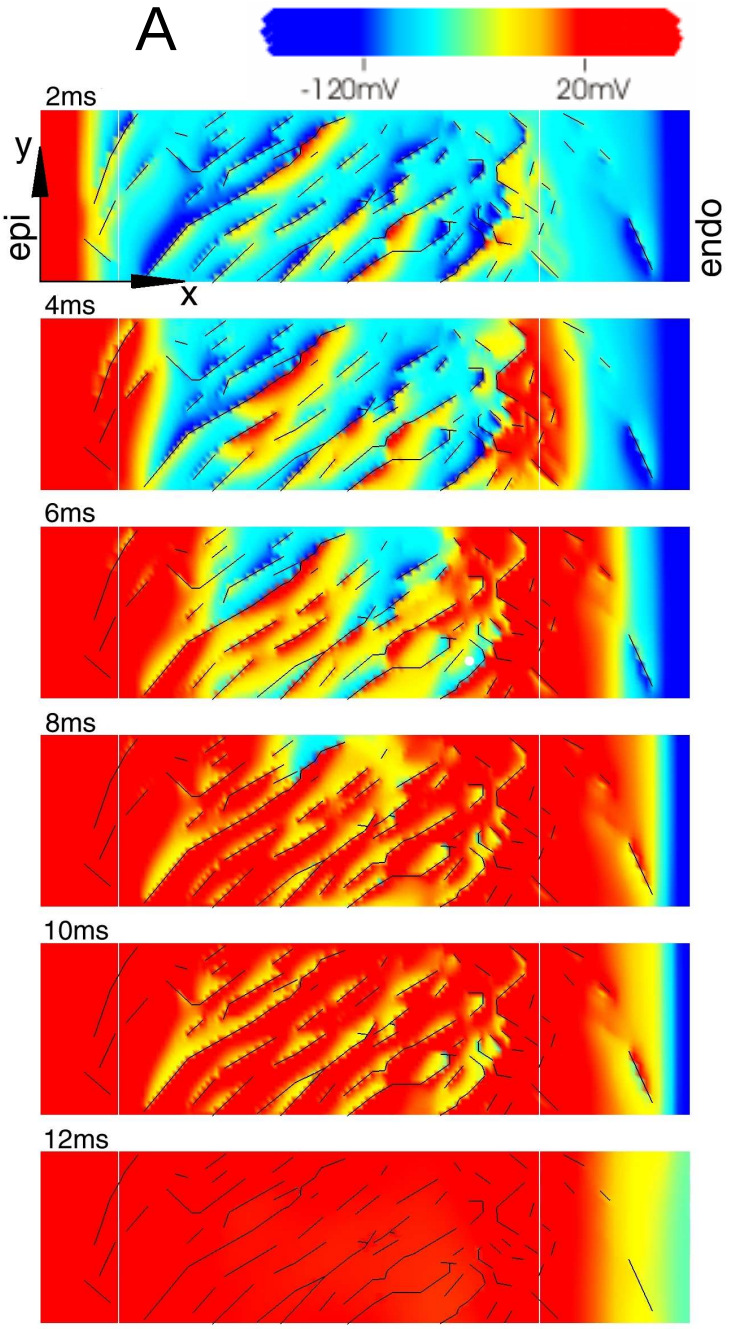
A
-120mV
20mV
2ms
y
epi
x
endo
4ms
6ms
8ms
10ms
12ms

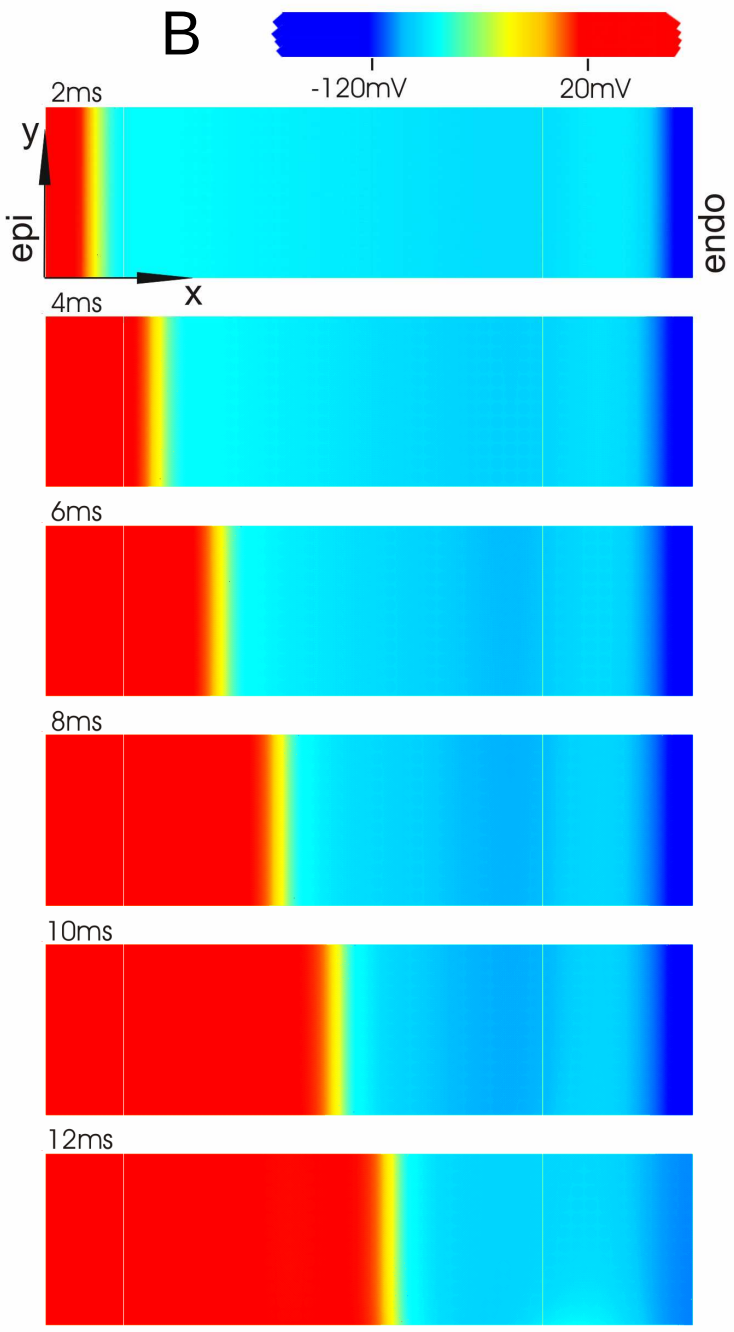

Figure 2.7 *Response to cardioversion* (A) Discontinuous model. (B) Continuous model. Progression of activation during the 10ms of applied shock. Transmembrane potentials are mapped on a single plane (z=0.4mm) at 2ms time increments following onset of shock. The colour spectrum is scaled to emphasise boundaries between depolarised and hyperpolarised regions, and does not cover the full range of potentials within the area shown. In part (A) the black lines depict the cleavage planes discontinuities, and vertical white lines indicate boundaries between the orthotropic and transversely isotropic regions of the model.

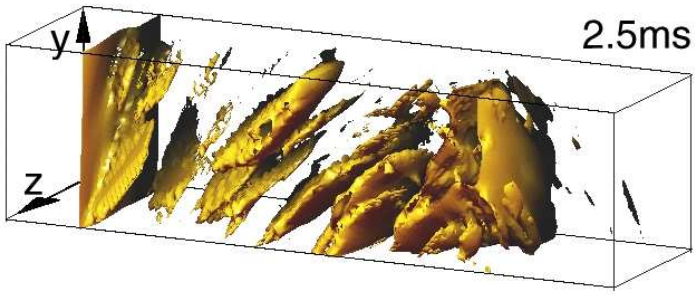

Figure 2.8 *Response to cardioversion – discontinuous model*

Three-dimensional view of secondary sources at 2.5ms into the shock. Isopotential surfaces at -60mV are drawn throughout the tissue volume.

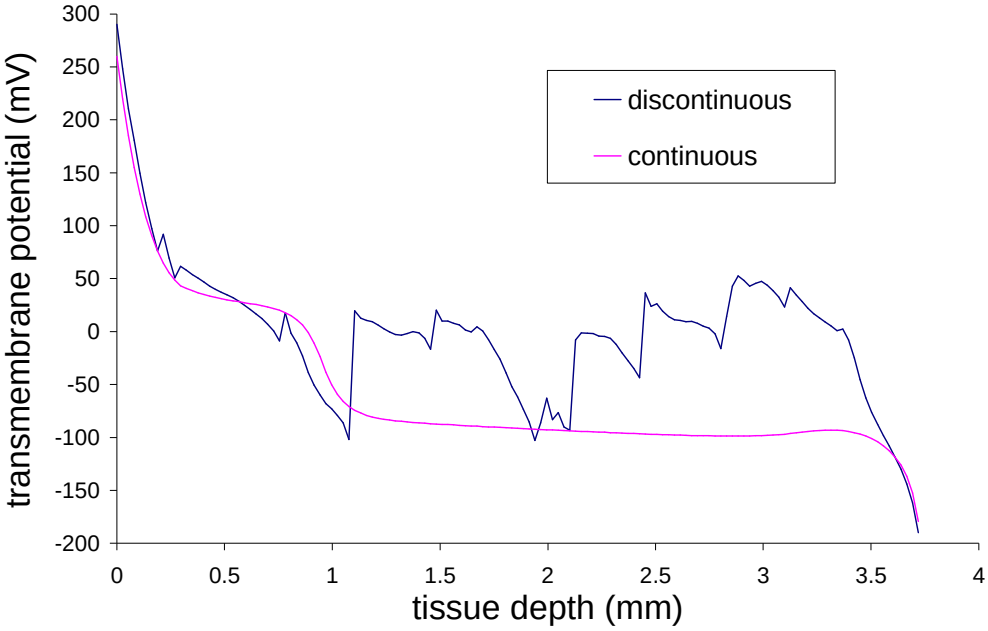

Figure 2.9 *Transmembrane potential profile comparison – discontinuous and continuous models*

Plot of transmembrane potential versus tissue depth (location along *x* axis, see Fig. 2.7) for both models. Potential varies smoothly in the continuous model, and much of the tissue remains hyperpolarized. In the discontinuous model cleavage plane obstructions to intracellular current flow lead to multiple inflections on the potential profile, and depolarised regions exist throughout most of the tissue volume.

(LeGrice, 1992). Pathlength measurements do not, however, take into account the possibility that direct stimulation of myocardium may occur across cleavage planes due to current flows in the extracellular domain. In fact, a wavefront may traverse a gap between two completely disconnected intracellular spaces by such electrotonic effects. The propensity for this form of propagation increases, whilst the delay of propagation at the gap reduces, with reduced extracellular conductivity. Under physiological extracellular conductivities however, the delay is sufficient to slow propagation in the direction normal to myocyte laminae. Our calculated ratio g_{it}/g_{in}^{MIN} was 3.25 for propagation in the midwall. Pathlength measurements have previously suggested a ratio of propagation velocities c_t/c_n of 2 in the midwall (LeGrice, 1992). To compare these results we use the relationship (Plonsey and Barr, 1988).

$$\frac{c_t}{c_n} = \sqrt{\left(\frac{g_{en}+g_{in}}{g_{en}g_{in}}\right)\left(\frac{g_{et}g_{it}}{g_{et}+g_{it}}\right)} \tag{2.24}$$

and find that we measure c_t/c_n to be 1.68. It is expected that direct stimulation of myocardium across cleavage planes via current flow in the extracellular domain would act to reduce the degree of anisotropy estimated on the basis of pathlength alone. Of course it must also be remembered that the pathlength measurements were carried out in two-dimensional dog heart tissue sections (LeGrice, 1992), whereas the present study uses a three-dimensional representation of rat myocardium.

In addition to conduction velocity anisotropy, we expect discontinuous propagation in the ventricle to be indicated by a number of other measures. Polyphasic extracellular potential waveforms have previously been observed in human ventricular tissue (Durrer et al., 1954), human atrial pectinate muscle bundles of increased age (Spach and Dolber, 1986), and in infarct border zone or ischaemic regions of myocardium (Gardner et al., 1985). Our results indicate that extracellular recordings from sites close to a midwall focal stimulation, in healthy ventricular tissue, may also exhibit complex multiple inflections. These recordings may also show a much reduced rate of downstroke than previously expected. These two characteristics may lead to inaccurate assignment of the local time of activation based on the maximum negative derivative of the extracellular

signal. Attempts have been made to use more of the shape information contained within an extracellular potential recording in order to determine activation time more precisely (Di Persio and Barr, 1987; Ganapathy et al., 1985; Ellis et al., 1996). The disadvantage of these approaches is that they rely on a priori knowledge of tissue parameters such as action potential shape and electrode to tissue distance, together with interstitial and intracellular resistivities.

We also expect that the discontinuous structure of the ventricle will give rise to preferential directions of propagation following point stimulation which may lead to a wavefront which is asymmetric about the site of stimulation. Such propagation is likely to be particularly important in the early development of a wavefront from a site of ectopic activation in the ventricle. We have commenced preliminary studies to investigate the presence of the above indicators of discontinuous propagation, utilising arrays of extracellular plunge electrodes in an experimental pig heart model. Preliminary data indicates a high level of correspondence between the model predictions and experiment (see *Chapter 5*).

2.4.2 Implications for Defibrillation

Over the past decade, a multitude of mechanisms by which an applied shock to the heart may alter transmembrane potential have been elucidated. There has been a concerted search for the mechanisms through which shock during fibrillation may permit the simultaneous resetting of a considerable volume of myocardium. This study presents striking evidence that myocardial cleavage plane discontinuities may in fact be a dominant factor in facilitating such synchronous resetting of myocardium. Our view of how defibrillation works, and how it should be accurately modelled is likely to be changed on the evidence presented here.

The term “virtual electrode” is now common jargon used to refer to any site of shock-induced transmembrane potential change distant from the site of current injection. It has been shown that virtual electrodes may be induced by unequal anisotropy of intra- and

extra- cellular spaces (Sepulveda and Wikswo, 1987), myofibre curvature (Trayanova and Skouibine, 1998), fibre narrowing (Sobie et al., 1997), spatial inhomogeneity of intra-cellular volume fraction (Fishler, 1998), and discontinuity associated with gap junctions (Trayanova, 1996) and inter-cellular clefts (Fast et al., 1998). Any geometrical condition which induces current redistribution across the cell membrane during stimulation will lead to formation of a virtual electrode. The present day challenge is to ascertain how all these mechanisms impact on the ability of a shock to terminate fibrillation.

It may be asserted that the most important form of structural discontinuity in terms of cardioversion is the inter-laminar cleavage plane, not the gap junction. Modelling studies of gap junction induced virtual electrodes have indicated spatial fluctuations in transmembrane potential of a few millivolts (Trayanova, 1996), however these "sawtooth" patterns have not been seen experimentally, despite considerable effort (Gillis et al., 1996). There is further previous evidence for the assertion. Frazier et al. (1988) measured the threshold required for diastolic cathodal point stimulation in the midwall, during diastole to be 0.8V/cm. Krassowska et al. (1990) were forced to assign discontinuity at the level of bundles of myocardial fibres rather than gap junctions to match this value in their discontinuous syncytial model of myocardium. The present structural model incorporates transmural fibre rotation, unequal anisotropy, as well as structural discontinuity. Under conditions of uniform field stimulation, it is the cleavage plane discontinuities which are responsible for the activation of the bulk of the myocardium within the duration of the shock. It is expected that a shock applied to the body surface will induce a relatively uniform current density field within the myocardium. The shock field from an implantable cardioverter-defibrillator (ICD) is likely to be less uniform, however, and the relative role of structural discontinuity in this form of far-field stimulation remains to be investigated. In the setting of non-uniform field stimulation, unequal anisotropy between intra- and extra-cellular spaces can by itself generate virtual electrodes in the form of a dog bone shape of polarisation, with adjacent regions of opposite polarisation (Sepulveda and Wikswo, 1987). It is interesting to note that the experimental studies confirming these patterns (Wikswo et al., 1995; Knisley,

1995) have been carried out on the epicardial surface of the heart, where coupling between myocytes is increased with respect to the midwall, and large inter-cellular clefts are absent. Whether a dog-bone pattern of polarization is in fact visible at all deep within the midwall during non-uniform field application remains to be seen.

As with the propagation section of this study, it would be desirable to be able to observe far-field stimulation effects in a three-dimensional experimental model. Currently no technique is available that is able to map transmembrane potential at sufficient resolution through large volumes of myocardium to achieve this. The development of a transmural probe able to record transmembrane potentials deep within myocardium (see *Chapter 3*) may yield experimental information on these processes, albeit at a lower spatial resolution than the scale of discontinuity involved.

2.4.3 Limitations of the study

The most severe limitation of this work stems from the restricted volume over which the cleavage plane geometries could be imaged. The length of the rat tissue volume from epi- to endo- cardial surfaces was 3.75 times its width, which resulted in the propagating wavefront reaching the transmural extents of the tissue block in the early stages of propagation from the central stimulus site (see Fig. 2.5). The presence of the transmural boundaries acts to reduce the available paths of propagation around the cleavage plane obstacles, in turn enhancing the effect of the cleavage planes on the slowing of propagation. As a result it is likely that we have obtained an over-estimate of g_{it}/g_{in}^{MIN} for this tissue block. The boundary effect does not, however, change our overall conclusion that $g_{in} < g_{it}$; the effects of this anisotropy can be seen in the tendency of earliest activation to skew towards the edges *(y=0, z=0)* and *(y=0.8, z=0)* on the epi- and endo-cardial surfaces respectively (see Fig. 2.5A).

It is evident from Fig. 2.2 that some cleavage planes extended across the full width of the reconstructed rat tissue volume. Study of larger volumes of tissue will allow us to reconstruct the full extent of single cleavage planes, and may yield further insights into

the possible role of the laminar organisation of myocytes in providing a substrate for re-entrant activity under conditions of depressed conduction.

Initially *Part II* of the study was carried out using just the rat tissue volume. The transmural boundaries acted to redistribute current between intra- and extra- cellular spaces to an extent that obscured the secondary sources of activation at the cleavage plane discontinuities. In order to reduce these boundary effects and better approximate the behaviour of tissue within an intact ventricle, it was necessary to enclose the cleavage plane region with a region were cleavage plane orientation was represented by a continuous description. Ideally, we may wish to examine the effects of cleavage planes on defibrillation by establishing a re-entering wavefront within the discontinuous model, and examining the conditions required for termination of re-entry. However, both the volume of imaged rat tissue, and the computational expense of such a model (with our current computing resources) precluded this approach. Acquisition of the extended confocal image was highly labour intensive, and in order to image larger volumes of tissue in reduced time we are currently developing an automated approach to this imaging process.

As indicated in Fig. 2.3A, the finite element model made a piecewise cube approximation to discontinuities in the intracellular space. This representation gave rise to the artifact that the gaps between adjacent myocyte laminae had a volume which was determined by the resolution of the finite element mesh. For example, in the discontinuous model of *Part I* a total of 483,840 nodes were used, giving trilinear element dimensions of 0.014 x 0.017 x 0.017mm. This resulted in ~11% of the total intracellular domain being removed from the solution (assigned as “gap space”). It is suggested from studies of collagen volume fraction in normal rat ventricle that connective tissues may constitute approximately 3-4% of the total ventricular volume (Weber et al., 1990). Not all of this collagen volume would be expected to lie between myocyte laminae. Thus our model may over-estimate the fractional volume of the gaps between myocyte laminae. Further refinement of the mesh used, however, was prohibited by computational time.

Interestingly, there is growing evidence that direct electrical communication between myocyte and fibroblast cell populations in the sino-atrial node may be important in regulation of heart rate (Kohl et al., 1999). Our study does not consider any possible role of such connective tissue cells in directly transmitting current between myocyte laminae.

A further assumption of our model is that extracellular conductivity is isotropic transverse to myofibre direction (ie. $g_{et}=g_{en}$). The close relationship between myocyte and collagen networks (Young et al., 1998) suggests that the extracellular space is likely to exhibit orthogonal anisotropy along the same microstructural axes as its intracellular counterpart. The model gave no means of testing this prediction, however.

The application of this work to the human heart requires experimental quantification of cleavage plane geometries in healthy and diseased human hearts. To date no such analysis has been carried out; we base our understanding of the laminar organisation of myocytes from measurements taken from rat (Young et al., 1998), dog (LeGrice et al., 1995), and pig hearts (unpublished observations).

2.4.4 Conclusions

We have shown that the discontinuous laminar organisation of myocytes in the ventricle has important implications for electrical propagation and cardioversion. Our structural finite element model indicates that the laminar organisation may define orthogonally anisotropic conductivities about microstructurally defined axes. Furthermore, we have shown effects of the structural discontinuity on propagation from a focal activation in the midwall, and on an applied defibrillation-strength shock across the ventricular wall.

Chapter 3

Intramural multisite recording of transmembrane potential in the heart

(printed in similar form in *Biophysical Journal*, 2001, 81:2671-2680)

Abstract

Heart surface optical mapping of transmembrane potentials has been widely used in studies of normal and pathological heart rhythms, and defibrillation. In these studies, three dimensional spatio-temporal events can only be inferred from two dimensional surface potential maps. We present a novel optical system which enables high fidelity intramural recording of transmembrane potentials. A probe constructed from optical fibres is used to deliver excitation light to, and collect fluorescence from, 7 positions, each 1mm apart, through the left ventricle wall of the rabbit heart. Excitation is provided by the 488nm line of a water-cooled argon-ion laser. The fluorescence from each tissue site is split at 600nm, and imaged onto separate photodiodes, for later signal ratioing. The optics and electronics are easily expandable to accommodate multiple optical probes. The system was used to record the first simultaneous measurements of transmembrane potential at a number of sites through the intact heart wall.

3.1 Introduction

The first intramural recordings of cardiac electrical activation were made by Durrer and Tweel (1953). They used purpose-built hypodermic needle probes, with which extracellular potentials were measured at sites along the needle, via ultra fine wires introduced through its lumen. Their technique has since been used by a number of investigators (Selvester et al., 1970; Kerber et al., 1994; Sands et al., 1999). By increasing the number of needles inserted through the heart wall, the transmural spread of electrical activation has been mapped in three dimensions, revealing details of normal and arrhythmic propagation (Chen et al., 1988; Frazier et al., 1988; Arnar et al., 1997).

There are problems, however, in relating extracellular potential signals to underlying cellular electrical activity. Extracellular signals represent the integrated effects of membrane currents over a relatively large volume and distinguishing near from far electrical events is often difficult. As a consequence, activation and recovery, the two most basic characteristics of propagation, cannot be identified reliably at the site of recording for conditions other than uniform propagation (Steinhaus, 1989).

Over the past two decades, optical measurement of transmembrane potential has provided an increasingly attractive option for cardiac electrical mapping studies. Optical mapping has distinct advantages over extracellular techniques. Foremost is the ability to interrogate cellular propagation directly by imaging transmembrane potentials. With optical mapping it is possible to achieve high spatial resolution. It is also possible to map potentials during the application of defibrillating shocks to the heart, when conventional electrical measurement techniques cannot be used. To date, however, optical measurement of transmembrane potential has been almost entirely restricted to the heart surfaces. The ability to access deeper propagation processes has in general been limited by scattering and absorption of the voltage-dependent fluorescence signal (Girouard et al., 1996). Recently, electrical activity inside cardiac muscle has been visualised via fluorescence measurements made in a trans-illumination mode (Baxter et al., 2001). This

technique currently offers a low degree of spatial resolution through the wall of the heart however, and is not applicable to the study of intact heart preparations.

We have developed a novel optical system for measuring intramural cardiac action potentials. Our main objectives were to record ventricular membrane potentials at sites with transmural separation comparable to extracellular needle probes, using a system which could readily be expanded to map the 3D spread of electrical activation through the ventricular wall. These objectives were met with the design (i) of a robust, small diameter, optical probe (optrode) able to deliver and collect light deep within tissue and (ii) of a modular (scalable) recording complex capable of simultaneous measurement of fluorescence signals and extracellular potentials. Dual wavelength collection of di-4-ANEPPS emission was used to reduce light source noise and motion-related artifact, in a ratiometric fashion similar to that reported by Knisley et al. (2000).

3.2 Methods

3.2.1 Optics

A schematic representation of the optical system is given in Fig 3.1A. Excitation light (488nm) from a water-cooled argon ion laser (Spectra Physics; model 165) was delivered to separate tissue sites via a fibre optic conduit which terminated in a purpose-built optical probe *(optrode)*. Fluorescence collected from each site returned through the "tissue" conduit and was split into two frequency bands. Long and short wavelengths were routed to discrete photodiodes via separate fibre optic "detector" conduits. Aspects of the optical design are similar to the tissue culture imaging system of Rohr and Kucera (1998).

Each conduit consisted of 7 optical fibres. These were packed in hexagonal bundles toward the centre of the optical system to optimise coupling of excitation light into the tissue conduit and fluorescence emission into the detector conduits. The central ends of

the fibre optic conduits are subsequently referred to as the “tissue bundle” and “detector bundles A and B”.

The tissue bundle was formed within an SMA fibre-optic connector (Thorlabs Inc.), and mounted in a multimode fibre coupler (F-91-C1-T; Newport Corporation) which allowed

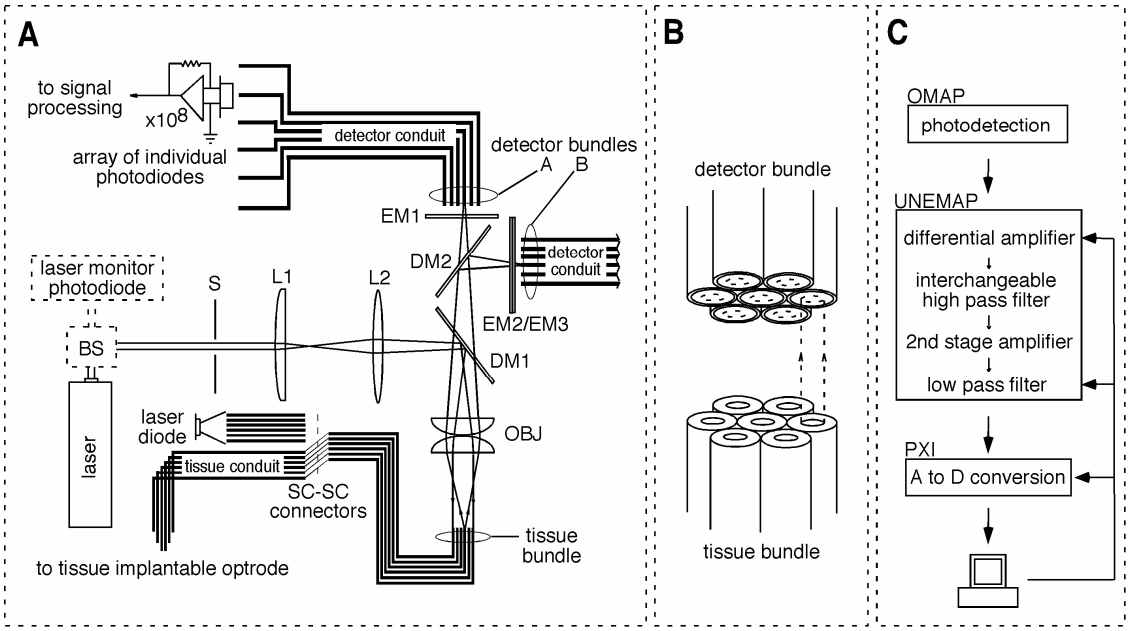

Figure 3.1 *The optical recording system*

(A) Schematic overview of the optical layout. See text for detailed description. L1 and L2, focal length 50mm and 80mm converging lenses; OBJ, 10x microscope objective; DM1 and DM2, 520nm and 600nm long pass dichroic mirrors; EM1 and EM2, 600nm and 520nm long pass emission filters; EM3, 600nm short pass emission filter; S, shutter; BS, beam steerer. (B) Schematic of the coupling of fluorescence from the tissue bundle to a detector bundle. The fibres of the detector bundles have an increased ratio of core:outer diameter which leads to greater coupling efficiency and easier alignment. For simplicity the objective lens has been omitted. (C) Schematic overview of the system electronics. Design is based around the three units: OMAP, UNEMAP, PXI (see text for details). Arrows to and from the computer represent data input and digital control lines respectively.

XYZ positioning as well as rotation about the bundle central axis. The detector bundles were mounted in fibre optic positioners attached to translation stages (FP-1, Model 426; Newport Corporation) for accurate placement. The end faces of all fibre bundles were manually polished.

Light from the laser was coupled into the tissue bundle by the lenses L1 and L2, a 520nm long-pass dichroic mirror (DM1) and a 10x microscope objective (OBJ). Beam diameter was varied, to ensure optimal coupling to tissue bundles of various dimensions, by adjusting the distances L1-L2, and L2-OBJ. The lenses and objective were positioned so that the laser beam was in all cases collimated at the face of the tissue bundle.

The tissue bundle was imaged onto the detector bundles via the objective OBJ. Return fluorescence was split by the 600nm long-pass dichroic mirror (DM2) and further band-limited by the emission filters EM1(>600 nm) and EM2/EM3 (520-600nm). Each detector fibre terminated with an SMA connector for coupling to the photodetection system.

Optimal mapping of the tissue bundle image onto the detector bundles was achieved as follows. The optrode was immersed in a fluorescent solution and the ratio $\Sigma A_i/\Sigma B_i$ was monitored continuously - A_i and B_i are the fluorescence levels recorded through individual fibres of detector conduits A and B. Firstly, detector bundle B was fixed in position, and detector bundle A was adjusted to maximise $\Sigma A_i/\Sigma B_i$. Detector bundle B was then moved, with bundle A fixed, until the ratio reached a minimum. The use of this ratiometric approach in the alignment procedure enabled us to reduce errors due to bleaching of the fluorescence signal and laser power fluctuation.

Cross-talk (defined as the fraction of total detected fluorescence power from any tissue fibre detected by photodiodes not assigned to that fibre) was used as a measure of the effectiveness of optical coupling in the system. Ideally, there should be one to one mapping between tissue fibres and associated detector fibres. However, cross-talk may arise from the diffraction limitations of the objective lens, different bundle geometries, or

from bundle misalignments. Cross-talk could not easily be determined with the optrode attached to the tissue bundle. A join was therefore added to the tissue conduit with a series of SC-SC fibre connectors (Thorlabs Inc.) so that cross-talk could be evaluated by reverse illumination of individual fibres in the tissue conduit with a laser diode.

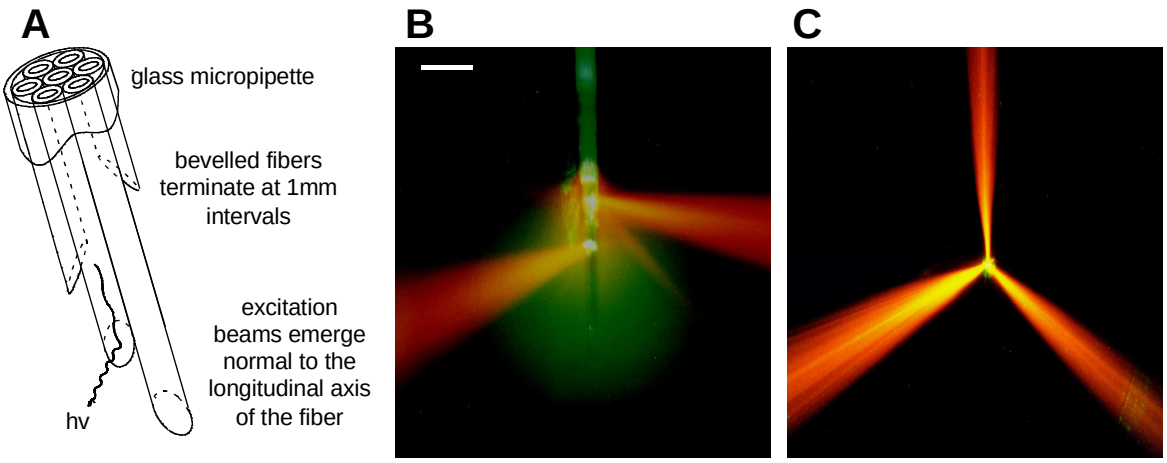

Figure 3.2 *The optrode*

(A) A schematic of the tissue implantable optrode (not drawn to scale). Seven optical fibres are arranged in a hexagonal array, and terminate at 1mm intervals. All fibres are enclosed in a glass micropipette. Light emission is from the side of the fibres by total internal reflection off their bevelled ends. (B and C) Photographs of the optrode in side and end-on views. Optrode is immersed in a fluorescing rhodamine solution. The green halo surrounding the optrode in (B) is caused by reflection of the beam which propagates into the page. For illustrative purposes only three of the seven optrode fibres carry excitation light. Scale bar at top of Part B indicates 2mm.

3.2.2 Optrode

The distal end of the tissue conduit formed the optrode. The buffer coatings of the conduit fibres were removed at the optrode end to reduce their size. Fibres were then hexagonally arranged, and terminated at 1mm intervals (Fig. 3.2). The end of each fibre

was polished at 40^{o} to its longitudinal axis to produce total internal reflection of excitation light and collected fluorescence at this face. A glass-air interface is required for total internal reflection, and for this reason the fibres were loaded into a glass micropipette plugged with epoxy resin at its tip. This construction also adds strength to the probe and aids in cleaning following experiments. Fibres were oriented so that excitation light was emitted radially from the optrode: the principal direction of emission (and collection) for successive fibres being separated by 60^{o} to minimize reflective losses at the micropipette surfaces. The micropipette was pulled manually to a gradual taper to ease insertion into the tissue. The total diameter of the optrode was approximately 400μm. Fig. 3.2 shows the pattern of illumination obtained when three of the seven optical fibres of the optrode were illuminated during immersion in a dilute solution of sulforhodamine B.

3.2.3 Optical Fibres

Separate tissue conduits were fabricated in order to compare the performance of two different types of optical fibre: GIF625[1] (Thorlabs Inc) and F-MCB-T (Newport Corp). FT-1.0-EMT fibres (Thorlabs Inc) were used for the detection conduits. Specifications for all three optical fibres are given in Table 1. A water-clear optical epoxy (Epoxies Etc…, Cranston, RI) was used to bond the hexagonally packed fibre bundle at the proximal end of the tissue conduit. Non-transparent epoxies did not remain intact when exposed to the intense laser beam.

The outer diameter of the detector fibres determines the magnification required to match the image of the tissue bundle to the detector bundle. In principle, alignment safety factors, and imaging efficiency should be increased, if tissue fibres with a small core to outer diameter ratio are mapped onto detector fibres with a much larger core to outer diameter ratio (see Fig 3.1B). On the other hand, the efficiency of coupling of excitation light into the tissue bundle will decrease markedly if core to outer diameter ratio is

[1] GIF625 is a standard communication graded index fibre

reduced. The buffer coating of the proximal ends of the GIF625 tissue fibres and the detector fibres (but not the F-MCB-T tissue fibres) was removed over the first 100mm in order to achieve appropriate core to outer diameter ratios (see Table 3.1). The ratio for the F-MCB-T fibre was most appropriate with the buffer coating left intact. However, leaving the buffer intact on this fibre lead to unforeseen contamination of the tissue fluorescence with fluorescence from the buffer coating. In order to overcome this problem whilst retaining the desired ratio, only the first 2mm of the buffer was etched from the F-MCB-T fibres. This shifted the buffer fluorescence away from the focal plane of the large core fibres. The etching was carried out with concentrated sulfuric acid at 140^{o}C.

Bundle	Name	Type	Diameter (μm)			Core:outer diameter ratio	Excitation efficiency (%)	Cross-talk mean (SD) (%)
			core	cladding	buffer			
tissue	GIF625	graded index	62.5	125*	250	0.5	4	1.79 (1.47)
	F-MCB-T	step index	100	110	140*	0.71	26	0.39 (0.13)
detector	FT-1.0-EMT	step index	1000	1035*	1400	0.97		

Table 3.1 *Optical fibre specifications and characteristics*
The various optical fibre types and their specifications. GIF625 (Thorlabs Inc.) and F-MCB-T (Newport Corp.) were the fibres trialed in the tissue conduits, while FT-1.0-EMT was used in the detector conduits. The fibre outer diameter (*) was the cladding diameter in cases where the buffer coating was removed. Use of F-MCB-T enabled greater excitation pathway efficiency. Cross-talk for the F-MCB-T bundle was lowest due to its more regular bundle geometry.

3.2.4 Signal acquisition and processing

The acquisition system consists of three modules as illustrated in Figure 3.1C. In the photodetection module, SMA connectors were used to couple detector fibres directly to photodiodes (S2386-44K; Hamamatsu Photonics) mounted in columns on the front

panels of the unit. The photodiodes were connected to current-voltage converters (gain = 10^8 V/A), (OPA121KU; Burr-Brown).

The photodetection system was interfaced with a multi-channel signal conditioning complex (UNEMAP; Auckland Uniservices Ltd, Auckland) which provided programmable gain (1 to 1100), and a 5-pole programmable low-pass filter (50Hz - 4950kHz). Optical signals were low-pass filtered at 500Hz to prevent aliasing. Optional high-pass filtering (0.05Hz) was available for the recording of extracellular potential signals.

Data was acquired with 16 bit resolution at 1.2kHz per channel using a National Instruments™ PXI acquisition system. This consisted of four 64 channel PXI-6031E acquisition cards in a PXI-1000B chassis controlled by a master SGI 02 (Silicon Graphics Inc) computer workstation. Data acquired by the PXI system was transferred to the SGI workstation for further processing and display.

A model of each recorded signal may be constructed as follows:

$$tissue\ signal + \text{fibre signal} = \alpha V_m(t)I(t)V(t)C(t) + \beta I(t)V(t)C(t) + \gamma \text{I(t)} \tag{3.1}$$

where $V_m(t)$ is the membrane potential, $I(t)$ the laser intensity, $V(t)$ the volume of recording, $C(t)$ the concentration of fluorochrome, and α, β, and γ are constants. The fibre signal was small in comparison to the tissue signal, and arose from laser light reflected off the polished tissue bundle (a small fraction of which leaked to the detectors), and fibre generated fluorescence. Prior to an experiment the constant γ was determined for each channel with the optrode held in air. The laser intensity $I(t)$ was monitored continuously with a single photodiode (see Fig 3.1A). This recording of laser power typically showed peak to peak fluctuations of up to 1.1% of total laser power. The recording was scaled and used to subtract the fibre signal component from each recording made in the heart tissue. Subsequently, the pair of signals generated from each recording site (520-600nm, and >600nm) were ratioed as below:

$$signal\ ratio = \frac{signal_1}{signal_2} = \frac{I(t)V(t)C(t)[\alpha_1 V_m(t) + \beta_1]}{I(t)V(t)C(t)[\alpha_2 V_m(t) + \beta_2]} \quad (3.2)$$

Provided the bleaching characteristics of each signal are the same (that the α and β terms of Eqn 3.2 are time-independent constants), the signal ratio may be reduced to a function dependent on $V_m(t)$ and constants only.

3.2.5 Experimental preparation

The optical recording system was tested on Langendorff-perfused rabbit hearts (n=3). All procedures were approved by the University of Auckland Animal Ethics Committee under approval #N805. New Zealand White Rabbits (2.5 - 6kg) were anaesthetised with saffan and their hearts rapidly excised. Hearts were perfused with Kreb's solution containing (in mM) NaCl 120, KCl 4.7, KH_2PO_4 1.2, $MgSO_4$ 1.2, D-glucose 11, $NaHCO_3$ 25, $CaCl_2$ 1.8, bubbled with 95%/5% O_2/CO_2, at an aortic pressure of 100mmHg, and a temperature of 37^{o}C. The heart was stained with recirculating di-4-ANEPPS at 20μM, for 10 minutes and left to equilibrate for a further 10 minutes. The optrode was then inserted into the free wall of the left ventricle (LV) at an angle (approximately 20^o to the epicardium) which allowed all recording sites to be located intramurally. Each optrode fibre delivered 10mW excitation power to the heart tissue. In order to investigate the efficacy of signal ratioing in the reduction of motion artifact, recordings were made with and without the addition of 2,3-butanedione monoxime (2,3-BDM, 15mM) to the perfusate, in two hearts. All recordings in the third heart were made with 2,3-BDM. The heart was paced at the base of the right ventricle at 1.5 times threshold during recordings, and the electrical function of the heart was monitored using a bipolar epicardial electrode placed as close as practical to the optrode insertion site.

3.3 Results

3.3.1 System Efficiencies

The major losses in the excitation optical pathway occurred at the face of the tissue bundle. Fig. 3.3 shows a segment of the tissue bundle illuminated by the laser beam. The beam intensity has a 2D Gaussian density distribution

$$f(r) = \frac{1}{2\pi\sigma^2} e^{-\frac{1}{2}\left(\frac{r}{\sigma}\right)^2} \tag{3.3}$$

where r is the radius from the centre of the beam, and σ is the standard deviation (SD) of the beam intensity profile. The fraction of the laser beam which falls on the fibre cores of the tissue bundle can be estimated by evaluating the integral

$$\iint f(r) dr r d\theta \tag{3.4}$$

between the limits set by the fibre dimensions.

This equation was numerically evaluated with increasing beam standard deviations. Results for the F-MCB-T fibre bundle are presented in Fig 3.3. As expected, the total efficiency of coupling of the laser beam to the tissue bundle reduces as beam diameter is expanded, while the uniformity of coupling to all seven fibres in the bundle is increased. Efficiency is defined as the percent of total laser power incident to the bundle that may be coupled into the fibre cores, whilst uniformity is defined as the ratio of average power carried by the outer fibres to the power carried by the central fibre. Coupling efficiency for the outer fibres of the bundle, peaks at a beam SD of approximately 100μm, and this is the beam SD currently used. The total loss of laser power associated with coupling into the tissue bundle and propagation through the tissue fibres can be measured directly for this beam SD. Results are shown as single data points in Fig. 3.3. It is evident that there are significant losses, additional to those due to illumination of non-core parts of the tissue bundle. A major fraction of this loss is likely due to degradation of the surface

polish at the face of the bundle, caused by the acid etching of the F-MCB-T fibre buffer. Theoretical losses through the fibres themselves are low (0.014dB/m). The overall efficiency of the excitation pathway, including losses through the coupling lenses, is shown in Table 3.1, for both types of tissue fibre. It is seen that use of the F-MCB-T fibre considerably increases the excitation efficiency of the system, and for this reason it was the fibre used in all animal experiments.

3.3.2 Fibre bundle alignment

The low cross-talk for both GIF625 and F-MCB-T tissue bundles (see Table 3.1) indicates precise bundle-to-bundle imaging. Furthermore, for both fibre types, the detector bundle alignment procedures outlined in the *Methods* section produced optimal alignment of every fibre within the bundles.

3.3.3 Fluorescence collection characteristics of the optrode

We characterised the depth over which fluorescence was collected in a single optrode fibre, with the optrode placed in a rhodamine solution, in order to ascertain whether an optrode fibre would integrate fluorescence from a similar volume as a flat-cleaved fibre. The protocol used is shown schematically in Fig. 3.4A. Both the flat-cleaved fibre and the optrode were mounted on micromanipulators, and the fluorescence signal level detected through the fibres was recorded as they were moved away from either the base or side (Fig. 3.4A) of a cuvette. Recordings were used to reconstruct the graph of Fig. 3.4B. The graph indicates that an optrode fibre may integrate fluorescence from a similar volume as its flat-cleaved counterpart, despite the curved surfaces in the optical pathway of the optrode. The characteristics of both optrode and flat-cleaved fibre were predicted reasonably by the theoretical model of Zhu and Yappert (1992) (see Fig. 3.4B).

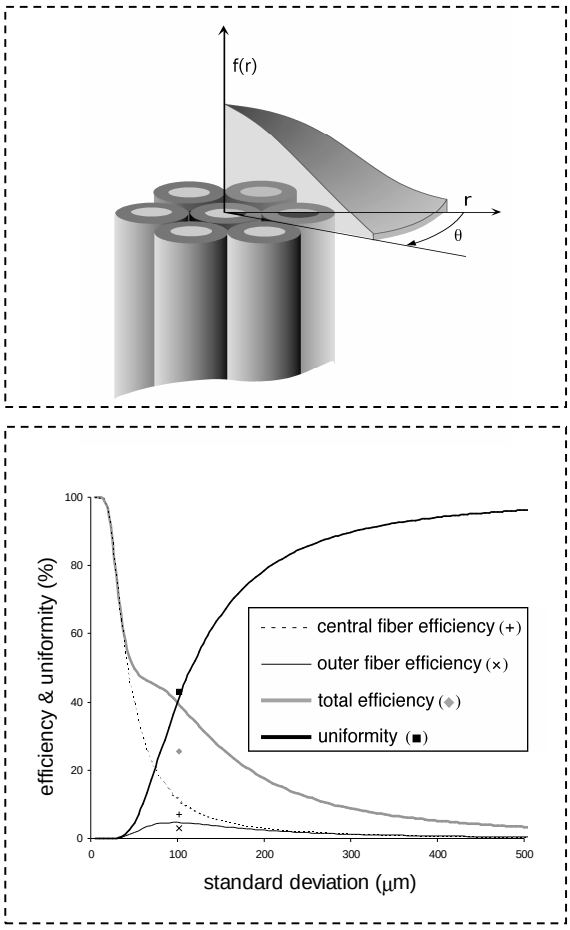

Figure 3.3 *Coupling the laser beam into the tissue fibre bundle*

(A) The Gaussian distribution of laser beam intensity, superimposed on the tissue fibre bundle. (B) Transmission characteristics for the F-MCB-T fibre bundle. Curves represent the results of numerical integration of the laser beam intensity profile. As the beam SD is increased from 15μm, coupling efficiency to the central fibre diminishes whilst coupling to the outer fibres increases, to peak at a SD of 100μm. Data points show the transmission efficiencies as determined by fibre bundle input and output beam intensity measurements.

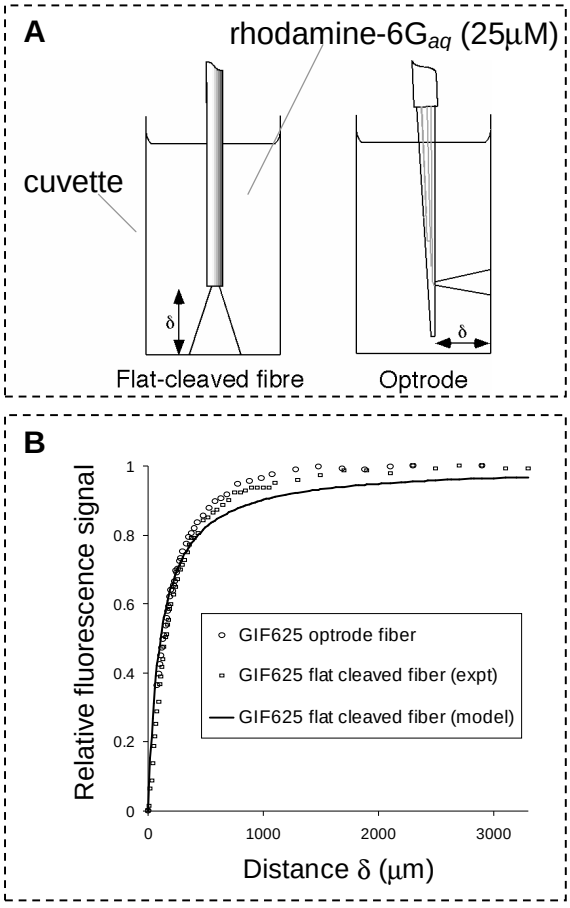

Figure 3.4 *Depth collection characteristics of optrode in rhodamine*

(A) Schematic showing the experiment to determine the depth collection characteristics of a flat-cleaved fibre, and an optrode fibre. Both were immersed in a fluorescing rhodamine solution contained in a cuvette and moved away from the cuvette boundary in a series of steps. (B) Resulting plots of relative fluorescence signal versus depth of fluorescence collection, for GIF625 fibres. The experimental measurements for both flat-cleaved fibre and optrode fibre are shown, along with the theoretically derived curve (solid line) for the flat-cleaved fibre (Zhu and Yappert, 1992).

3.3.4 Directionality of the optrode

The assumption that the F-MCB-T fibre optrode is a unidirectional sensor (ie. fluorescence is collected at each fibre position from one side of the optrode only), was tested. The motivation for this test arose from the observation that as the core:cladding ratio increased in the optrode fibre (compare GIF625 and F-MCB-T fibres), the exiting beam became less directional and "clean". A single 40^o bevelled fibre of type F-MCB-T (Newport Corp.) was held in position by a holder (FPH-CA, Newport Corp.) allowing only rotation about its central axis (Fig. 3.5). A custom made stage allowed the positioning of a second single mode flat-cleaved fibre at any point in an annulus about the bevelled fibre. Firstly the bevelled fibre delivered light which was sampled in space by the flat-cleaved fibre. The flat-cleaved fibre was routed to a photodiode, and the detected power recorded at a number of θ and ϕ positions (see Fig. 3.5) to obtain a map of excitation efficiency $I_e(\theta,\phi)$ of the optrode fibre. Subsequently the coupling was reversed such that the flat-cleaved fibre delivered light which was sampled with the bevelled fibre, generating the complementary map of collection efficiency $I_c(\theta,\phi)$. The normalised fields were multiplied together to obtain an illustration of the relative spatial fluorescence collection efficiency of the optrode fibre. The maps of $I_e(\theta,\phi)$, $I_c(\theta,\phi)$, and $I_e{*}I_c(\theta,\phi)$ are shown in Fig. 3.6A, B, and C respectively. It can be seen in this figure that the bevelled fibre demonstrated more directionality in excitation than in collection. Fig. 3.6C indicates, however, that the optrode fibre is indeed a unidirectional sensor. It is likely that in generation of the excitation map, coupling of the laser to the multimode fibre only excited low order modes of the fibre, leading to a more directional field than in the collection case. To test this prediction a mode scrambler would need to be added within the length of the multimode fibre, and the fields reconstructed.

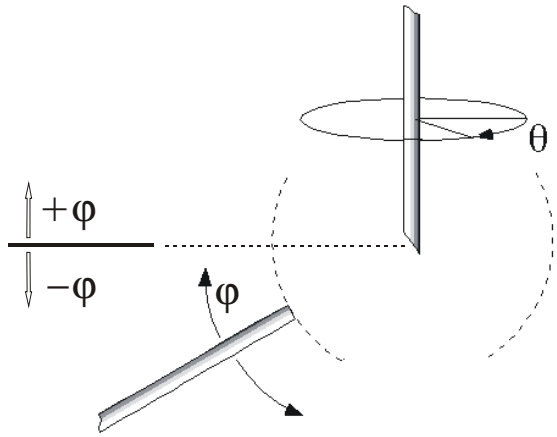

Figure 3.5 *Optrode directionality characterisation*

Schematic of the set-up used to characterise the optrode fibre directionality of recording. The bevelled fibre is free to rotate about its central axis. A second flat-cleaved fibre can be rotated about the bevelled fibre whilst always pointing toward its end. Each fibre is used alternately to deliver and collect light (see text for details).

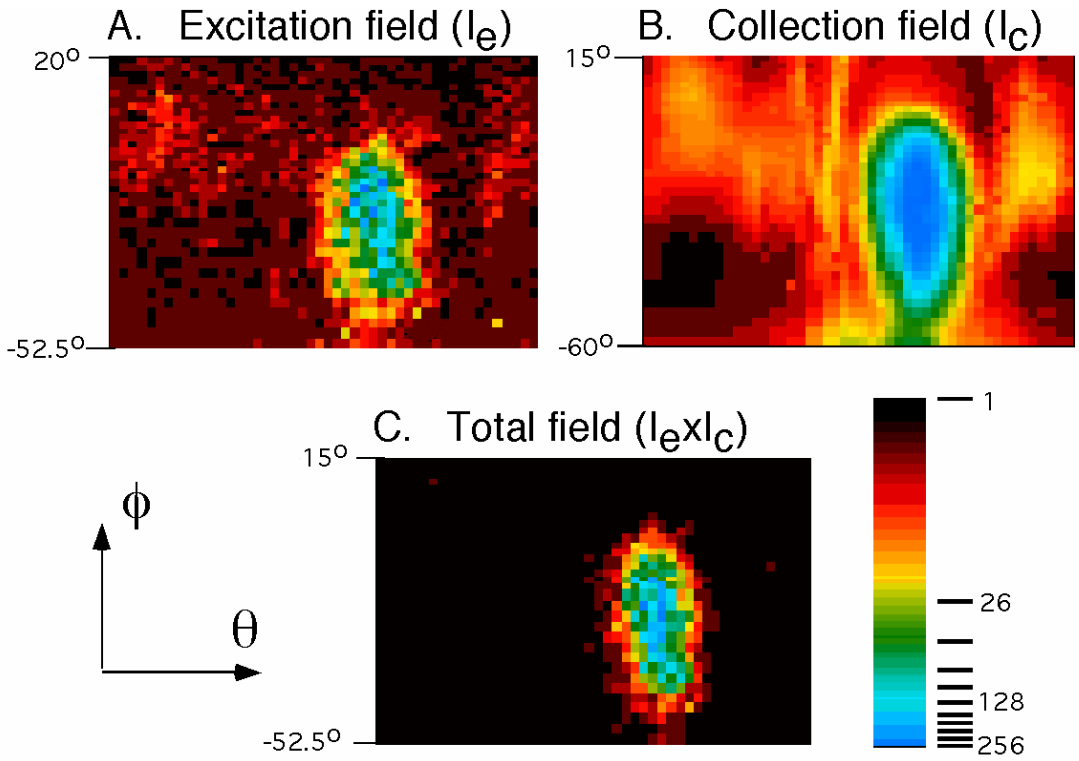

Figure 3.6 *Bevelled fibre fluorescence collection directionality*

(A) Map of excitation efficiency of the bevelled fibre obtained by using the bevelled fibre for illumination and the flat-cleaved fibre for detection. (B) Map of collection efficiency of the bevelled fibre obtained by reversing the coupling used in A. (C) Map of the product of excitation and collection efficiencies, illustrating the spatial variation of fluorescence collection efficiency of the optrode fibre. Note the use of a logarithmic colour scale for all images.

3.3.5 System noise

System noise was characterised by varying the fraction of laser power delivered by a single fibre to a fluorescent solution. Signal level was the total fluorescence detected, and the RMS noise on this signal was determined. In Fig. 3.7, RMS noise is plotted as a function of the mean signal level. The dark noise of the system (RMS noise at zero signal

level) was 0.004mV. The system noise was characteristic of shot noise ($noise_{RMS} \propto \sqrt{signal}$) over a small range, before being determined by the laser noise ($noise_{RMS} \propto signal$). The fitted line for a laser noise limited system in Fig. 3.7 indicates RMS laser noise of 0.27% of the signal level. The operating points of the system when using 10mW excitation power delivered to the stained heart preparations are shown by white and grey arrows for the 520-600nm and >600nm wavelength detectors, respectively. The illumination power of 10mW is similar to that used in the laser scanning optical mapping system of Knisley and Baynham (1997).

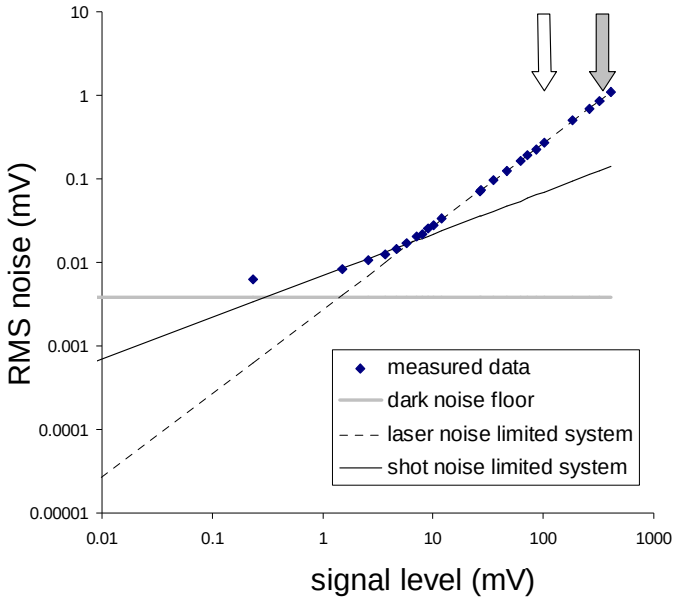

Figure 3.7 *Noise characteristics of the system*

Examination of the RMS noise to mean signal level relationship for the optical system (note log-log scale). At high signal levels the system noise becomes dominated by laser noise, and increasing the excitation power to the tissue does little to enhance SNR further. The operating points for 10mW excitation power in stained heart tissue are shown by the arrows (white arrow for the 520-600nm detectors, and grey arrow for the >600nm detectors).

3.3.6 Animal experiments

In all rabbit hearts tested, high fidelity membrane potential dependent signals were recorded. Typical raw signals obtained with a combination of both ratiometry and 2,3-BDM (15mM) are shown in Fig. 3.8A. Their beat averaged counterparts are shown in Fig. 3.8B, along with the cardiac electrogram. Time of depolarisation was measured in the optical signals by the time at dV/dt_{max}, and always lay within the activation complex of the cardiac electrogram. For the recording shown in Fig. 3.8 activation times had a

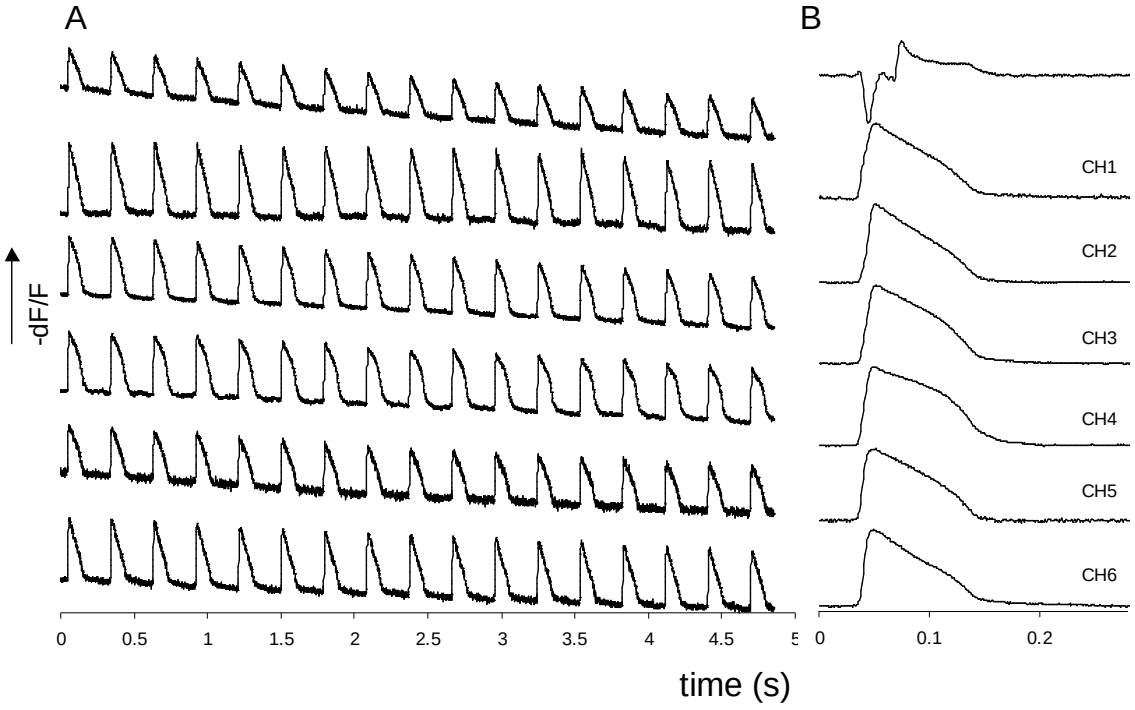

Figure 3.8 *Membrane potential–dependent signals*
(A) Raw membrane potential dependent signals obtained with both ratiometry and 2,3-BDM (15mM). Baseline drift of the signals is on average 78% of the upstroke amplitude over this 5sec recording. (B) Upper trace: beat averaged (16 beats) cardiac electrogram recorded close to the optrode. Lower six traces: Beat averaged (16 beats) optical signals. Average signal to noise ratios are 42 and 165 for optical signals in (A) and (B) respectively.

spread of 6ms (mean spread was 7.2ms across all three experiments). Action potential upstroke durations as measured by the time required for the upstroke to change from 10% to 90% of its maximum amplitude were 9.03±1.54ms (mean±SD) for Fig. 3.8 recordings, and 5.82±2.75ms (mean±SD; range 1.9ms to 11.52ms) over all recordings from the three experiments. Typically upstrokes were fastest in the early stages of an experiment (data

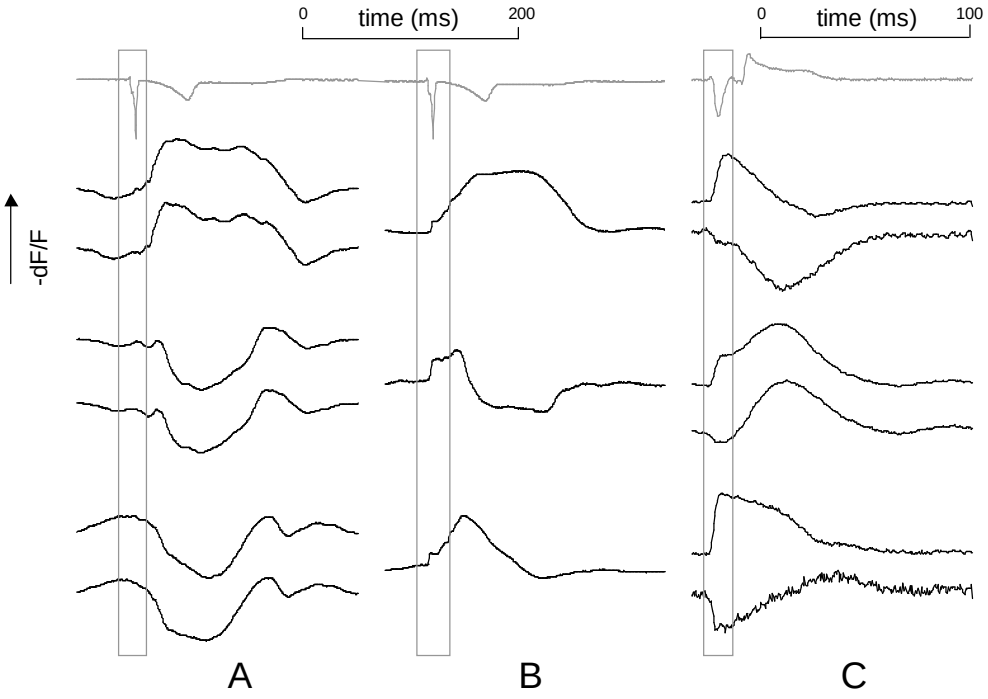

Figure 3.9 *Effects of 2,3-BDM on the signals*

All traces represent beat averaged data (16-20 beats). The uppermost (grey) traces are cardiac electrograms. (A) Lower traces: pairs of optical signals (>600nm (top) and 520-600nm (bottom)) from three optrode recording sites without the addition of 2,3-BDM to the heart. (B) Ratioed signals from (A), showing a clear action potential upstroke followed by substantial motion artifact. (C) pairs of optical signals from three recording sites with 2,3-BDM. Average signal to noise ratios are 47 and 7 for wavelengths >600nm and 520-600nm respectively. See Figure 3.8B (CH3-5) for the ratioed signals from (C).

not shown). Baseline drift in the ratioed signals was 0.4±0.47% per second of recording (mean±SD), whilst the action potential upstroke constituted 1.86±0.88% of the ratio (mean±SD) over all experiments. For the analysed experiments the central fibre of the optrode was not used in recording.

Where 2,3-BDM was not added to the perfusate, the non-ratioed voltage-dependent signals were lost within large motion-related signal fluctuations (Fig. 3.9A). The ratioing of these signals yielded visible action-potential upstrokes which could be identified by their fast rate of rise, and their timing relative to the cardiac electrogram. However, the signals still contained large motion artifacts (Fig. 3.9B). Where 2,3-BDM was added to

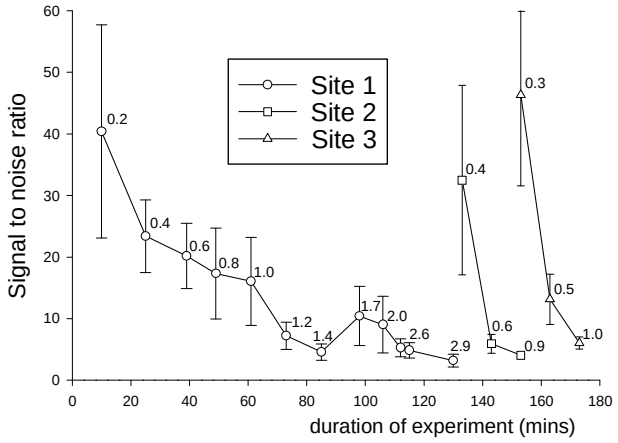

Figure 3.10 *Decay of signal quality with time.*

Plot of SNR against total duration of the experiment. Data represents the mean and standard deviation SNR across all six optrode recording channels. The cumulative laser exposure time (mins) following each recording is shown alongside each data point. Three optrode placements (Sites 1, 2 and 3) were made during the course of the experiment. Total laser exposure of the tissue was 2.9, 0.9, and 1 minutes at the respective sites. The heart was first stained with di-4-ANEPPS at time zero, then restained at t=90mins with the optrode left inserted in its first position.

the perfusate, the non-ratioed signals again contained visible motion artifact (Fig. 3.9C). Ratioing these signals (see Fig. 3.8A) appeared to eliminate motion artifact completely, and reduced the level of noise which was common to all channels, by rejection of the fluctuations in laser power.

The time dependency of signal quality was examined in a single heart, and is summarised in Fig. 3.10. Recordings were made from a single optrode which was inserted at three different sites during the course of the experiment. SNR was calculated as the ratio of action potential amplitude to the RMS noise between action potentials. SNR is plotted against the duration of the experiment, noting the cumulative laser exposure time following each recording. At each optrode insertion site there is a decay in signal quality, this decay being most gradual for the first site.

3.4 Discussion

We have shown that it is possible to record high-fidelity membrane potential dependent signals from multiple sites within the heart wall using a fibre-optic based recording system. To obtain reliable signals, uncontaminated by motion-related artifact and light source noise, it was necessary to employ a combined approach using both ratiometry and the electro-mechanical decoupling agent 2,3-BDM. Neither approach by itself eliminated motion artifact completely, due to the large degree of movement in the preparation, and the relatively small collection volume of the optical fibres. Ratiometry typically improved SNR ten fold by rejecting light source noise. The signals obtained by this method have slow baseline drifts of magnitude similar to those reported by Knisley et al. (2000), and signal to noise ratios rivalling those of spatially averaged CCD video recordings of membrane potential from the heart surface (Baxter et al., 1997). Action potentials measured with the optrode typically had upstroke durations which were comparable to those obtained with photodiode array based surface optical mapping systems operated at low magnification (surface pixel area of $0.3mm^2$) (Girouard et al., 1996).

In order to assess the robustness of the recording technique, signal quality was monitored over the course of an experiment. Signals could be recorded for at least an hour at the initial site of optrode insertion. Gradual deterioration of signal quality was observed, which could be attributed to either laser light induced bleaching of the voltage-sensitive dye, or cell death around the optrode, or some combination of these factors.
Experiments indicated that there were only slight differences in the fluorescence collection depths of flat-cleaved fibres and their optrode fibre counterparts, indicating that both types of fibre geometry may integrate fluorescence from a similar volume.

3.4.1 Limitations of the present study and recording technique

There are a number of limitations to this study, related to both the preparations used, and optical mapping in general. The LV wall thickness of the rabbit hearts was 3-4mm, which did not allow the optrode to be inserted perpendicular to the epicardium. Accordingly, it was not possible to estimate the depth of each fibre tip after insertion, so analysis of transmural differences in action potential morphology is not possible from the present data. Application of the optrode to larger heart experiments will allow such a study, as well as the simultaneous introduction of multiple optrodes and/or combinations of optrodes and extracellular plunge electrodes into the LV. Although spreads in activation times amongst the optrode fibres were seen in all cases, use of a single optrode at any one time did not allow the characterisation of a direction of propagation.

Accurate, time-independent calibration of the optical signals in terms of mV changes in membrane potential was not possible as evidenced by the slow drift in baseline of the ratioed signals. The reason for this drift was the faster decrease in green emission of the dye compared with red emission, over time, as shown by Knisley et al., (2000).

The fluorescence depth collection characteristics of an optrode fibre were examined in a dilute solution of rhodamine. To what extent the collection depth is altered in the presence of a scattering and absorbing medium such as myocardium is the focus of future investigation.

3.4.2 Extracellular potential mapping

For many decades multisite recording of extracellular potentials was the only tool available to investigate patterns of electrical propagation at the whole heart level. Reconstruction of cellular propagation from extracellular potentials (ϕ_e) relies on the assignment of fiducial markers, within the extracellular recordings, which correspond to cellular activation and recovery at the recording site. Typically the maximum negative slope (intrinsic deflection) of a unipolar recording of ϕ_e is picked as the time of activation (Spach et al., 1972), and the maximum positive slope as the time of repolarisation (Steinhaus, 1989). Assignment of these markers to activation and repolarisation is based on studies of ideal propagation in uniform domains. Non-ideal conditions that introduce errors in the times assigned by the fiducial markers include changes in the uniformity of activation sequence, propagation through regions of non-uniform coupling resistance and/or non-uniform membrane properties, changes in the shape of action potential depolarisation and repolarisation, and the addition of distant events (Steinhaus, 1989). Under these conditions, errors in estimating repolarisation times, in particular, may be large (Steinhaus, 1989). Attempts have been made to use more of the shape information contained within an extracellular potential recording in order to determine the parameters of cellular propagation more accurately (Di Persio and Barr, 1987; Ganapathy et al., 1985; Spach et al., 1979; Ellis et al., 1996). The disadvantage of these approaches is that they rely on a priori knowledge of tissue parameters such as action potential shape and electrode to tissue distance, together with interstitial and intracellular resistivities. The problem of how best to define cellular events from extracellular recordings remains unresolved. Despite inherent uncertainties, 3D reconstructions of activation have been carried out with extracellular potential recordings, using the intrinsic deflection to mark depolarisation at the recording site. Indirect measures of repolarisation such as maps of refractory period duration have been used in three-dimensional studies of re-entry, where knowledge of both activation and recovery processes is crucial (Chen et al., 1988).

3.4.3 Optical mapping of transmembrane potential on the heart surfaces

Over the last 20 years, transmembrane potentials on the surface of the heart have been imaged directly by use of voltage-sensitive dyes. Accurate maps of repolarisation have been recorded on the heart surfaces (Efimov et al., 1996). In addition, it has been possible to study the electrical effects of defibrillation and pacing. For instance, recent optical mapping studies have demonstrated that inhomogeneities in post-shock transmembrane polarisation may lead to defibrillation failure (Efimov et al., 1998), which occurs as a result of re-entrant propagation about a shock-induced phase singularity. To date, however, transmural heterogeneities in action potential morphology and repolarisation times have not been well characterised. The recent work of Baxter et al. (2001) offers promise of visualisation of phase singularities in a transmural sense, although the trans-illumination technique used suffers limitations with respect to both spatial resolution, and signal quality, particularly in thick ventricular preparations. It has been shown in modelling studies that phase singularities induced by shocks from implantable cardioverter defibrillators (ICDs) may also occur in the mid-myocardium, and as filaments in three dimensions, with orientations dependent on the local tissue architecture (Entcheva et al., 1998). Routine experimental visualisation of such processes in three dimensions would represent a major advance in cardiac electrophysiology.

3.4.4 Optical mapping with fibre optics

Our optical recording system is based around the use of fibre-optics to deliver excitation light to, and collect fluorescence from, the tissue, with the principle aim of extending optical recordings of transmembrane potential to sites within the heart wall. Previous use of fibre-optics in the measurement of cardiac action potentials is documented (Krauthamer et al., 1991; Neunlist et al., 1992; Krauthamer et al., 1994). These investigators used single optical fibres to measure voltage-dependent fluorescence signals on the heart surfaces. Recently, a multisensor acquisition system has been developed where a plague of fibres is placed on the heart surface, allowing *in vivo* recording of surface propagation (Dillon et al., 1998). Whilst such approaches enable the heart to be

placed remotely from the recording apparatus, they also compromise one of the principal benefits of optical mapping, namely the absence of hardware devices contacting the myocardium. The greatest advantage of using fibre optics, is the potential to make intramural optical measurements, and hence move a step closer to three dimensional reconstructions of membrane potential. For such measurements to be made, a robust, implantable, multi-fibre optical probe was required.

Optical mapping with large numbers of optical fibres requires efficient coupling of the exciting light source into the fibre-optics in order to deliver reasonable excitation power to many tissue sites simultaneously. This presents a problem when small diameter fibres are used. Of the optrode fibres compared in this study, the optimal efficiency of the excitation pathway was greatest (26%) for the F-MCB-T[2] fibres. Based on 10mW exciting power at each optrode fibre site with seven fibres per optrode the maximum number of optrodes that could be used with a 5W laser is 18. Similar numbers of plunge electrodes have been used in 3D extracellular mapping studies (Frazier et al., 1988; Arnar et al., 1997). The optical equivalents of these studies will usefully complement the extracellular potential data already available.

In summary, a novel method for obtaining high-fidelity intramural recordings of transmembrane potential has been developed. We intend to use this system to map transmembrane potential directly in three dimensional volumes of myocardium. The benefits include direct assessment of propagation without extrapolation from extracellular potential data, and the ability to carry out studies into the three dimensional effects of defibrillation.

---

[2] Because of its hard polymer cladding, the F-MCB-T fibre is also stronger than the GIF625 fibre.

Chapter 4

Spatial point response function of fibre optic probes determined by two-photon microscopy

(in preparation for *Applied Optics*)

Abstract

The region of space to which light is delivered and/or from which light is collected (spatial point response function or SPRF) by a fibre optic probe has been determined using a new technique based on two photon microscopy. One advantage of the new technique is that it is applicable to probes embedded in biological media, as well as those immersed in liquids. The SPRFs of some conventional fibre probes are determined in a nominally non-absorbing, non-scattering liquid (rhodamine solution) and an absorbing, scattering biological tissue sample (fluorescein stained heart tissue), and the results compared. The SPRF has also been determined for an optrode fibre (see *Chapter 3*) in fluorescein solution.

4.1 Introduction

The use of fibre optic probes to deliver light to, and/or collect light from, a sample under investigation has wide application in many disciplines. In physiology, for example, such probes can be inserted into the heart and used to extract information about action potentials with minimal damage to surrounding tissue (Hooks et al., 2001). The region of the sample to which light is delivered and/or from which light is collected by the probe is called the spatial point response function (SPRF), and is of interest in many applications. The SPRF depends both on the probe design and the optical properties of the sample in which it is embedded. Theory relating the fibre parameters and optical properties of the medium to the SPRF for the case of non-scattering media can be found in Zhu and Yappert (1992). In the same paper, the authors also provide experimental verification of the theory by making measurements on fibre probes immersed in liquid. For fibres embedded in scattering media, a theoretical calculation of the SPRF is much more difficult and, thus far, the SPRF of fibres embedded in such media has been determined only by experiment (Shim et al., 1999). One drawback of the existing experimental methods for determining SPRF is that they are applicable only to probes immersed in gases and liquids. Since, in physiology as well as other fields, probes are embedded in biological (composite) media, and, since the SPRF depends in part on the optical properties of the medium, an experimental method for the determination of the SPRF for probes embedded in biological media is highly desirable. Such a method (the "2P" method), based on two photon microscopy (Pawley, 1995), is the main subject of this chapter.

The organisation of the chapter is as follows. *Section 4.2* gives a brief review of the theory of SPRF, as expounded in Zhu and Yappert (1992). *Section 4.3* gives a description of the 2P method. In *Section 4.4*, the SPRF in non-scattering media of a standard flat-cleaved communications fibre is determined using both the 2P method and the method described in Zhu and Yappert (1992). The results obtained using the two different methods are in good agreement, providing experimental confirmation that the 2P method is valid. In *Section 4.5*, the 2P method is used to determine the SPRF of two types of

fibre probe, when embedded in an absorbing, scattering biological tissue sample (heart tissue). Comparison of the results with those obtained for the non-scattering media allows the effect of scattering on the SPRF to be inferred. Finally, in *Section 4.6* we aim to characterise the SPRF of the optrode described in *Chapter 3*, using the 2P method.

4.2 Theory

The fluorescence signal *dF* collected by an optical fibre from a small volume *dV* is described under the assumption of axial symmetry by (Zhu and Yappert, 1992)

$$dF(x,r) = \eta K I_c(x,r) I_e(x,r) dV \tag{4.1}$$

where η and K are parameters proportional to the fluorescence quantum yield and absorptivity of the fluorochrome respectively, I_c is the collection efficiency of the fibre ($0<I_c\leq 1$), I_e the intensity of the excitation beam, and dV an annular volume given by

$$dV = 2\pi r dr dx \tag{4.2}$$

where r is the distance from the central axis of the fibre. Applying the assumption that $I_c(x,r) = \alpha I_e(x,r)$, where α is a constant, an expression for the fluorescence collected by the fibre which originates within a distance x from the fibre face can be readily formed as

$$F(x) = 2\pi\alpha\eta K f(x) \tag{4.3}$$

where

$$f(x) = \int_0^x \int_0^r I_c(x,r)^2 r dr dx \tag{4.4}$$

The relative fluorescence signal (R_F) collected within the same distance x from the fibre face may then be defined as

$$R_F(x) = \frac{F(x)}{F(\infty)} = \frac{f(x)}{f(\infty)} \quad (4.5)$$

$R_F(x)$ may then be used to characterise the SPRF of the fibre. Specifically, an effective depth of fluorescence collection x_{eff}, defined as the distance from the fibre face at which $R_F = 0.5$ may be used to compare R_F curves.

4.3 The 2P method for determining the SPRF

Two-photon excitation of fluorochromes arises from the simultaneous absorption of two photons that combine their energies to cause a transition to the excited state of a fluorophore. Because 2P absorption requires two photons for each excitation, its rate depends on the square of the intensity of the excitation beam. In a 2P microscope, the focused excitation beam of infrared wavelength has sufficient intensity to excite fluorochromes only in a small region at its focus. Thus 2P microscopy allows spatially resolved excitation of fluorochromes at points within a volume (Pawley, 1995). To assess the SPRF of fibre probes embedded in biological media, novel use of a 2P laser scanning microscope was made. In a 2P laser scanning microscope the point of fluorochrome excitation is scanned rapidly throughout an imaging plane, and the fluorescence at each point detected in synchrony to the scanning by a photomultiplier tube (PMT). Use of such a microscope allowed us to map the collection efficiency $I_c(x,r)$ of an optical fibre by using the microscope optics for excitation, and the fibre for fluorescence collection (Fig. 4.1). In each case the fibre was routed to the microscope PMT for detection. The microscope excitation point spread function indicates the resolution of fluorochrome excitation at each scan position, and was 1.4 x 13.4μm (FWHM; *x* and *z* directions) for the 10x (NA 0.3) objective lens used. The imaging plane of the microscope was adjusted to intersect the centre of the optical fibre by maximising the collected fluorescence signal. Using the 2P technique, the collection efficiency profiles of two different types of flat cleaved fibre were examined in both solution and heart tissue, and used to reconstruct $R_F(x)$. A step index 100μm core fibre (F-MCB-T; Newport Corp.), and a graded index

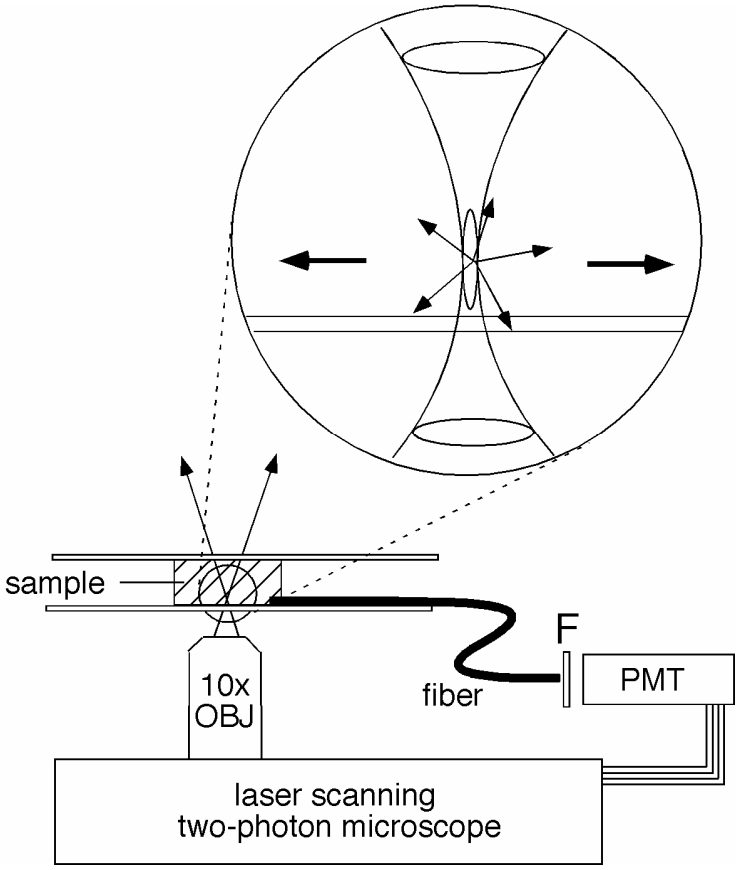

Figure 4.1 *Schematic of the two-photon microscopy set-up*

The microscope objective lens (OBJ) is used to deliver excitation light (750nm) to the sample, and the resulting fluorescence is collected by the optical fibre. The sample is either a solution of fluorescein (1mM), or a block of fluorescein stained heart tissue. The absorption filter (F) reduces direct coupling of the excitation light to the photomultiplier tube (PMT). Inset shows the beam of excitation light and region over which two photon excitation of the fluorochrome occurs. The beam is scanned rapidly in a plane through the sample to generate a map of collection efficiency for the fibre.

62.5μm core fibre (GIF625; Thorlabs Inc.) were used. Each fibre was secured to a glass slide mounted on the microscope stage (Fig. 4.1). Recordings were made first with the fibre bathed in a solution of fluorescein (1mM) to derive the solution SPRF, and then with the fibre inserted into a block of fluorescein (1mM) perfusion stained heart tissue, to derive the tissue SPRF. An overlay of a transmitted light image of an optical fibre inserted into tissue and the corresponding 2P image of collection efficiency acquired immediately after, is shown in Fig. 4.2A, to demonstrate the technique. Scan time for a single 256x256 pixel 2P image was typically 8s, and the image signal to noise ratio was improved by averaging over 128 images. Averaged images were further processed with application of a 3x3 pixel median filter, followed by a threshold to remove the background level. A typical processed image is shown in Fig. 4.2B. The radius *r* was calculated for each pixel as the minimum distance from the pixel to the image axis of symmetry, and used in the discrete summation to obtain *f*(*x*):

$$f(x) = \sum_{0}^{x} \sum_{0}^{256} I_C(x,r)^2 \, r(y) \tag{4.6}$$

The polynomial

$$\delta = a + b/x + c/x^2 + d/x^3 \tag{4.7}$$

was fitted to the *f*(*x*) data using a least-squares linear fit, and the asymptote *a* of the fitted curve used to specify $f(\infty)$. $R_F(x)$ could then be derived from the ratio $f(x)/f(\infty)$. Mean square error of the normalised polynomial fits were of order 10^{-5}.

4.4 Validation of the 2P method

$R_F(x)$ was determined experimentally for a flat-cleaved GIF625 fibre in solution by use of the protocol described in *Section 3.3.3*. (Zhu and Yappert, 1992; Hooks et al., 2001). Briefly, the fibre was used to both deliver excitation light to, and collect the resulting fluorescence from a dilute (25μM) rhodamine solution contained in a cuvette. The fluorescence signal level detected through the fibre was determined as the fibre was

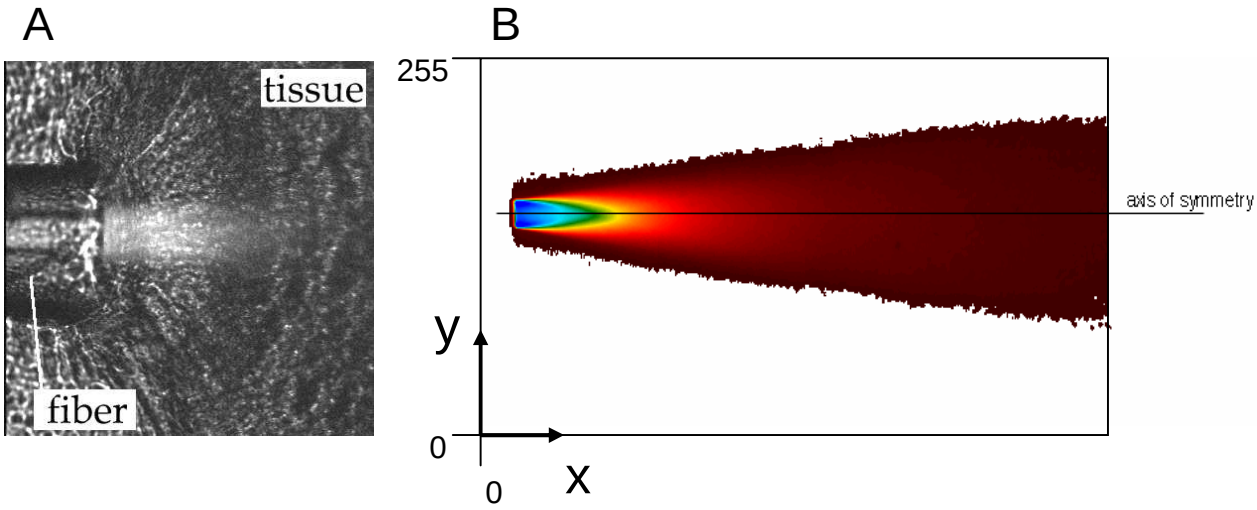

Figure 4.2 *Two-photon image reconstruction*

(A) Overlay of a transmitted light image of an optical fibre inserted into stained heart tissue, and the corresponding map of collection efficiency of the fibre obtained with the 2P microscope. The fibre enters the field of view from the left of the image. (B) Image of the collection efficiency of an F-MCB-T fibre placed in fluorescein (1mM) solution, following averaging, filtering, and thresholding. An axis of symmetry is manually assigned to the image, and the radius of a pixel calculated as the minimum distance from a pixel to this axis..

moved away from the base of the cuvette, in a series of 10μm steps. Data was used to plot $R_F(x)$, and the plot compared to that obtained with the 2P method described above. Both sets of data are graphed in Fig. 4.3A, along with the theoretical model of $R_F(x)$ for this fibre, developed by Zhu and Yappert (1992). Both methods yielded results consistent with the theory, with the 2P method giving the closest description of the model.

For the 2P method to be valid, it is important that the level of fluorescein used to stain the tissue samples does not significantly alter the tissue decay constant for light at the emission wavelengths of fluorescein (peak emission wavelength = 520nm). The staining concentration (1mM) was chosen to obtain 2P images in tissue with a reasonable signal-

to-noise ratio, with the same concentration of fluorescein being used in the solution experiments. The effects of fluorescein concentration on the solution 2P results were tested: a 10 fold dilution to the solution was made, and $R_F(x)$ re-calculated. Fig. 4.3B shows $R_F(x)$ for the two fluorescein concentrations (1mM and 0.1mM). There appears a small shift in the R_F curve to the right following the dilution, indicated by a 10% increase in x_{eff}. The direction of shift in x_{eff} is consistent with a shortening of the decay constant in the concentrated solution.

4.5 SPRF of two fibre types in solution and tissue

The 2P maps of collection efficiency in solution and tissue, for fibre types GIF625 and F-MCB-T are shown in Fig. 4.4. It can be seen in both solution and tissue images that the smaller core diameter fibre (GIF625) has a more rapid decline in collection efficiency than does the larger core fibre (F-MCB-T). Of interest is the slight "flaring" of the GIF625 fibre profile, which presumably is indicative of its graded index construction. The SPRF of both fibres become considerably shortened upon insertion into heart tissue. Plots of $R_F(x)$ for the two flat-cleaved fibres in solution and tissue are shown in Fig. 4.4B. The corresponding values of x_{eff} are tabulated in the legend.

4.6 SPRF of the optrode in solution

The SPRF of an F-MCB-T fibre optrode (see *Chapter 3*) immersed in solution, was also examined. The optrode collection efficiency map is presented in Fig. 4.5A as one longitudinal and three cross-sectional slices. The optrode beam appears to be essentially conical and of similar shape to that of the flat-cleaved F-MCB-T fibre. A volume image (256x256x100 pixels) of collection efficiency was used to determine $R_F(x)$ for the optrode, relaxing the assumption of axial symmetry of the collection field which was used for the flat-cleaved fibre analyses above.

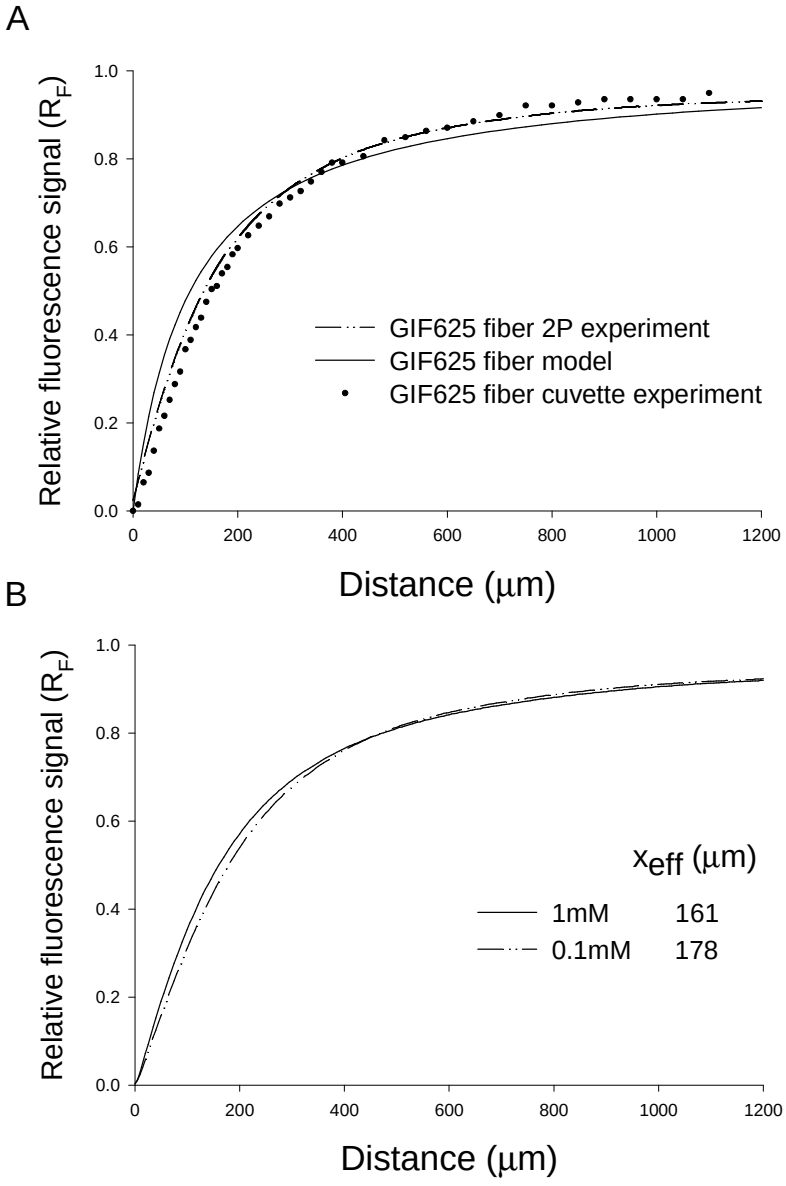

Figure 4.3 *Validation of the two-photon method*.

(A) Comparison of the GIF625 fibre solution collection volume as determined by the cuvette and two-photon protocols, and theoretical analysis. (B) Effect of fluorescein concentration on results obtained for the GIF625 fibre in solution with the two-photon microscope. Values of x_{eff} (distance at which $R_F = 0.5$) are shown in the legend.

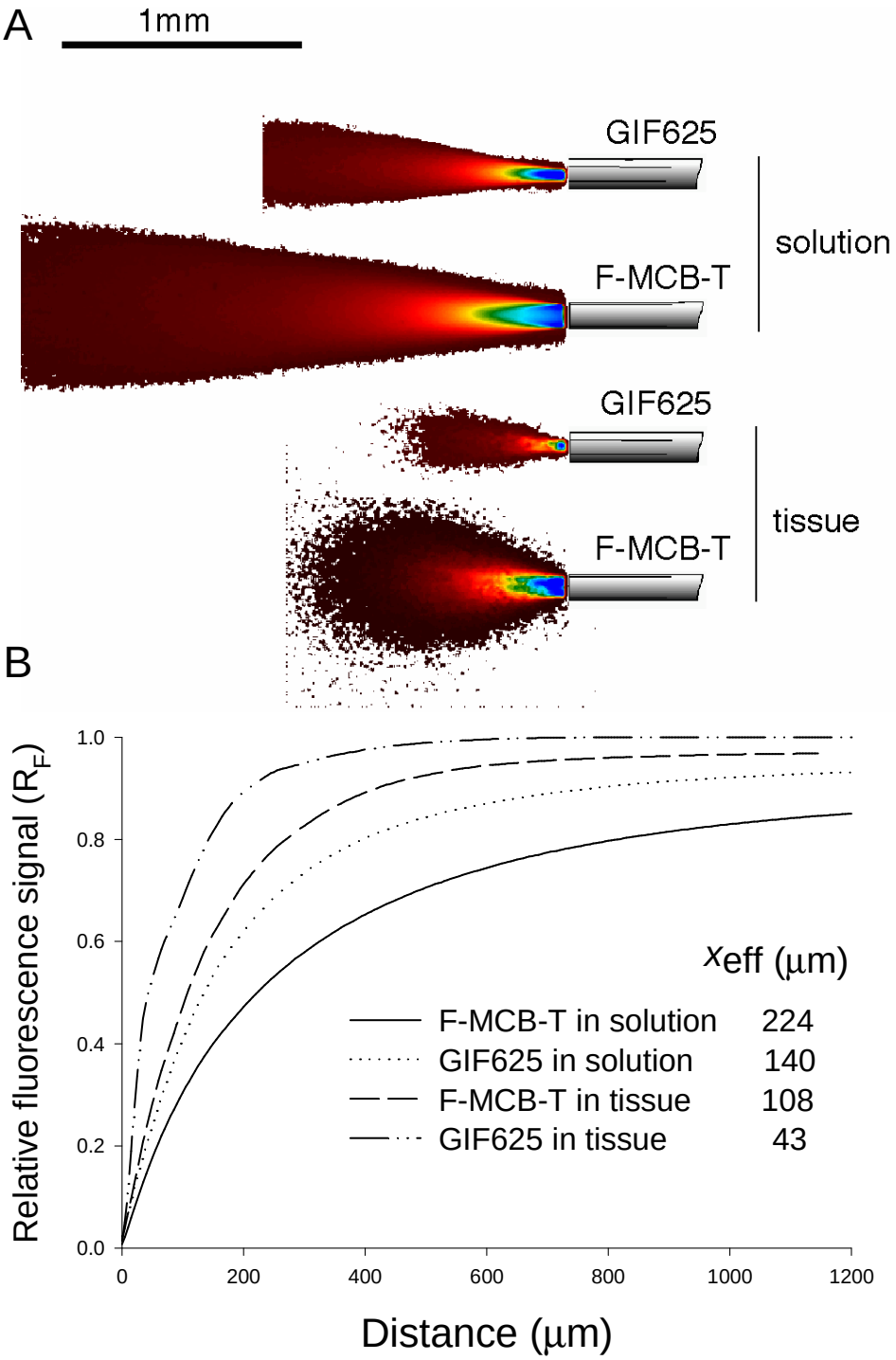

Figure 4.4 *SPRF for two types of fibre in solution and tissue*

(A) Reconstructions of collection efficiency for the two fibre types in solution and tissue. The collection depth of both fibres is reduced in tissue. (B) Plots of relative fluorescence signals versus collection distance from the face of the fibres, derived from the images in (A). Values of x_{eff} (distance at which R_F = 0.5) are shown in the legend.

Figure 4.5B redraws $R_F(x)$ for the flat-cleaved F-MCB-T fibre in solution, alongside $R_F(x)$ for the F-MCB-T optrode fibre, and the $R_F(x)$ theoretical model for the flat-cleaved geometry of this fibre. There is remarkable similarity between all curves. Similar correlation between the SPRF of GIF625 flat-cleaved and optrode fibres was reported in *Chapter 3*.

A tissue collection volume of either optrode fibre could not be directly assessed using the 2P method because the 2P effect could only be produced within a distance limit of ~200μm into the tissue. The optrode device has a diameter of 400μm, and is thus too bulky to position in tissue on the microscope stage. Reconstructions of SPRF in tissue can only be made where the probe geometry allows positioning of the probe fibres close to a microscope slide; this is the major drawback of the method.

Given the high degree of correlation between the SPRF of flat-cleaved and optrode fibres in solution demonstrated here and in *Chapter 3*, one may assume that the optrode SPRF in tissue is also similar to that of its flat-cleaved fibre counterpart.

4.7 Discussion

This study has made novel use of 2P microscopy to reconstruct the SPRF of fibre probes in biological media. The study aimed to characterise the depth of fluorescence collection of various optical fibre probes, and to investigate the effects that a scattering and absorbing biological medium would have on this depth of collection. In the two fibre types examined, the effective depths of collection of the optrode were reduced in tissue by more than one half of their values in solution. There are several limitations to the 2P technique for determining SPRF, and some caution is warranted in interpretation of the results.

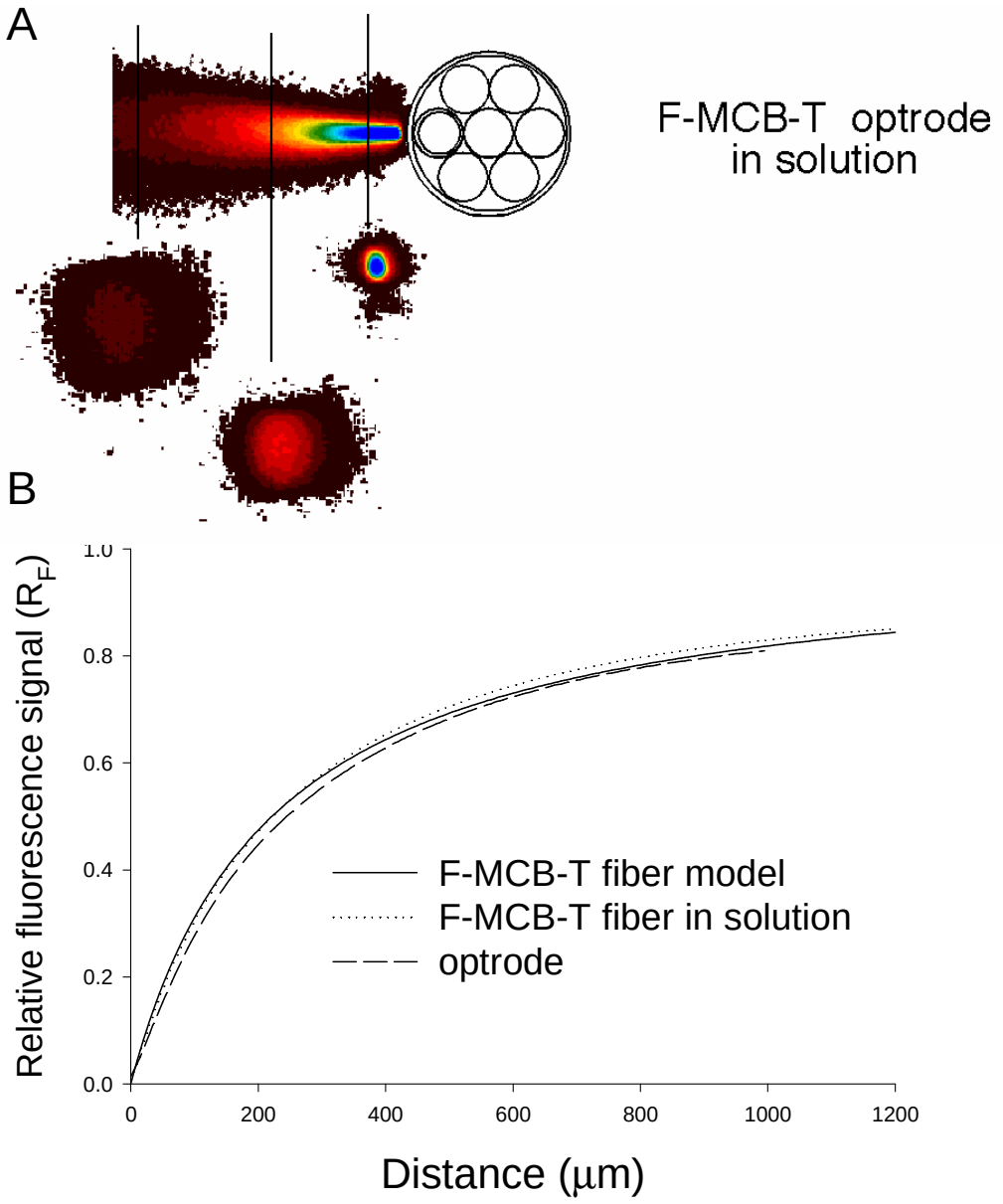

Figure 4.5 *Determination of SPRF for a F-MCB-T fibre optrode*

(A) Reconstruction of collection efficiency for an optrode fibre. A single longitudinal, and three transverse sections are shown through the data volume. (B) Comparison between the F-MCB-T optrode fibre and the F-MCB-T flat-cleaved fibre, along with the theoretical model for the flat-cleaved fibre.

Analysis of the collection efficiency profiles used the assumption that $I_c(x,r) = \alpha I_e(x,r)$. In the context of biological tissue this assumption neglects the effects of wavelength-dependent scattering and absorption as they apply to the different wavelengths of delivery and collection down a fibre based probe. The fluorescein peak emission is at 520nm, and the $R_F(x)$ reconstructions in tissue incorporate the rate of decay of light at this wavelength. For example, 520nm corresponds to the preferred excitation wavelength for the popular voltage-sensitive dye di-4-ANEPPS, however this dye has peak emission at 630nm (Fluhler, 1985). Decay constants for light at 520 and 630nm in heart tissue, which incorporate the effects of both scattering and absorption, have been recently reported as 0.8 and 1.3mm respectively (Baxter et al., 2001). On the basis of these constants we expect the assumption $I_c(x,r) = \alpha I_e(x,r)$ to lead to a small underestimation of the volume of fluorescence collection where di-4-ANNEPS is the fluorochrome. On the other hand, our measurements are expected to be an over-estimate of collection volumes where dyes which are excited at shorter wavelengths are used (for example many of the calcium-sensitive dyes). To obtain a more accurate estimate of the SPRF, one would have to reconstruct two collection efficiency fields, using fluorochromes which had peak emissions at the delivery and collected wavelengths of interest, and then work with the product of these two fields.

There have been previous reports detailing the spatial resolutions of various optical recording devices used in studies of cardiac electrophysiology. The laser scanning system of Knisley et al. (1995) has been shown to have an effective depth of fluorescence collection of ~200μm, whilst Girouard et al. (1996) and Baxter et al. (2001) report effective depths of ~130μm and ~500μm for their photodiode and CCD camera systems respectively. The ability to combine various recording modalities of different spatial resolution in examining the intricacies of cardiac propagation is of fundamental importance. In this study we have shown that fibre-optic based recording systems provide the capacity to combine measurements of different spatial resolution by either the interchange or parallel use of different types of optical fibre. It has also been shown that small diameter optical fibres can offer higher spatial resolutions of recording than present

free space optical systems. Finally, it has been demonstrated that optical fibres may exhibit similar collection volumes whether flat-cleaved or incorporated into an optrode.

Chapter 5

Future Directions

Abstract

The aim of this chapter is to provide a guide for future research which aims to build on the ideas, systems, methods, and results presented earlier in the thesis. The chapter is divided into two main parts. The first deals with future approaches to micro-structurally based modelling of propagation in cardiac tissue, and as such builds on the work described in *Chapter 2*. The second part deals with future developments possible with regard to the optical recording system described in *Chapter 3*, and characterised in *Chapter 4*. The optical recording section of this chapter is the longer of the two parts, and this reflects the considerable work still required to establish a system which can be reliably used to examine phenomena of biological importance. The Bioengineering Group at the University of Auckland has been involved with modelling electrical propagation for over 15 years now. On the other hand, our effort to record optical signals deep within tissue is still in its infancy.

5.1 Microstructurally based propagation modelling

The combination of detailed microstructural data gathered from extended confocal microscopy, and finite element modelling, is an exciting approach to unravelling the mysteries which still surround cardiac function. Although the time taken for computation of any mathematical model is considerable when small scale structure is introduced into the model, the major bottle-neck in this process currently is the time taken to gather the microstructural data. This issue is being addressed by the construction of an automated extended confocal imaging system by the Auckland Bioengineering Group. This rig will consist of 3 integrated modules – a laser scanning confocal microscope, a three-axis translational stage, and a milling machine (Fig. 5.1). With regard to models of propagation, it is hoped that this facility will be able to rapidly provide reconstructions of blocks of human ventricle, which are of equal dimension in each direction. Larger tissue blocks will allow the tracking of most cleavage planes through their entire extent. This will enable investigations of the conditions favourable to re-entry of propagation, as well as the effects of structural alterations implicit in various cardiomyopathies. *Chapter 2* showed that cleavage plane discontinuities play an important role in activation of bulk myocardium during defibrillation, as well as determining rates of propagation from a focal stimulus. Application of the propagation model to a larger volume of reconstructed heart tissue would allow the examination of spiral waves of propagation within the tissue domain. It has been shown that spiral wave stability depends on factors such as ventricular wall thickness (Gray and Jalife, 1998), and domain homogeneity (Mironov et al., 1996). An interesting hypothesis to test is whether cleavage plane discontinuities also predispose a rotating spiral wave to instability. In order to make testing of this hypothesis computationally tractable, it would be necessary to implement an adaptive solution mesh, such that the mesh about the wavefront region was of finer resolution than the mesh elsewhere. Employing multigrid preconditioners for the conjugate gradient solution method also holds promise as a technique to reduce computational time.

With the completion of the automated imaging rig (Fig. 5.1), it will also be feasible to reconstruct volume images of tissue components other than cleavage planes. Components

of interest would include the three-dimensional architecture of Purkinje fibres, or capillaries. Accurate descriptions of components of tissues other than heart such as lung alveoli, will also be tractable. In all cases the functional significance of the structure being imaged can only be deduced by using mathematical modelling. Blood vessel, and alveolar reconstructions might, for example, become critical in designing appropriate lumped-parameter models for the solution of whole organ models. Future limitations to this approach include tissue preparation and staining regimes for the confocal imaging, as well as the large mass of data storage that will be required.

There is an acute need to gain better representations of the three-dimensional geometries of the sinoatrial (SA) and atrioventricular (AV) nodes, to aid the understanding of how these regions of the heart work. There is debate, for instance, over whether earliest activation in the cardiac cycle begins at the centre or periphery of the SA node, and why propagation appears to proceed most rapidly toward the crista terminalis, ahead of activation of the atrial septum (Efimov et al., 1997). Questions such as these readily lend themselves to a microstructurally based modelling based approach.

As the quantity of structural data expands, it will become necessary to develop computer algorithms which can accurately assign three-dimensional geometries to various tissue components. The cleavage plane geometries assigned to the reconstructed rat ventricular volume in *Section 2.2.1,* were manually generated. A larger volume of tissue would necessitate an automated approach. Similarly, building up a three-dimensional reconstruction of a single capillary bed would also be overly labour-intensive to do manually, and suitable vessel tracking algorithms would be needed.

Perhaps the ultimate goal of all cardiac electrophysiology research is to be able to reconstruct electrical propagation at the level of the heart from a set of electrograms recorded non-invasively on the body torso surface. This problem is commonly known as the inverse problem of electrocardiology, and a great number of investigators have been involved in its solution over many decades. One approach to solving the inverse problem is to generate critical points of activation on the epi- and endo- cardial surfaces, and use

these to constrain a continuum model of propagation. The discontinuous behaviour of propagation close to a focal point of activation may in fact lead to significant errors in such a method however, and these need to be investigated in a future study.

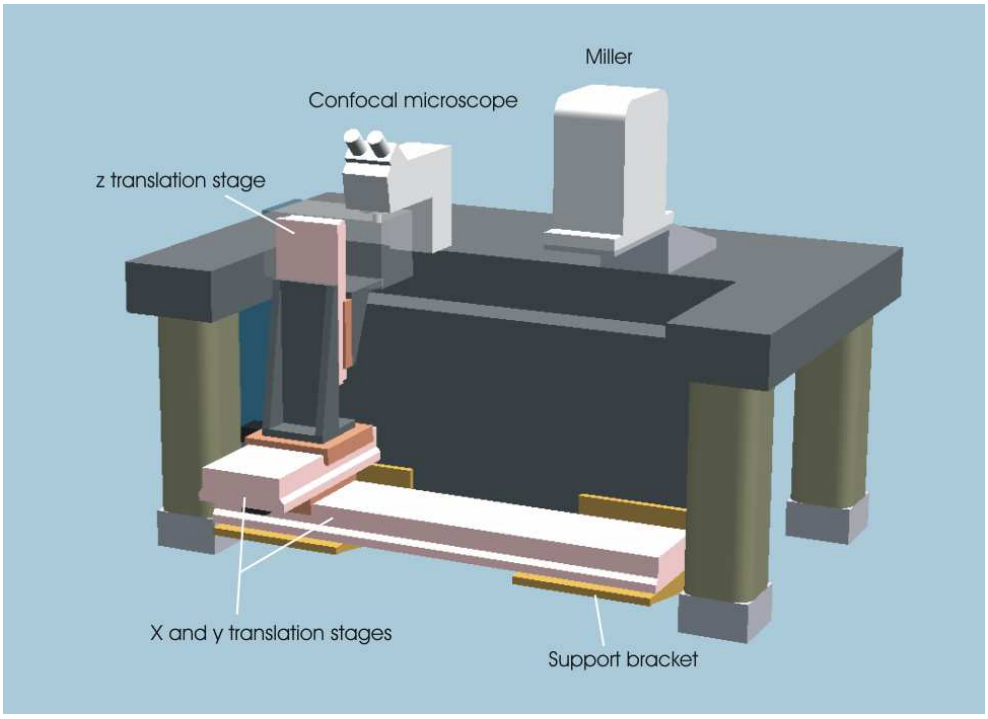

Figure 5.1 *Imaging system schematic*

5.1.1 Validation of the model results of Chapter 2

Three primary observations were possible from the model of electrical propagation described in *Chapter 2*. They were, *1*. that the microstructure of the ventricular wall may be used to define unique electrical properties in three orthogonal axes, *2*. that the initial stages of propagation from a midwall stimulus may be asymmetric about the site of stimulation, and *3*. that the discontinuities associated with the laminar arrangement of myocytes in the ventricular wall may provide the necessary substrate for activation of a sufficient volume of myocardium to terminate arrhythmia by shock application. Preliminary studies in pig hearts (Sands et al., 1999) have begun to provide evidence of

the validity of the first two model observations. It is important that these experiments carried out so far, are progressed further, particularly now that construction of the UNEMAP electrophysiology recording complex (see *Fig. 3.1 part C*) is complete. Briefly, the experiments to date have utilised an array of extracellular plunge electrodes (96 electrodes, mounted on 16 hypodermic needles) to map activation in the left ventricular free wall. Sites of extracellular potential recording are depicted within the myocardial volume in Fig. 5.2. Maps of activation over a volume (14 x 14 x 6mm) of myocardium have been reconstructed, and compared to the microstructure of the tissue within the recording array. Activation maps in the plane of the epicardial surface, at subendocardial, midwall, and subepicardial depths, are shown in Fig. 5.3.

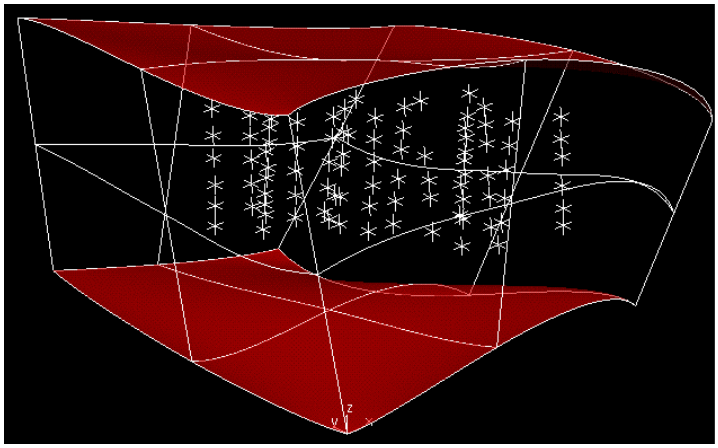

Figure 5.2 *Locations of extracellular electrodes within myocardium*
The positions of the 96 recording electrodes (white crosses) are shown within the tissue volume. Locations are reconstructed by measurement of the plunge needle orientations through the heart wall post-experiment (needles remain in position as the heart is formalin fixed), and interpolation of the recording sites along the needle shaft.

Each map shows propagation from a twice diastolic threshold stimulus located in the centre of the map. Isochrones of activation (defined as the time at which the first

derivative of the extracellular potential signal is most negative) in general form ellipses which are oriented with the local fibre direction at the level of the map (see tissue sections below activation maps, Fig. 5.3). There is marked asymmetry of activation about the stimulus site, as predicted by the model in *Chapter 2*. It is not yet clear, however, whether this asymmetry is merely an artifact of inaccuracies in determining the position of each recording terminal within the tissue. Moreover, the volume of tissue under investigation in the experiments is much larger than that used in the model of *Chapter 2*. It is not certain over what volume the initial asymmetries in propagation, apparent in the model, are likely to average out.

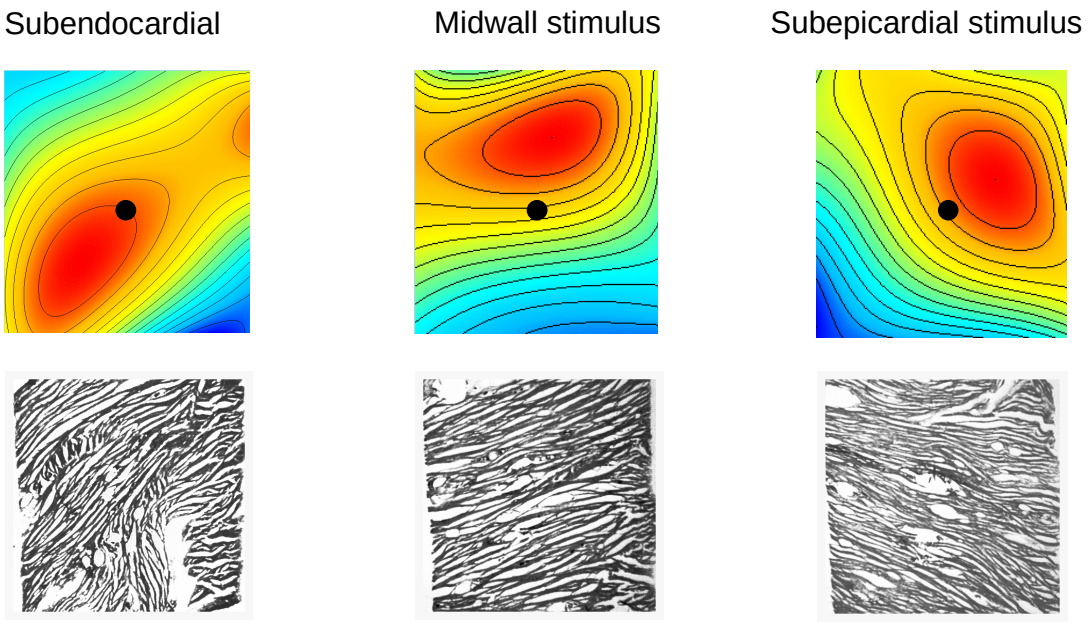

Figure 5.3 *Activation maps following point stimulation*
Activation maps are drawn for the cases of subendocardial, midwall, and subepicardial stimulation. Stimulus sites are shown as black dots. Activation isochrones are aligned with the myofibre structure imaged at the same wall depth as the stimulus site (lower photographs). Isochrone orientations are also markedly asymmetric about the site of stimulation. Tissue images are of frozen 50μm thick sections of myocardium.

In one animal to date, activation maps have been reconstructed in the transmural base-apex plane, and compared to a section of microstructure in this plane. These maps are shown in Fig. 5.4, and again seem to follow the imaged microstructure, indicating that intercellular gaps between adjacent myocyte laminae act to impede propagation normal to these laminae. It should be possible, given signals of better quality than those so far recorded (using an old mapping system), to map activation in three-dimensions, and fit a continuum model of propagation to the map based on measures of structure, and appropriate selection of conductivity parameters. This remains future work. In terms of the extracellular potential signals themselves, data gathered thus far suggests that propagation from a midwall stimulus is indeed discontinuous, and this is reflected in the multiphasic nature of the potential signals (see Fig. 5.5).

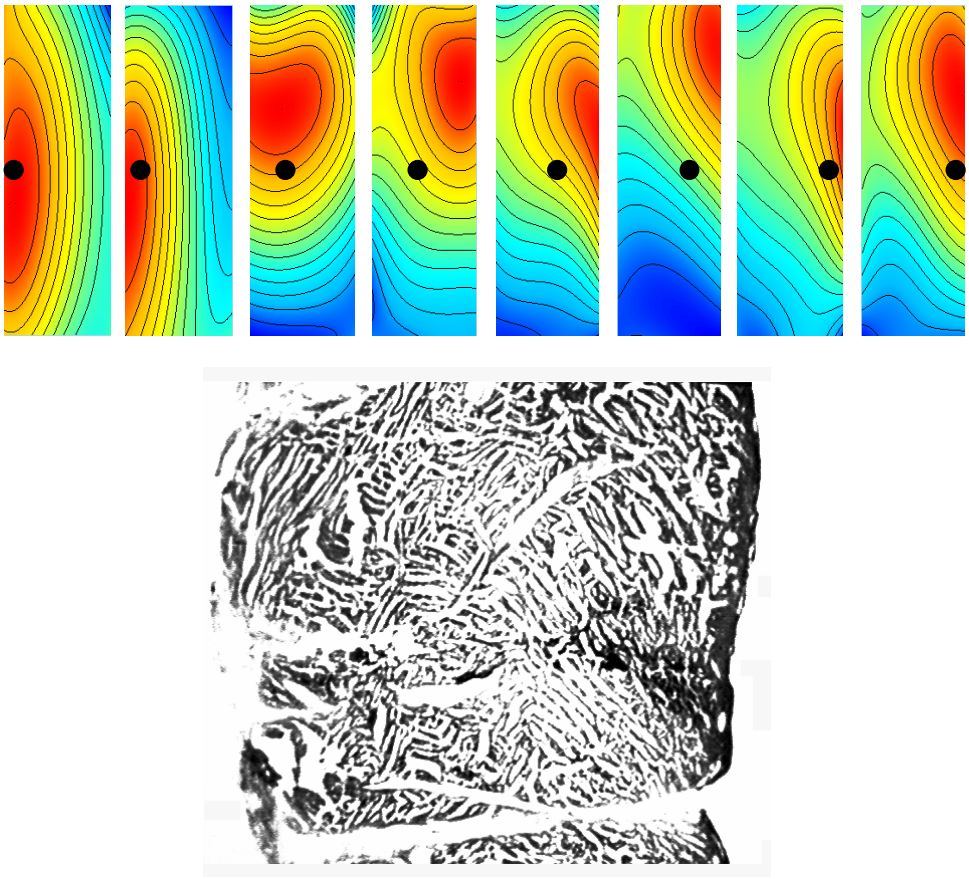

Figure 5.4 *Effect of laminar architecture of myocytes on propagation* Activation maps are plotted on a single transmural base-apex plane for eight different sites of stimulation (black dots). Initial activation appears faster along sheets of myocytes than across these sheets.

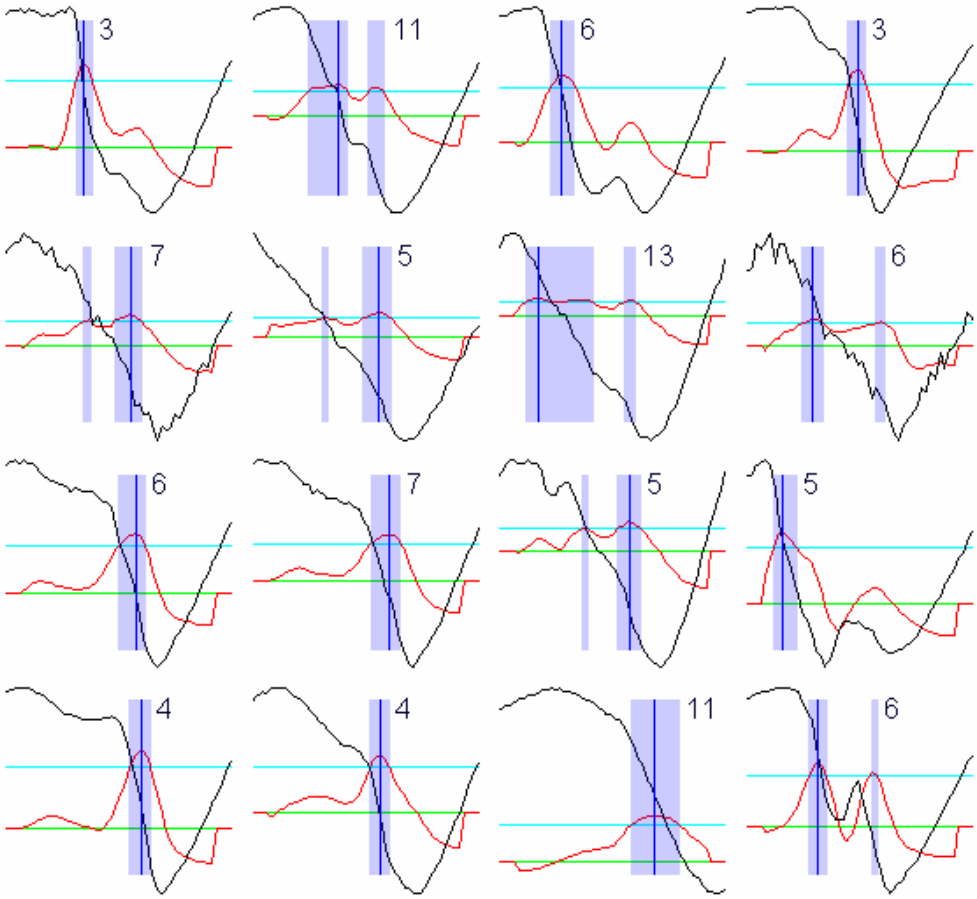

Figure 5.5 *Extracellular potential recordings*

Extracellular potential signals (black traces) from a two-dimensional plane of recording within the ventricular midwall. Stimulation was by current injection at the centre of the array shown. Many traces showed multiphasic activity, indicative of discontinuous propagation. The smoothed negative derivative of the potential recordings is shown in red, whilst the solid vertical bars indicate the time of maximum negative derivative chosen as activation time for a recording site, in order to construct the activation maps of the previous figures. Shaded (blue) regions indicate the duration over which signal derivative is within 90% of its maximum, with the numbers recording this duration in milliseconds.

5.2 Optical Mapping System

This thesis has shown the utility of a fibre-optic based recording system for measuring transmembrane potentials at multiple sites through the heart wall. A foundation has been provided for the development of a full optical mapping system able to measure membrane potentials in three-dimensions, usable for both cardiac and brain research applications.

5.2.1 Beyond the heart - wider applications of a multi-optrode system

5.2.1.1 Electrical activity of the brain:

Whilst the optrode was conceived as a device for the recording of transmembrane potentials at sites deep in the heart wall, it also has clear application in other fields of research. The electrophysiology of neural tissue has been studied with a variety of imaging techniques and with substantial success in understanding the mechanisms of electrophysiological processes. However, a continuing limitation has been the inability to assess action potentials, including the repolarisation of the cell membrane, at multiple sites within the excitable tissue. Previous and current imaging techniques include positron emission tomography, functional magnetic resonance imaging, electroencephalography, magnetoencephalography, and near infrared spectroscopy, each of which offers limited temporal resolution (Shoham et al., 1999). These approaches are sensitive primarily to functional and metabolic processes (Grinvald et al., 1991). Methods that depend on activity related changes in optical properties, such as opacity (Hill and Keynes, 1949) or scattering and birefringence, (Cohen et al., 1968) of neural tissue have also been used to study metabolism. These approaches have allowed, for instance, the investigation of cortical changes resulting from penicillin induced seizures in a rat model (Chen, 2000), the response to stimuli in the auditory complex of cats (Spitzer et al., 2001), long term cortical function in behaving primates (Shtoyerman et al., 2000), the organization of the visual cortex (Bonhoeffer and Grinvald, 1991; Shmuel and Grinvald, 2000), the relationship between functional and neuronal measures in the brains of young adult

humans during visual stimulation (Gratton et al., 2001), and characterisation of language cortices during stimulation in patients (Cannestra et al., 2000; Pouratian et al., 2000).

More recently, electrophysiological investigations in the brain have been aided by recording transmembrane action potentials through the use of voltage sensitive dyes to stain the tissue (Shoham et al., 1999). Voltametric dyes and their associated acquisition and imaging systems have been used to study stimulus evoked excitation in the mouse (Schlosser et al., 1996), cortical dynamics with high temporal and spatial resolution (Shoham et al., 1999), the spread of epileptiform activity in rat neocortex (Sutor et al., 1994), and coherence of activation patterns in the cat visual cortex (Arieli et al., 1995). Because of the inherently two-dimensional nature of optical imaging, deeper structures in the brain are not routinely or easily accessible using this technique. For three-dimensional recordings, it is currently necessary to use extracellular sensors. Traditionally, single unit recordings have been carried out using one or a few manually fabricated microelectrodes in the extracellular space (Vaadia et al., 1986). More recently, an array of fine wires has been developed in order to make many single neuron recordings simultaneously from different depths (Nicolelis, 1997) providing a means for analysing time dependent interactions between cells. Microelectronics techniques have been used to fabricate silicon based electrode arrays that can penetrate the neural tissue (Yoon et al., 2000; van Horne et al., 1990; Campbell et al., 1990; Najafi, 1990) even under chronic conditions (Rousche and Norman, 1998; Hoogerwerf and Wise, 1994). Special fabrication processes can yield true three-dimensional structures (Campbell et al., 1991; Bai et al., 2000)

Significant accomplishments have been achieved in neurophysiology using currently available techniques for recording electrically, using standard two- or three-dimensional electrode arrays, or optically, with intrinsic optical properties or with voltage sensitive dyes. However, there are serious limitations in these approaches. Optical methods are inherently two-dimensional. Although some limited three-dimensional information can be gleaned using confocal microscopy, transillumination (Baxter et al., 2001), or by measuring on two surfaces of isolated preparations, it has until now been impossible to

measure multiple action potentials within the tissue under study. In neurobiology, there is a need to study the relationship between activity in the three-dimensional structures such as the cortex and the retina simultaneously (Nicolelis et al., 1997). A multi-optrode imaging system would provide a new, powerful tool that would lead to new capabilities in this area of investigation.

5.2.1.2 Other fluorescence indicators:

Provided the correct excitation wavelength and appropriate filters are employed, we expect that fluorescence indicators for other variables such as *pH*, *ATP*, and *calcium* could be measured with the optrode. As an example, an interesting study could be the measurement of transmural gradients in *pH* following acute blockage of the left anterior descending artery in the heart. The time course of *pH* change would indicate the gradients of cellular damage across the ventricular wall. Such a study may also provide quantitative means of comparing drugs which aim to re-establish blood perfusion following coronary occlusion, such as thrombolysin. To facilitate use of the wide range of fluorescence probes commercially available, it would be necessary to make a multi-optrode system easy to use in terms of dichroic filter interchange.

5.2.1.3 Blood flow measurements:

The use of laser light to measure blood flow was developed in the late 1970s (Stern, 1975). Since then measurement of blood flow has been made in tissues such as the liver, kidney and brain. The basis of laser based measurement of blood flow relies on the Doppler principle where a moving red blood cell will reflect incident light, and in doing so shift its frequency, in proportion to the velocity of the cell. Laser light allows resolution of capillary blood flow. Light is scattered by red blood cells and the spectral line is broadened by the Doppler effect. Measurement of tissue perfusion at the capillary exchange level is widely used in assessing reperfusion in organ transplantation and in a range of research applications (Bolognese et al., 1993; Lam et al., 1997). However current laser doppler machines use single channel light fibres to record blood flow at only

one site at a time. Although dual channel systems are available their use is limited as each site requires insertion of a separate probe and hence increased tissue damage. (Hennigan et al., 1994). In many situations such as throughout the brain and kidney, blood flow can vary markedly between sites only 2 mm apart (Leonard et al., 2000). These differences can have a profound influence with regard to the hypoxic and metabolic state of the tissue (Leonard et al., In Press). Thus, the ability to assess blood flow at multiple tissue depths simultaneously could be of great benefit in a wide variety of clinical and research applications. The optrode device shares many similarities with laser based methods to record blood flow in that laser light is sent down a fibre to the tissue and the return light detected on a photodiode: the device could be valuable in these applications.

5.2.2 Further system characterisation

Development of a multi-optrode recording system usable for a range of applications will require elegant user interfaces. Moreover, further characterisation of multi-optrode recording will be necessary. Characterisation issues of critical importance in relation to recording transmembrane potentials in the heart and brain include:

1. Testing whether the intramural optical signals closely represent local transmembrane potentials by comparing intramural optical signals with extracellular electrical signals recorded at the same locations, and manipulating action potential amplitudes and durations both by application of electrical fields and by pacing at different rates. It will be possible to assess changes in shock-induced action potentials by comparison with previous results, and to correlate the duration of optical signals with local QT intervals, as well as activation times of optrode signals with those of extracellular potentials.

2. Testing whether multiple optrodes disturb the electrophysiological activity under investigation. The effects of multiple optrodes inserted at varying distances from each other on morphology of action potentials and activation sequence need to be

determined. The effect of the device on extracellular signals recorded with traditional electrodes could be similarly assessed.

3. Demonstrating that an optrode system can be used to record intramural potentials in the presence of defibrillating shocks. This may be achieved by showing that changes in the optical action potential caused by defibrillation strength shocks during the refractory period increase as shock strength increases, and that hyperpolarisation is greater than depolarization (Zhou et al., 1995).

4. Demonstrating feasibility of optical recording of electrical activity in three dimensions in the brain of an experimental animal. This could be done by demonstrating the co-ordinated activity typical of artificially induced seizure activity.

The successful completion of these aims would prove the feasibility of optrode-based three-dimensional measurements of membrane action potentials in heart and brain. Understanding how insertion of optrodes might disturb the electrophysiological activity under investigation (see *Aim 2* above) can be addressed in part by computer modelling of the insertion process. An example is given in Fig. 5.6, where a spiral wave of activation is modelled in a two-dimensional domain, using the Fitz-Hugh Nagumo membrane current model. In *part A* of the figure, the domain is continuous, whereas in *part B*, insertion of an array of optrodes is modelled by incorporation of square holes in the domain (each hole is of diameter 0.1 x the inter-optrode spacing). It is evident in Fig. 5.6 that insertion of the optrodes does not dramatically alter the general sequence of activation under investigation, although there are some differences in wavefront propagation apparent between the continuous and discontinuous models. The value of the optrode in studies of defibrillation needs to be investigated in a similar fashion. It is likely that the discontinuities invoked by optrode insertion introduce a higher degree of artifact during shock application, than during normal propagation processes.

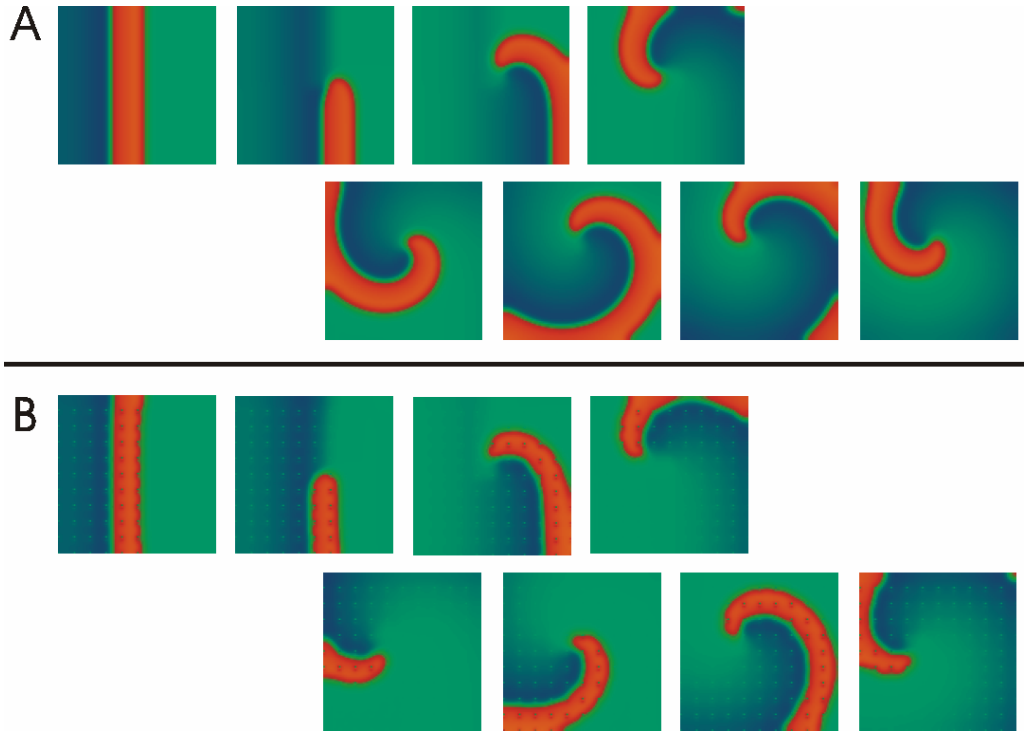

Figure 5.6 *Spiral wave propagation and the effects of optrode insertion*
A two-dimensional monodomain simulation of a rotating spiral wave in (A) a continuous domain, and (B) a discontinuous domain. The discontinuous domain has holes across which zero-flux conditions are applied. The holes are patterned in a regular array, with hole diameter equal to 0.1 x the inter-hole distance. The general pattern of activation is consistent between the two models, although some discrepancies in wavefront curvature are apparent. The spiral wave is induced by extinguishing the upper half of the propagating wavefront (see the second panel of parts A and B). The model used is courtesy of Flavio Fenton (www.http://stardec.ascc.neu.edu/~fenton/java/2dfhnh.html).

5.2.3 Technical issues of a multi-optrode recording system

The specifications for any multi-optrode recording system would need to be stringent. Key issues include minimising cross-talk between channels (preferably to <1%), maximising efficiency of coupling of laser light into the optrode fibres, and maintaining a high signal to *RMS* noise ratio (preferably >60 for recordings during sinus rhythm in the

heart). Satisfying these requirements becomes more challenging as the number of optrodes increases. The strategy for attaining these goals rests on the design of an elegantly engineered module to replace the central (dichroic mirrors, lenses, fibre bundles) portion of the present single optrode system (see Fig. 3.1). Various options have been assessed, and are outlined in detail below.

5.2.3.1 Methods of efficient and uniform coupling of excitation light into optrode fibres:

There are two primary approaches to obtaining a greater efficiency of coupling of the laser light into optrode fibres. One approach is to retain direct illumination of a tightly bundled group of fibres by the laser beam, but enhance the uniformity and efficiency of coupling of this beam into the fibres by changing its cross-sectional intensity profile. The advantage of this approach is its simplicity. System losses will arise primarily due to the illumination of non-core parts of the optrode fibres. A second approach is to devise a means of splitting the laser beam into a number of ‘beamlets’, and then imaging these

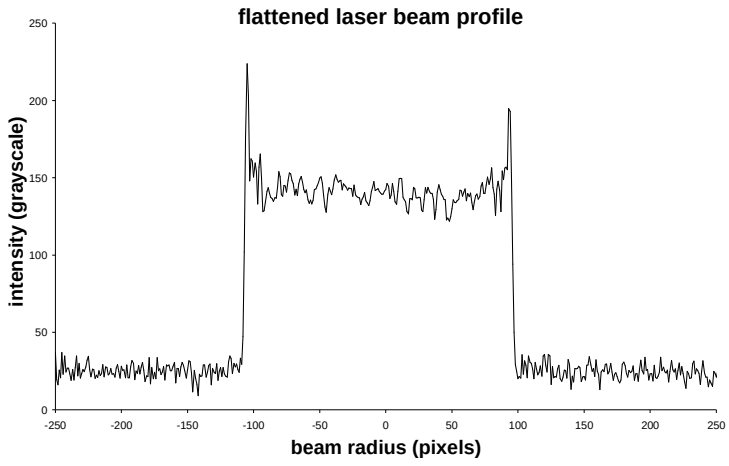

Figure 5.7 *The flattened beam profile*

Profile of the laser beam following propagation through a standard converging lens exhibiting spherical aberration. The spatial noise on the trace is due to the low levels of light that were imaged. Intensity peaks are present on either side of the plateau of the profile, and are consistent with those seen by Al-Saidi (2001).

beamlets into the optrode fibres. The principle losses in a system using this approach are sustained in the beam splitting process. This approach has two main advantages. Firstly, the ends of the optrode fibres proximal to the laser would not need to be bundled together in a tightly packed array. If we are already splitting the laser beam up into multiple beams, there is no reason why these beams need to be in close proximity to each other. A more spread out arrangement of optrode fibres would act to eliminate any cross-talk problems, and may also allow the use of ribbon cable- like structures for bundling fibres. Secondly, coupling of beamlets into the optrode fibres would reduce illumination of the fibre buffer coating, and hence reduce the resulting fluorescence of this coating.

Various experiments were carried out as detailed below to determine the best approach to the beam coupling problem.

Approach 1. Direct illumination of a fibre bundle:

The output beam of a laser operating in TEM_{00} mode has a Gaussian cross-sectional intensity profile. For distributing light evenly to a large number of fibres, a flatter profile would be preferable. Two methods were investigated to achieve so-called “flattened irradiance” (Pu and Zhang, 1998) from the Gaussian laser beam. In the first, light exiting a multimode fibre was imaged onto the tissue fibre bundle. The (light exiting) face of the multimode fibre was brought into focus on the tissue fibre bundle. This technique offered relatively uniform illumination of the tissue fibre bundle, but was found to be untenable due to temporal fluctuations in intensity across the beam width, which were caused by the speckle pattern associated with the multimode fibre. The second method employed the spherical aberration of a standard lens to flatten the Gaussian profile (Pu and Zhang, 1998; Al-Saidi, 2001). The flattened beam obtained by this method was assessed by projection onto a CCD array. The beam profile is plotted in Fig. 5.7. The use of spherical aberration to generate a flattened profile beam holds promise as a useful technique for our application. The advantages of using a beam of flat profile were quantified (Fig. 5.8). The fraction of the laser beam which falls on the fibre cores of the tissue bundle is numerically integrated as in *Section 3.3.1*. Efficiency and uniformity of coupling is examined for a hexagonally packed bundle of F-MCB-T fibres. There are 4 concentric

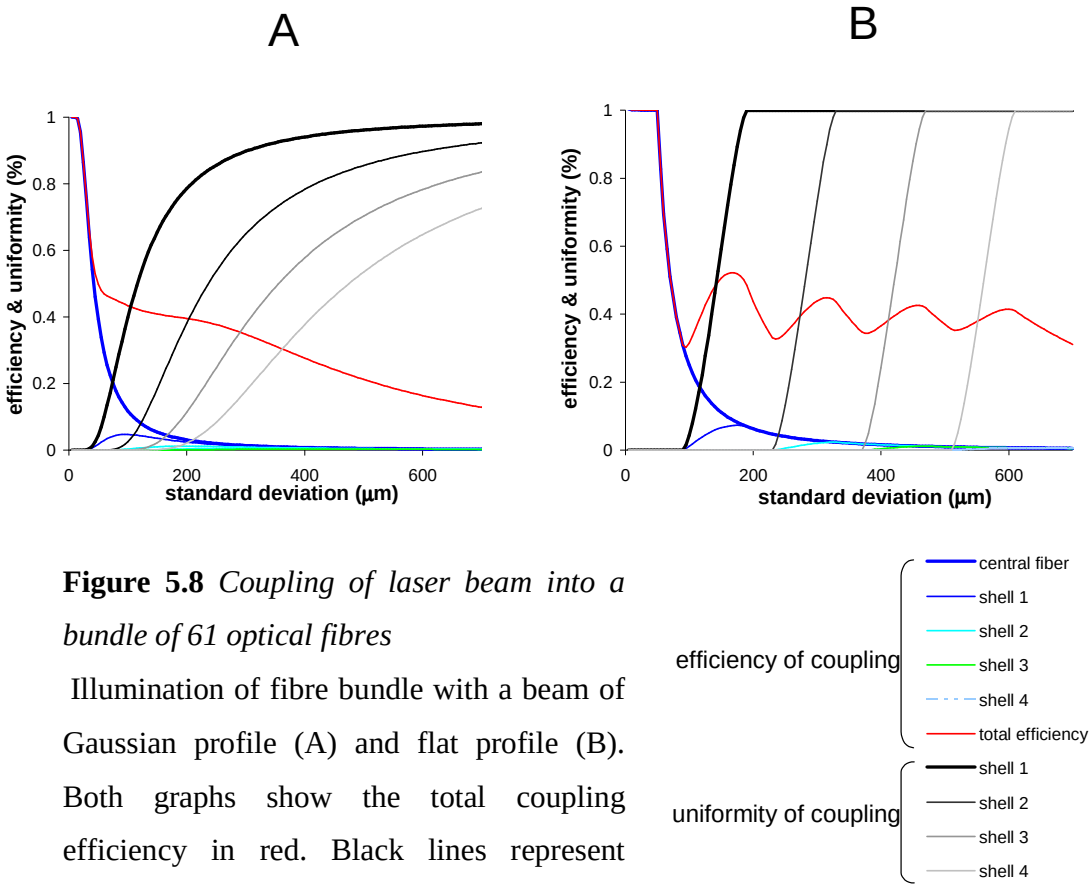

Figure 5.8 *Coupling of laser beam into a bundle of 61 optical fibres*

Illumination of fibre bundle with a beam of Gaussian profile (A) and flat profile (B). Both graphs show the total coupling efficiency in red. Black lines represent coupling uniformity for each of the fibre shells, whilst blue lines represent the efficiency of coupling of light into each shell, and the central fibre of the bundle.

rings or ‘shells’ in the bundle plus a central fibre, giving 61 fibres in total. Efficiency is defined as the percent of total laser power incident to the bundle that may be coupled into any single fibre of a particular fibre shell. Uniformity is defined as the ratio of average power carried by fibres of a particular shell to the power carried by the central fibre. The flattened beam provides both improved coupling efficiency and uniformity for a bundle of 61 fibres. For a flattened beam, total coupling efficiency approaches ~40% as the number of shells in the fibre bundle increases.

Approach 2. Use of beam splitters for distributing light between optrode fibres:

(a) A fibre splitter based approach

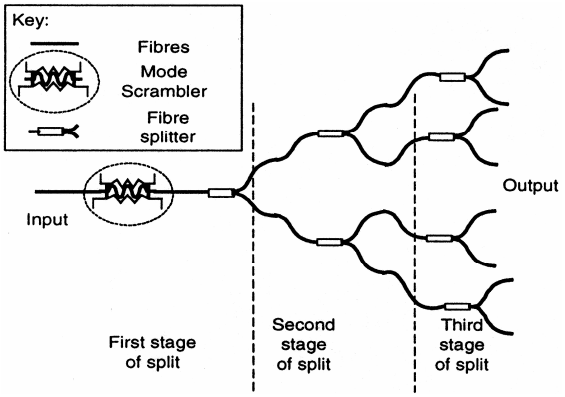

Figure 5.9 *The fibre splitter cascade*

Broad-band fibre splitter configuration. Laser beam is coupled into the input fibre of the splitter in stage one. Three stages of splitters divide the laser light into 8 channels of output.

A light distribution system was designed from broad-band (400-1600nm) fibre splitters (ADC Inc.). The design is shown in Fig. 5.9, and consists of a cascade of fibre splitters. A mode scrambler (FM-1; Newport Corporation) was necessary at the input end of the first splitter to allow even distribution of light across all output fibres. The individual splitter performance is determined by the insertion loss (ratio of the optical power launched at the input port of the coupler to the optical power at either output port) and the uniformity (difference between the highest and lowest insertion loss between both output ports). These two parameters were measured to be ~3.5dB, and ~0.5dB, respectively, for the splitters tested. With a cascade of seven splitters (eight output channels), the total transmission efficiency at 630nm was ~53%. Losses arose from coupling the laser into the input fibre of the first splitting stage, the mode scrambler, and the successive stages of splitting. A suitable model for the total transmission efficiency (*T.E.*) of the system may be written as

$$T.E. = 0.9 \times 0.9 \times 0.87S \qquad (5.1)$$

where values of 0.9 are assigned to the maximum achievable laser coupling efficiency, and maximum efficiency of the mode scrambler, and *S* is the number of splitter stages.

A system using 64 optrode fibres would require 6 stages of splitters, resulting in ~35% transmission efficiency. The output fibres of the splitter cascade may be bundled and imaged onto the optrode fibres. A prototype imaging system allowing this strategy was developed as in Fig. 5.10. On the basis of the high losses inherent in the fibre splitters alone this method offered little promise as a viable solution to the laser-fibre coupling problem.

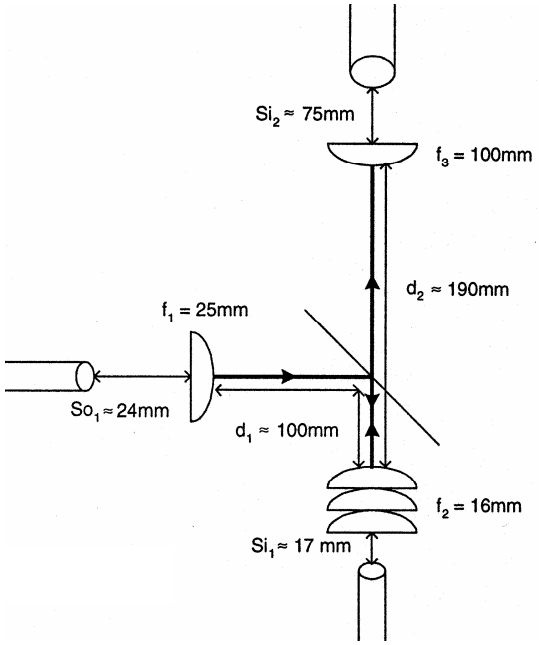

Figure 5.10 *Fibre to fibre imaging system*

The splitter output fibre is imaged via reflection off the dichroic mirror onto the optrode fibre. This is in turn imaged through the dichroic mirror, onto the detector bundle fibre.

(b) A diffractive beam splitter based approach

It is possible to cheaply purchase a linear diffractive beam splitter – a device which is able to split an incident laser beam into 31 beamlets along a single axis, with reportedly 81% efficiency, and 80% uniformity (Thorlabs Inc.). This approach to splitting the laser beam needs to be investigated more fully. It is unclear whether the added efficiency of such an approach would out-weigh the disadvantage that a linear (one-dimensional) array

of fibres is likely to require specially corrected optics to image all fibres without excessive image aberration. Of course the extent of correction required will depend on the number of optrode fibres employed.

5.2.3.2 Systems for detection:

In order to maintain a high SNR on signals recorded with a multi-optrode system, it is necessary to re-evaluate which form of detection is optimal in the optrode application. Before beginning an in-depth comparison of detector types, it is useful, however, to obtain a rough indication of the levels of light we are wishing to detect with the system.

A typical action potential recorded with a single optical fibre placed on the epicardial surface, using a single photodiode as the detector, is shown in Fig. 5.11. The signal was obtained with a flat-cleaved F-MCB-T fibre (see *Section 3.2.3*). Fluorescence was in the >600nm bandwidth (non-ratioed signal). The action potential amplitude is approximately

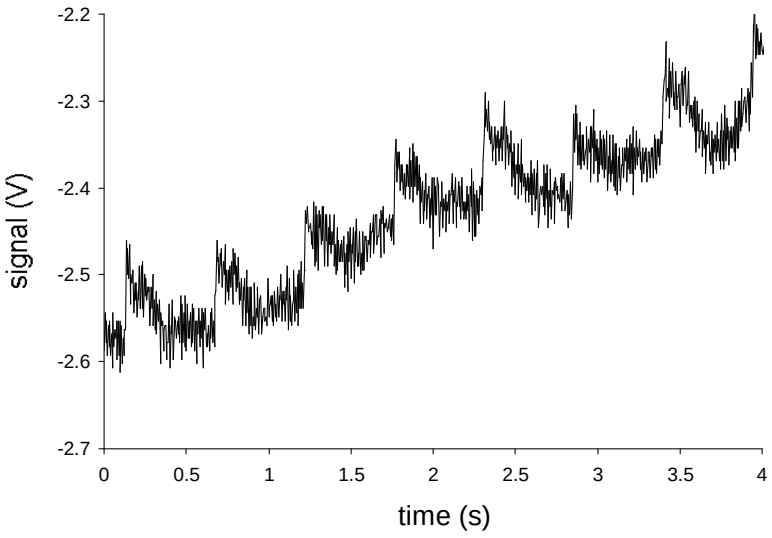

Figure 5.11 *Membrane potential dependent optical signal*
Raw (unfiltered) signal recorded through a flat-cleaved optical fibre placed on the epicardium, using a photodiode. Fluorescence collected is of wavelength >600nm.

0.1V, suggesting a photodiode current of 10nA. Taking (from the manufacturer's specifications) the sensitivity of the photodiode to be 0.4A/W one can easily deduce the photon flux associated with the action potential to be approximately $8x10^9$ photons per second. From Fig. 5.11 we can see that this flux is about 3% of the total background fluorescence. To put this level of light in context, it is suggested that photon counts of $\leq 10^8$/s represent the "low light levels" of fluorescence confocal microscopy (where in fact photon counting may be advantageous), whereas counts $\geq 10^8$/s might be typical of reflectance confocal microscopy (Pawley, 1995). It is not surprising that fibre optics collect more light than the photomultiplier tube of a fluorescence confocal microscope. The increased signal comes at the expense of reduced spatial resolution.

The principle forms of detection presently employed in optical systems used to map fluorescence from tissue surfaces are charge-coupled device (CCD) cameras and photodiode arrays (Baxter et al., 2001; Girouard et al., 1996). The fundamental difference between these two forms of detection is that CCD cameras integrate light (photons) over a period (the frame interval) whereas photodiodes provide a continuous current output in proportion to the light they receive. CCD cameras have many more pixel elements (typically thousands) than photodiode arrays (typically hundreds). If the same area is imaged onto a CCD camera, and a photodiode array, each CCD element will receive far less light than its larger photodiode counterpart, and its SNR will be correspondingly poorer. However the large number of elements permit CCD users the option of averaging over a number of elements (spatial averaging) which can either be done at the readout stage of the camera (pixel binning), or post-hoc by applying averaging kernels to the image.

Detector Overview

Deciding the optimum detector for a particular application depends on an understanding of the parameters governing noise in various detectors. Any photoelectric effect is subject to the Poisson statistics which govern the arrival of photons at the detector, which leads to so called "shot noise" in the recording. Shot noise is simply equal to the square root of

the signal mean for a system which integrates light over time, such as a CCD camera or photomultiplier tube (PMT) in photon-counting mode. For a device which generates current continuously in response to light, such as a photodiode or PMT in continuous measurement mode, the shot noise current is determined from the expression $\sqrt{(2eI_kB)}$, where B is the bandwidth of recording, e the electron charge, and I_k the cathodal current generated in the detector. Quantum efficiency (QE) of the detector in a shot noise limited system is an important parameter. For example, to achieve a SNR of 10 in a light integrating system requires 100 detected photons, which, in a system of QE=0.5 (typical of a CCD camera) requires 200 incident photons. If QE=0.15 however (typical of a PMT) this requires 667 incident photons. Of course shot noise is not the only noise to be considered. PMTs have markedly lower dark noise than CCD cameras, reducing their noise equivalent power to less than the human eye. As light levels increase, PMTs become less attractive because of their poor QE (particularly at red wavelengths). Photodiodes generally have lower dark noise and even higher quantum efficiency (approx. 0.8) than CCD cameras.

The task is to decide on the optimum detector for our application of intramural optical mapping. One of the primary advantages of CCD cameras in heart surface optical mapping is the ability to visualize anatomical structures such as the coronary arteries, in movies of voltage-dependent fluorescence. In our application, spatial sampling density is restricted by the geometry of the optrode itself, and these anatomical features are lost no matter what form of detection is used. The large number of elements in a CCD chip do offer us a different advantage however. This is the ability to image a bundle of many (even hundreds) of tissue fibres, and assign a set of pixels to each tissue fibre. The flexibility in this assignment would allow irregular tissue bundle geometries. For a bundle of tissue fibres to be imaged onto a photodiode array, or onto arrays of fibres leading to individual photodiodes, the tissue bundle must be of strictly regular geometry. This poses fabrication difficulties as the number of tissue fibres increases. The ease of implementing a fibre based imaging system with a CCD camera must ultimately be weighed against the signal qualities of the two detection systems. In a system of low spatial sampling density one must achieve the highest fidelity signals possible, to exclude

artifacts additional to the possible spatial frequency aliasing already inherent to the system.

CCD Cameras

There are currently a very large number of CCD camera types available commercially for a wide range of applications. Camera frame rates vary from the standard 30Hz video rate to in excess of 4kHz. Rapid readouts in the kilohertz range can be obtained in short bursts in specialised cameras, whilst cameras with fewer CCD elements can sustain continuous frame rates up to 1kHz. A popular camera amongst optical mapping researchers at the present time is the Dalsa CA-D1, and the extent of literature which characterises this camera lends it to comparison to our present recording system. This camera offers on-board digitisation of the recorded image, with 12-bit resolution. An important specification for this camera is the read noise (5 digital numbers (DN) *RMS* (max), which corresponds to a noise equivalent exposure of 63pJ/cm^2 (manufacturer's specs)). Assuming a frame rate of 490 frames per second (maximum frame rate), we may derive the noise equivalent power (NEP) as 1.4×10^{-9}W. By cooling, Witkowski et al. (1998(a)) were able to operate the camera with an *RMS* read noise (≡dark noise) of 1.6DN. Their extrapolated conversion constant of 25.7e$^-$/DN (see their Fig. 3B) seems too low for this camera as it corresponds to a full well capacity of 12nJ/cm^2 (assuming a QE of 0.5), far less than manufacturer's specification of 44nJ/cm^2. From Fig. 3B of the Witkowski paper one can estimate the NEP of their cooled system as approximately 10^{-10}W. This is a useful value to compare to our current imaging system. In Section 3.3.5 the dark noise of our photodiode based system was calculated as 0.004mV. Assuming a gain of 10^8 in our current to voltage conversion, and a photo-sensitivity in our detectors of 0.4A/W (manufacturer's specs) we find the NEP of our system is 10^{-13}W. This indicates that our photodiode based system has a threshold for light detection 1000 fold lower than the CA-D1 camera.

Whether the higher sensitivity of our photodiode based system translates into improved recordings of transmembrane potential depends on the magnitude of our signal level

compared to the dark noise. At first glance it may seem that a read noise of 1.6DN is insignificant compared the total 4096DN (12 bits) image representation, however this is not necessarily the case. Following contrast adjustments to allow the entire field of view to be imaged without saturation, it is unusual to obtain a mean action potential upstroke which covers greater than 50DNs in a 12 bit system. It can be seen in Fig. 3 of the Witkowski paper (Witkowski et al., 1998(a)) that at such a signal level the system is not shot noise limited. It is also worthwhile noting that the system of Witkowski et al. (1998) uses pre-camera intensification which adds additional multiplication noise to the system.

We may compare the CA-D1 camera to another camera used in the laboratory of Jalife (Syracuse, New York). Overall, the CA-D1 system has a theoretical limit to the S/N_{RMS} of approximately 10 for each CCD element (Witkowski et al., 1998), which, is not far from the S/N_{RMS} of 7.5 obtained experimentally with Baxter's system (Baxter et al., 2001).

In conclusion we expect that photodiodes may offer greater recording fidelity of transmembrane potentials than their CCD counterparts.

Photodiodes

The operations of a p-n diode can be summarised with the use of Fig. 5.12 (Hamamatsu, 1997). Light incident to the diode generates electron-hole pairs, establishing a current around the short circuited device, which varies linearly with light intensity (note positions at which the operating curves cross the *y* axis in Fig. 5.12. The open circuit photodiode will also produce a voltage response with light which shows less linearity than the current response (see points at which the curves cross the *x* axis). Device linearity is maximised by employing the photodiode in a circuit of low load such as that provided by a high input impedence op amp. Application of a reverse voltage to a photodiode shifts the operating lines to the left in Fig. 5.12, and introduces a dark current which compromises the diode sensitivity. Such a reverse potential leads to improvements in response speed however, by establishing an electric field in the depletion layer of the photodiode which

moves charge carriers more quickly to the diode surface. Thus the principle trade-off in photodiode selection is one of sensitivity and response speed.

PIN photodiodes (region of intrinsic material between the two doped regions) offer very rapid response times, due to their lower terminal capacitance and construction, which reduces the number of carriers generated outside the depletion layer. These devices are primarily aimed at high speed communications applications. The speed required to resolve the events of interest in the heart is considerably less. Avalanche photodiodes (APDs) are similar to PMTs in that they carry on board amplification of the signal. They are suited to applications where the operational amplifier circuit thermal noise dominates the photodiode noise (typical in high speed low light level applications). In this case the amplification of the diode can be increased until its associated noise reaches the same level as the thermal noise of the readout circuit (Pawley, 1995). APDs require driving

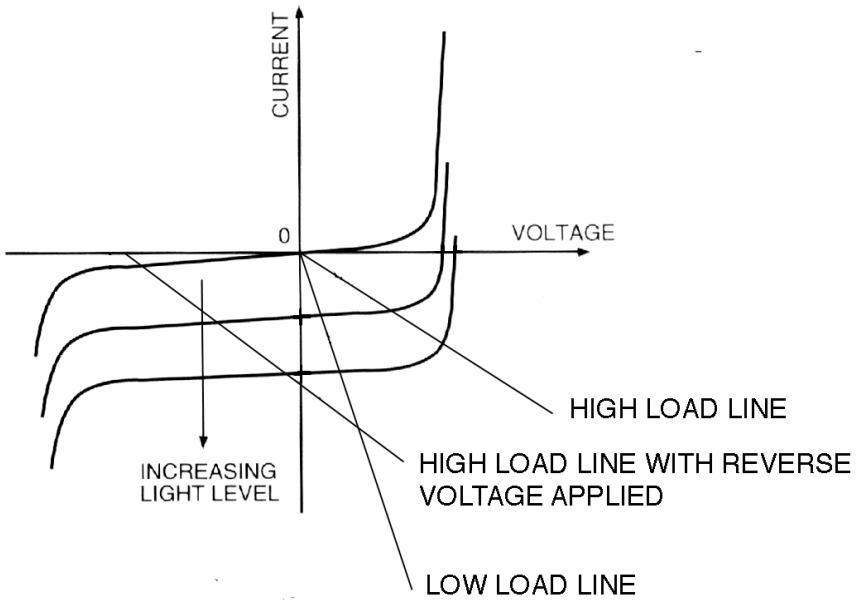

Figure 5.12 *Current versus voltage relationship for photodiodes*
The photodiode operates at points along the y axis when its poles are shorted. Conversely, infinite load between its poles leads to operation at points along the x axis. Intermediate load lines of operation are shown in the figure.

circuits to quench the amplification process, limiting their ease of implementation in multi-element optical mapping systems.

CCD vs Photodiode arrays – a signal comparative study

It is possible to directly compare action potential signals obtained over the same epicardial area, by different sensing modalities. Ideally such a comparison would be between signals obtained in the same hearts, at the same temporal resolutions. Although such data does not exist, some useful comparison is still possible between the signals of different research groups. Fig. 5.13 shows a comparison between photodiode signals obtained with two commercial arrays (C4675; Hamamatsu, Efimov and Biermann, in press), and (MD-144-5T; Centronic, Girouard et al., 1996), and CCD camera signals (6510; Cohu, Baxter et al., 2001), and (ICX 082; Sci-Media Ltd, Gray, 1999). The spatial resolutions (in mm of epicardial surface/pixel) of the signals are shown underneath each trace. Both the high resolution Cohu 6510 signal and the ICX 082 signal are from single CCD elements, whereas the lower resolution Cohu 6510 signal is obtained by application of a conical averaging kernel of width 11 pixels, the effective resolution having been calculated as the product of the spatial resolution of a single pixel and the kernel width at half height (Baxter et al., 2001). Other CCD camera signals from the Witkowski group, using the CA-D1 camera, are of similar quality to those shown (Witkowski et al., 1998(b)). The acquisition rates of the signals shown in Fig. 5.13 are (in order top to bottom) 2000Hz, 1000Hz, 240Hz, and 500Hz. The figure suggests that in terms of both fidelity and acquisition speed CCD cameras perform worse than photodiode arrays. It should be noted that the SNR of CCD camera signals will deteriorate further as frame rates are increased, due to increased contributions of read-out noise (see Fig. 3 of Gray and Banville, *in press*). The light source used in recording may also add noise to the signals. The top three signals were all recorded using 250W tungsten-halogen light sources, whilst the bottom signal was obtained using a 400W xenon arc lamp.

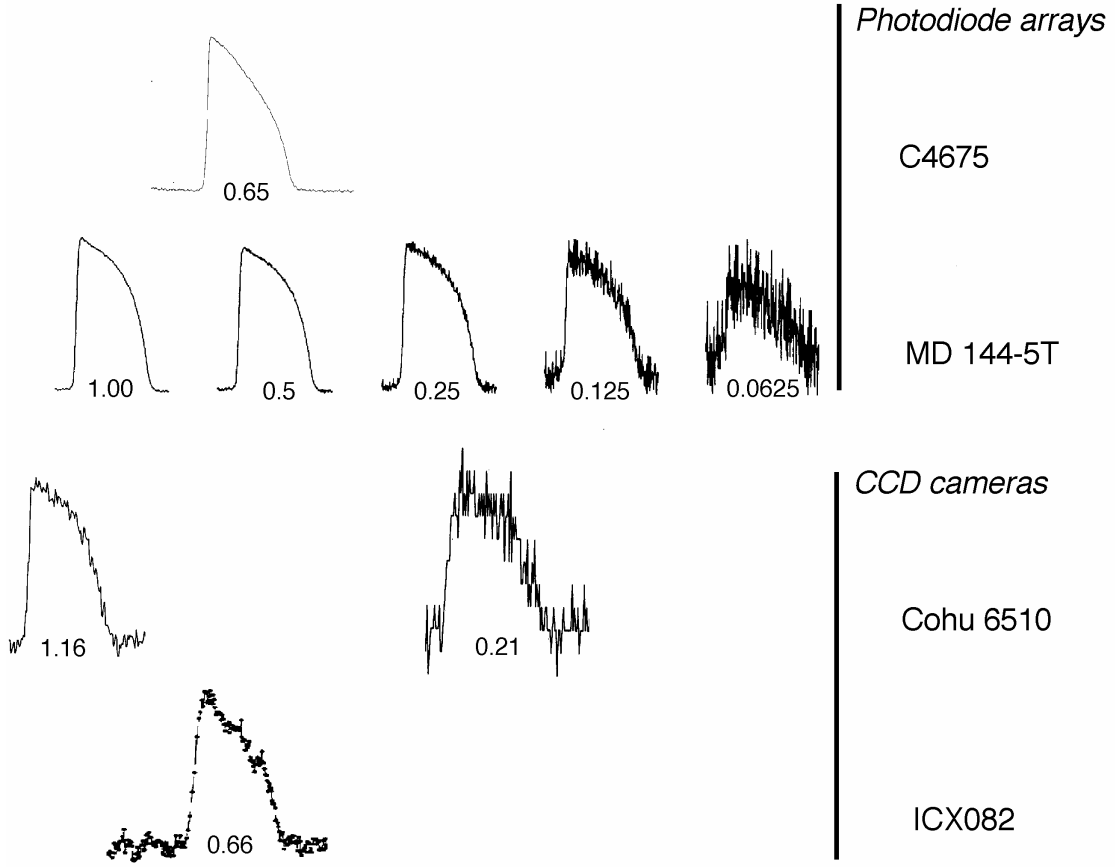

Figure 5.13 *Comparison of optically recorded action potentials*
Signals obtained with photodiodes (top) and CCD cameras (bottom). Spatial resolutions (mm/pixel of the epicardial image) are shown beneath the individual traces.

The discussion above indicates that photodiodes are indeed the most suitable form of detector in our application, assuming the constraints of imaging the optrode fibres onto each detector surface with minimal cross-talk can be overcome.

5.2.3.3 Systems for illumination:

Having discussed the options for detection in the optrode system, it is worth reinforcing the fidelity of non-ratioed signals from our present system is actually limited by noise associated with the laser light source (see *Section 3.3.5*). It is expected that upgrading the

laser presently employed will improve this situation. Options include a new water cooled argon ion laser, or a solid state Verdi laser. The advantage of the latter is an exceptionally stable output beam, however only one line of operation (532nm) is possible with this laser, which would restrict the variety of dyes usable with the system. Perhaps a better approach is to combine the purchase of an argon ion laser with a “noise eating” acousto-optic modulation system: these have the ability to reduce noise in the <1kHz bandwidth by an order of magnitude.

5.3 Conclusions

In summary, this thesis has presented two major bodies of work. In the first, results relevant to the biological function of the heart were obtained, via a novel combination of extended confocal microscopy, and finite element modelling. In the second, a novel probe for making fluorescence measurements deep within tissue was developed and characterised. Both aspects of the thesis promise to open future areas of research and yield further interesting data.

Work is underway to develop an automated extended confocal imaging system capable of producing large-scale reconstructions of tissue microstructure which will be used in functional finite element modelling studies. Segmentation of the tissue components of interest and storage of large volumes of data remain issues to be progressed. Experimental verification of the key aspects of the discontinuous propagation model is continuing.

Several studies are planned which aim to further characterize the optrode system for use in recording action potentials through the ventricular walls. A multi-optrode system with seamless user interfaces is required for the development of a multi-purpose fluorescence imaging system able to be used in a variety of applications.

Appendix

CMISS Command Files

The discontinuous bidomain model described in *Chapter 2* was implemented within the CMISS (**C**ontinuum **M**echanics, **I**mage analysis, **S**ignal processing ad **S**ystem identification) environment which has been developed over some 20 years in the Bioengineering Group. The following file is a list of CMISS commands which are used to solve the model described in *Section 2.2.3* (propagation from a point stimulus).

fem de para;r;minimal_parameters	*Define the parameter sizes for this problem*
fem de regi;r;d_c	*Set up 2 regions; one for the external bounding elements of the trilinear mesh (region 1) and one for the cleavage planes (region 2).*
fem de coor;r;region1 reg 1	*Set up the rectangular cartesian coordinates for*
fem de coor;r;region2 reg 2	*both regions. Both regions are three-dimensional.*
fem de base;r;three_base_combo1	*Define the two basis functions required, namely bilinear (cleavage planes), trilinear (bounding elements of trilinear element mesh).*
fem de node;r;d_c_small_yz	*Define the nodal coordinates of the bounding elements of the trilinear mesh*
fem de elem;r;d_c	*Define the bounding elements*
fem de node;r;manuscript_diag reg 2	*Define the nodal coordinates of the cleavage plane elements*
fem de elem;r;manuscript_diag reg 2	*Define the cleavage plane elements*
fem de fibr;r;d_c_full	*Define the myocyte fibre orientations at the nodes*
fem de elem;r;d_c_full fibre	*Define the interpolation to describe the fibre orientations*
fem de grid;r;d_c	*Define the number of solution nodes within each bounding element, in each direction*
fem update grid geometry	*Update the arrays describing solution node*
fem update grid connectivity	*connectivity*
fem group grid external as boundary	*Group all boundary solution nodes and flag as "boundary points"*
#fem list grid;temp connectivity	*Optional listing of the connectivity of solution nodes (useful for debugging)*

```
#fem export node;d_c_export_full_small_yz as cube
   reg 1

#fem export elem;d_c_export_full_small_yz
   grid_numbers as cube reg 1

#fem export node;cleavage_export_full as
   cleavage_export reg 2

#fem export elem;cleavage_export_full as
   cleavage_export reg 2

fem de equa;r;discontinuous_1 class 1,2

fem de mate;r;discontinuous_1

fem de cell;r;discontinuous_1

fem de init;r;d_c class 1,2

fem de solv;r;discontinuous_1_bidomain calc_activ
   class 1
fem de solv;r;discontinuous_1_bidomain2 class 2

fem solve to 0 calc_activ class 1,2

fem export elem;"gridfield3_full_class1_000" field
   class 1

fem export elem;"gridfield3_full_class2_000" field
   class 2

foreach $count ( '001'..'200' ) {
    my $time = $count/10;
    fem solve restart to "$time" calc_activ class 1,2
    print "time: $time\n";
    fem export elem;"gridfield3_full_class1_$count"
      field class 1
    fem export elem;"gridfield3_full_class2_$count"
      field class 2
   }
```

Export the nodes and elements of regions 1 and 2 in a form readable by the graphics front end CMGUI.

Define the equations to be solved, ie. bidomain and the ionic current model, ie. cubic.

Define the material properties of the domain, namely intra- and extra- cellular conductivities in the three orthogonal directions of the laminar microstructure.

Define the parameters of the cubic ionic model.

Define the initial conditions (nodes of transmembrane current injection).

Define the solver type to use for solving transmembrane and extracellular potentials (ie. conjugate gradient method).

Assemble solution matrices and solve for the initial potentials.

Export the transmembrane (class 1) and extracellular (class 2) potentials at time zero.

Solve the system of equations for 0 to 20ms, in steps of 0.1ms, exporting the potential fields at each time step.

The following file is a list of CMISS commands which are used to solve the model described in *Section 2.2.4* (shock-induced response).

fem define para;r;minimal_parameters	*Define the parameter sizes for this problem*
fem define regi;r;biline	*Set up 2 regions; one for the external bounding elements of the trilinear mesh (region 1) and one for the cleavage planes (region 2).*
fem define coor;r;biline reg 1 fem define coor;r;biline2 reg 2	*Set up the rectangular cartesian coordinates for both regions. Both regions are three-dimensional.*
fem define node;r;confocal_sim_1	*Define the 64 nodes required for the outer bounding elements of the trilinear solution mesh*
fem define base;r;five_base_combo	*Define the five basis functions required, namely bilinear (cleavage planes), trilinear (bounding elements of trilinear element mesh), cubic-linear-linea (sheet angle interpolation), cubic-linear, and linear-cubic.*
fem define elem;r;variable_outer	*Define the bounding elements*
fem define node;r;cleavage_heavy_handed_shifted reg 2	*Define the nodal coordinates of the cleavage plane elements*
fem define elem;r;cleavage_heavy_handed_shifted reg 2	*Define the cleavage plane elements*
fem define fibr;r;full_domain	*Define the myocyte fibre orientations at the nodes*
fem define elem;r;confocal_sim_1 fibre	*Define the interpolation to describe the fibre orientations*
fem define grid;r;confocal_sim_1	*Define the number of solution nodes within each bounding element, in each direction*
fem update grid geometry fem update grid connectivity	*Update the arrays describing solution node connectivity*
fem group elem 1,2,3,4,6,7,8,9 as outer_elements1 fem group elem 10,11,12,13,15,16,17,18 as outer_elements2 fem group elem 19,20,21,22,24,25,26,27 as outer_elements3	*Group the bounding elements for later reference*
fem define equa;r;biline class 1,2	*Define the equations to be solved, ie. bidomain and the ionic current model, ie. modified BR*
fem define mate;r;biline class 1,2	*Define the material properties of the domain, namely intra- and extra- cellular conductivities in the three orthogonal directions of the laminar microstructure.*
fem define cell;r;biline class 1,2	*Define the parameters of the cubic ionic model.*

```
fem group grid xi1=low elem 5 as left_group1_stimulus
fem group grid xi1=high elem 23 as
   right_group1_stimulus
fem group grid xi1=low elem 2,4,6,8 as
   left_group2_stimulus
fem group grid xi1=high elem 20,22,24,26 as
   right_group2_stimulus
fem group grid xi1=low elem 1,3,7,9 as
   left_group3_stimulus
fem group grid xi1=high elem 19,21,25,27 as
   right_group3_stimulus
fem group grid line 1189 xidirn 2 as temp1
fem group grid line 1189 xidirn 3 as temp2
fem group grid line 24301 xidirn -2 as temp3
fem group grid line 24301 xidirn -3 as temp4
fem group grid grid temp1,temp2,temp3,temp4 as
   left_group4_stimulus

fem group grid line 325435 xidirn 2 as temp1
fem group grid line 325435 xidirn 3 as temp2
fem group grid line 371659 xidirn -2 as temp3
fem group grid line 371659 xidirn -3 as temp4
fem group grid grid temp1,temp2,temp3,temp4 as
   right_group4_stimulus

fem group grid line 1189 xidirn -3 as temp1
fem group grid line 1189 xidirn -2 as temp2
fem group grid line 10429 xidirn 2 as temp3
fem group grid line 10429 xidirn -3 as temp4
fem group grid line 24301 xidirn 2 as temp5
fem group grid line 24301 xidirn 3 as temp6
fem group grid line 5269 xidirn 3 as temp7
fem group grid line 5269 xidirn -2 as temp8
fem group grid grid
   temp1,temp2,temp3,temp4,temp5,temp6,temp7,temp8
   as left_group5_stimulus

fem group grid line 325435 xidirn -3 as temp1
fem group grid line 325435 xidirn -2 as temp2
fem group grid line 343915 xidirn 2 as temp3
fem group grid line 343915 xidirn -3 as temp4
fem group grid line 371659 xidirn 2 as temp5
fem group grid line 371659 xidirn 3 as temp6
fem group grid line 333595 xidirn 3 as temp7
fem group grid line 333595 xidirn -2 as temp8
fem group grid grid
   temp1,temp2,temp3,temp4,temp5,temp6,temp7,temp8
   as right_group5_stimulus

fem group grid line 1 xidirn 2 as temp1
fem group grid line 1 xidirn 3 as temp2
fem group grid line 33697 xidirn -2 as temp3
fem group grid line 33697 xidirn -3 as temp4
fem group grid grid temp1,temp2,temp3,temp4 as
   left_group6_stimulus
```

Group together solution nodes at the epicardial and endocardial surfaces in order to specify the time-dependent current boundary conditions at these grouped nodes. Note that uneven node spacing across the epi- and endocardial surfaces requires different current magnitudes to be injected on regions of different node density, in order to maintain a uniform current density boundary condition. This section of the command file was automatically generated by Perl script given the sizes of the bounding elements.

```
fem group grid line 323059 xidirn 2 as temp1
fem group grid line 323059 xidirn 3 as temp2
fem group grid line 390451 xidirn -2 as temp3
fem group grid line 390451 xidirn -3 as temp4
fem group grid grid temp1,temp2,temp3,temp4 as
   right_group6_stimulus

fem group grid line 109 xidirn -2 as temp1
fem group grid line 6757 xidirn 2 as temp2
fem group grid line 29053 xidirn -3 as temp3
fem group grid line 32725 xidirn 3 as temp4
fem group grid line 27973 xidirn 2 as temp5
fem group grid line 6349 xidirn -2 as temp6
fem group grid line 5161 xidirn 3 as temp7
fem group grid line 1081 xidirn -3 as temp8
fem group grid grid
   temp1,temp2,temp3,temp4,temp5,temp6,temp7,temp8
   as left_group7_stimulus

fem group grid line 323275 xidirn -2 as temp1
fem group grid line 336571 xidirn 2 as temp2
fem group grid line 381163 xidirn -3 as temp3
fem group grid line 388507 xidirn 3 as temp4
fem group grid line 379003 xidirn 2 as temp5
fem group grid line 335755 xidirn -2 as temp6
fem group grid line 333379 xidirn 3 as temp7
fem group grid line 325219 xidirn -3 as temp8
fem group grid grid
   temp1,temp2,temp3,temp4,temp5,temp6,temp7,temp8
   as right_group7_stimulus

fem group grid grid 1189,10429,5269,24301 as
   left_group8_stimulus
fem group grid grid 325435,343915,333595,371659 as
   right_group8_stimulus
fem group grid grid
   109,6757,29053,32725,27973,6349,5161,1081 as
   left_group9_stimulus
fem group grid grid
323275,336571,381163,388507,379003,335755,333379,
   325219 as right_group9_stimulus
fem group grid grid 1,28081,33697,6241 as
   left_group10_stimulus
fem group grid grid 323059,379219,390451,335539 as
   right_group10_stimulus

fem define time;r;left_group1_stimulus
fem define time;r;right_group1_stimulus
fem define time;r;left_group2_stimulus
fem define time;r;right_group2_stimulus
fem define time;r;left_group3_stimulus
fem define time;r;right_group3_stimulus
fem define time;r;left_group4_stimulus
fem define time;r;right_group4_stimulus
fem define time;r;left_group5_stimulus
fem define time;r;right_group5_stimulus
```

Define the time-dependent boundary conditions on the various solution node groupings. Each node group contains nodes of equal spacing, on the epi- and endo- cardial surfaces of the solution domain

```
fem define time;r;left_group6_stimulus
fem define time;r;right_group6_stimulus
fem define time;r;left_group7_stimulus
fem define time;r;right_group7_stimulus
fem define time;r;left_group8_stimulus
fem define time;r;right_group8_stimulus
fem define time;r;left_group9_stimulus
fem define time;r;right_group9_stimulus
fem define time;r;left_group10_stimulus
fem define time;r;right_group10_stimulus

fem define init;r;biline class 1,2

fem define solv;r;biline class 1

fem define solv;r;biline2 class 2

fem export node;biline as cube reg 1

fem export elem;biline grid_numbers as cube reg 1

fem export node;cleavage_heavy_handed_shifted as
   cleavage reg 2

fem export elem;cleavage_heavy_handed_shifted as
   cleavage reg 2

fem solve to 0 class 1,2

fem export elem;"gridfield_class1_000" field class 1

fem export elem;"gridfield_class2_000" field class 2

foreach $count ( '001'..'100' ){

  my $time = $count/10;

  fem solve restart to "$time" class 1,2

  fem export elem;"gridfield_class1_$count" field class 1

  fem export elem;"gridfield_class2_$count" field class 2

  print "time: $time\n";
}
```

Read in all the time-dependent boundary conditions, and set the point at which extracellular potential is zero.

Define the solver type to use for solving transmembrane and extracellular potentials (ie. conjugate gradient method).

Export the nodes and elements of region 1 in a form able to be read by the front end CMGUI graphics display

Export the nodes and elements of region 2 in a form able to be read by the front end CMGUI graphics display

Assemble solution matrices and solve for the initial potentials.

Export the transmembrane (class 1) and extracellular (class 2) potentials at time zero.

Solve the system of equations for 0 to 10ms, in steps of 0.1ms, exporting the potential fields at each time step.

References

Al-Saidi, I.A. 2001. Using a simple method: conversion of a Gaussian laser beam into a uniform beam. *Optics & Laser Technology* 33: 75-79.

Allessie, M.A., F.I. Bonke, F.J. Schopman. 1997. Circus movement in rabbit atrial muscle as a mechanism of tachycardia. III. The "leading circle" concept: a new model of circus movement in cardiac tissue without the involvement of an anatomical obstacle. *Circulation Research*. 41(1):9-18.

Arieli, A., D. Shoham, R. Hildesheim, A. Grinvald 1995. Coherent spatiotemporal patterns of ongoing activity revealed by real- time optical imaging coupled with single- unit recording in the cat visual cortex. *J. Neurophysiol*. 73:2072-2093.

Arnar, D.O., J.R. Bullinga, J.B. Martins. 1997. Role of the Purkinje system in spontaneous ventricular tachycardia during acute ischemia in a canine model. *Circ.* 96(7):2421-2429.

Augenstein, K.F., E.R. McVeigh and A.A. Young. 2001. Magnetic resonance imaging and ventricular mechanics. *Phil. Trans. R. Soc. Lond.* A359:1263-1275.

Bai, Q., K.D. Wise, D.J. Anderson. 2000. A high-yield microassembly structure for three-dimensional microelectrode arrays. *IEEE Trans. Biomed. Eng*. 47:281-289.

Baxter, W.T., J.M. Davidenko, L.M. Loew, J.P. Wuskell, and J. Jalife. 1997. Technical features of a CCD video camera system to record cardiac fluorescence data. *Ann. Biomed. Eng.* 25:713-725.

Baxter, W.T. 1999. Intramural optical recordings of cardiac electrical activity via transillumination. *PhD thesis*. State University of New York.

Baxter, W.T., S.F. Mironov, A.V. Zaitsev, J. Jalife, and A.M. Pertsov. 2001. Visualizing excitation waves inside cardiac muscle using transillumination. *Biophys. J.* 80:516-530.

Beeler, G.W. and H. Reuter. 1977. Reconstruction of the action potential of ventricular myocardial fibres. *J. Physiol. (Lond.).* 268:177-210.

Bolognese, P., J.I. Miller, I.M. Heger, T.H. Milhorat. 1993. Laser-Doppler flowmetry in neurosurgery. *J. Neurosurg. Anesthesiol.* 5:151-158.

Bonhoeffer, T., A. Grinvald. 1991. Iso-orientation domains in cat visual cortex are arranged in pinwheel- like patterns. *Nature* 353:429-431.

Buist, M.L. 2001. Modelling cardiac activation from cell to body surface. *PhD Thesis*, University of Auckland.

Campbell, P.K., K.E. Jones, R.A. Normann. 1990. A 100 electrode intracortical array: structural variability. *Biomed. Sci. Instrum.* 26:161-165.

Campbell, P.K., K.E. Jones, R.J. Huber, K.W. Horch, R.A. Normann. 1991. A silicon-based, three-dimensional neural interface: manufacturing process for an intracortical electrode array. *IEEE Trans. Biomed. Eng.* 38:758-768.

Cannestra, A.F., S.Y. Bookheimer, N. Pouratian, A. O'Farrell, N. Sicotte, N.A. Martin, D. Becker, G. Rubino, A.W. Toga. 2000. Temporal and topographical charcterization of language cortices using intraoperative optical intrinsic signals. *Neuroimage.* 12:41-54.

Chen, J.W., A.M. O'Farrell, A.W. Toga. 2000. Optical intrinsic signal imaging in a rodent seizure model. *Neurology* 55:312-315.

Chen, P-S., P.D. Wolf, E.G. Dixon, N.D. Danieley, D.W. Frazier, W.M. Smith, R.E. Ideker. 1988. Mechanism of ventricular vulnerability to single premature stimuli in open-chest dogs. *Circ. Res.* 62:1191-1209.

Clancy, C.E., Y. Rudy. 1999. Linking a genetic defect to its cellular phenotype in a cardiac arrhythmia. *Nature* 400(6744):566-9.

Clerc, L. 1976. Directional differences of impulse spread in trabecular muscle from mammalian heart. *J. Physiol.* 255:335-346.

Cohen, L.B., R.D. Keynes, B. Hille. 1968. Light scattering and birefringence changes during nerve activity. *Nature* 218:438-441.

Davidenko, J.M., A.V. Pertsov, R. Salomonsz, W. Baxter, J. Jalife. 1992. Stationary and drifting spiral waves of excitation in isolated cardiac muscle. *Nature.* 355(6358): 349-351.

Di Persio, D.A. and R.C. Barr. 1987. A prototype inverse solution in one-dimension to find the origin of excitation, strand radius, intracellular resistivity, or distance from the surface. *IEEE Trans. Biomed. Eng.* 34(9):681-691.

Dillon S.M., T.E. Kerner, J. Hoffman, V. Menz, K.S. Li, J.J. Michele. 1998. A system for in-vivo cardiac optical mapping. *IEEE. Eng. Med. Biol.* 17(1):95-108.

Drouhard, J.P., and F.A. Roberge. 1982. A simulation study of the ventricular myocardial action potential. *IEEE Trans. Biomed. Eng.* 29:494-502.

Durrer, D., and L.H. van der Tweel. 1953. Spread of activation in the left ventricular wall of the dog. I. *Am. Heart J.* 683-691.

Durrer, D., L.H. van der Tweel, J.R. Blickman. 1954. Spread of activation in the left ventricular wall of the dog. III. Transmural and intramural analysis. *Am Heart J.* 48:13-35.

Efimov, I.R., B. Ermentrout, D.T. Huang, G. Salama. 1996. Activation and repolarisation patterns are governed by different structural characteristics of ventricular myocardium: experiental study with voltage-sensitive dyes and numerical simulations. *J Cardiovasc. Electrophysiol.* 7:512-530.

Efimov, I.R., J.F. Gerard, Y. Cheng, D.R. Van Wagoner, P.J. Tchou, T.N. Mazgalev. 1997. High-resolution fluorescent imaging does not reveal a distinct atrioventricular nodal anterior input channel (fast pathway) in the rabbit heart during sinus rhythm. *J. Cardiovasc. Electrophys.* 8(3): 295-306.

Efimov, I.R., Y. Cheng, D.R. Van Wagoner, T. Mazgalev, P.J. Tchou. 1998. Virtual electrode-induced phase singularity. A basic mechanism of defibrillation failure. *Circ. Res.* 82:918-925.

Efimov, I.R., and M. Biermann, D. Zipes. Fast fluorescent mapping of electrical activity in the heart: practical guide to experimental design and applications. In: *Cardiac Mapping*. Futura Publishing Co., *in press*.

Ellis, W.S., D.M. Auslander, M.D. Lesh. 1995. Fractionated electrograms from a computer model of heterogeneously uncoupled anisotropic ventricular myocardium. *Circulation* 92:1619-1626.

Ellis, W.S., S.J. Eisenberg, D.M. Auslander, M.W. Dae, A. Zakhor, M.D. Lesh. 1996. Deconvolution: a novel signal processing approach for determining activation time from fractionated electrograms and detecting infarcted tissue. *Circulation* 94:2633-2640.

Entcheva, E., J. Eason, I.R. Efimov, Y. Cheng, R. Malkin, F. Claydon. 1998. Virtual electrode effects in transvenous defibrillation- modulation by structure and interface: evidence from bidomain simulations and optical mapping. *Cardiovasc. Electrophysiol.* 9:949-961.

Fast, V.G., A.G. Kleber. 1995. Block of impulse propagation at an abrupt tissue expansion: evaluation of the critical strand diameter in 2- and 3-dimensional computer models. *Cardiovasc. Res.* 30:449-459.

Fast, V.G., S. Rohr, A.M. Gillis, A.G. Kleber. 1998. Activation of cardiac tissue by extracellular electrical shocks. Formation of 'secondary sources' at intercellular clefts in monolayers of cultured myocytes. *Circ. Res.* 82:375-385.

Fast, V.G., S. Rohr, R.E. Ideker. 2000. Nonlinear changes of transmembrane potential caused by defibrillation shocks in strands of cultured myocytes. *Am. J. Physiol.* 278(3):H688-H697.

Fenesis, H. 1943. Da gefüge des herzmuskels bei systole und diastole. *Morphologisches Jahrbuch* 89(4):371-406.

Fishler, M.G. 1998. Syncytial heterogeneity as a mechanism underlying cardiac far-field stimulation during defibrillation-level shock. *J. Cardiovasc. Electrophysiol.* 9:384-394.

Fluhler, E., V.G. Burnham, L.M. Loew. 1985. Spectra, membrane binding, and potentiometric responses of new charge shift probes. *Biochemistry* 24:5749-5755.

Frazier, D.W., W. Krassowska, P.-S. Chen, P.D. Wolf, N.D. Danieley, W.M. Smith, R.E. Ideker. 1988. Transmural activations and stimulus potentials in three-dimensional anisotropic canine myocardium. *Circ. Res.* 63:135-146.

Ganapathy, N., J.W. Clark Jr., O.B. Wilson, W. Giles. 1985. Forward and inverse potential field solutions for cardiac strands of cylindrical geometry. *IEEE Trans. Biomed. Eng.* 32(8):566-577.

Gardner, P., P. Ursell, J. Fenoglio, A. Wit. 1985. Electrophysiologic and anatomic basis for fractionated electrograms recorded from healed myocardial infarcts. *Circulation* 69:369-381.

Garrey, W.E. 1914. The nature of fibrillary contraction of the heart – its relation to tisse mass and form. *Am. J. Physiol.* 33:397-414.

Geselowitz, D.B., R.C. Barr, M.S. Spach, W.T. Miller, III. 1982. The impact of adjacent isotropic fluids on electrograms from anisotropic cardiac muscle. A modeling study. *Circ. Res.* 51:602-613.

Gillis, A.M., V.G. Fast, S. Rohr, A.G. Kleber. 1996. Spatial changes in transmembrane potential during extracellular electrical shocks in cultured monolayers of neonatal rat ventricular myocytes. *Circ. Res.* 79:676-690.

Gillis, A.M., V.G. Fast, S. Rohr, A.G. Kleber. 2000. Mechanism of ventricular defibrillation. The role of tissue geometry in the changes in transmembrane potential in patterned myocyte cultures. *Circ.* 101:2438-2445.

Girouard, S.D., K.R. Laurita, D.S. Rosenbaum. 1996. Unique properties of cardiac action potentials recorded with voltage-sensitive dyes. *J. Cardiovasc. Electrophysiol.* 7(11):1024-1038.

Gratton, G., M.R. Goodman-Wood, M. Fabiani. 2001. Comparison of neuronal and hemodynamic measures of the brain response to visual stimulation: An optical imaging strudy. *Hum. Brain. Mapp.* 13:13-25.

Gray, R.A., A.M. Pertsov, J. Jalife. 1998. Spatial and temporal organization during cardiac fibrillation. *Nature.* 392(5):75-78.

Gray, R.A., J. Jalife. 1998. Ventricular fibrillation and atrial fibrillation are two different beasts. *Chaos* 8(1):65-78

Gray, R.A., I. Banville. Video imaging of fibrillation and defibrillation. In: *Quantitative Cardiac Electrophysiology*. Editors: Cabo C. and D.S. Rosenbaum, *in press*.

Grinvald, A., R.D. Frostig, R.M. Siegel, E. Bartfield. 1991. High-resolution optical mapping of functional brain architecture in the awake monkey. *Proc. Natl. Acad. Sci.* 88:11559-11563.

Hamamatsu Photonics. 1997. Photodiodes (catalogue). Japan.

Hennigan, T.W., T.G. Allen-Mersh. 1994. Duration of blood flow reduction to normal liver tissue induced by angiotensin, vasopressin and endothelin. *Eur. J. Surg. Oncol.* 20:446-448.

Henriquez, C.S. 1993. Simulating the electrical behavior of cardiac tissue using the bidomain model. *Crit. Rev. Biomed. Eng.* 21(1):1-77

Hill, D., R.D. Keynes. 1949. Opacity changes in stimulated nerve. *J. Physiol.* 108:278-281.

Hodgets, N. 1996. Laminar structure of the porcine ventricles. *Masters Thesis*, University of Auckland.

Holden, A.V. 1998. A last wave from the dying heart. *Nature* 392(5):20-21.

Hoogerwerf, A.C., K.D. Wise. 1994. A three-dimensional microelectrode array for chronic neural recording. *IEEE Trans. Biomed. Eng.* 41:1136-1146.

Hooks, D.A., I.J. LeGrice, J.D. Harvey, B.H. Smaill. 2001. Intramural multisite recording of transmembrane potential in the heart. *Biophys. J.* 81:2671-2680.

Hort, W. 1957. Mikrometrische untersuchungen an verschieden weiten meerschweinchenherzen. *Verhandl. Deut. Ges. Kreislaufforsch.* 23:343-346.

Hort, W. 1960. Makroskopische und mikrometrische untersuchungen am myokard verschieden stark gefüllter linker kammern. *Virchows Arch. Path. Anat.* 333:523-564.

Hunter, P.J., P.A. McNaughton, D. Noble. 1975. Analytical models of propagation in excitable cells. *Prog. Biophys. Molec. Biol.* 30(2/3):99-144.

Hunter, P.J., B.H. Smaill, P.M.F. Nielsen, I.J. LeGrice. 1997. A mathematical model of cardiac anatomy. In: *Computational Biology of the Heart*. John Wiley & Sons Ltd. New York. Ch6:183-187.

Janesick, J.R., K.P. Klaasen, T. Elliott. Charge-coupled-device charge-collection efficiency and the photon-transfer technique. 1987. *Opt Eng* 26(10):972-980.

Keener, J.P. 1988. On the formation of circulating patterns of excitation in anisotropic excitable media. *J. Math. Biol.* 26:41-56.

Kerber, R.E., K.T. Spencer, M.J. Kallok, C. Birkett, R. Smith, D. Yoerger, R.A. Kieso. 1994. Overlapping sequential pulses. A new waveform for transthoracic defibrillation. *Circ.* 89(5):2369-2379.

Kléber, A.G. and C.B. Riegger. 1987. Electrical constants of arterially perfused rabbit papillary muscle. *J. Physiol.* 385:307-324.

Knisley, S.B. 1995. Transmembrane voltage changes during unipolar stimulation of rabbit ventricle. *Circ. Res.* 77:1229-1239.

Knisley, S.B., and T.C. Baynham. 1997. Line stimulation parallel to myofibres enhances regional uniformity of transmembrane voltage changes in rabbit hearts. *Circ. Res.* 81:229-241.

Knisley, S.B., N. Trayanova, F. Aguel. 1999. Roles of electric field and fiber structure in cardiac electric stimulation. *Biophys. J.* 77:1404-1417.

Knisley, S.B., R.K. Justice, W. Kong, P.L. Johnson. 2000. Ratiometry of transmembrane voltage-sensitive fluorescent dye emission in hearts. *Am. J. Physiol. Heart Circ. Physiol*. 279(3):H1421-1433.

Kohl, P., P. Hunter, D. Noble. 1999. Stretch-induced changes in heart rate and rhythm: clinical observations, experiments and mathematical models. *Prog. Biophys. and Mol. Biol.* 71:91-138.

Krassowska, W., D.W. Frazier, T.C. Pilkington, R.E. Ideker. 1990. Potential distribution in three-dimensional periodic myocardium – Part II: application to extracellular stimulation. *IEEE Trans.on Biomed. Eng.* 37(3):267-284.

Krauthamer, V., H.J. Bryant, C.C. Davis, T.W. Athey. 1991. Action potential-induced fluorescence changes resolved with an optical fiber carrying excitation light. *J. Fluorescence.* 1(4):207-213.

Krauthamer, V., C.C. Davis, E. Gan. 1994. Two-point electrical-fluorescence recording from heart with optical fibers. *IEEE Trans. Biomed. Eng.* 41(12):1191-1195.

Kucera, J.P., A.G. Kleber, S. Rohr. 1998. Slow conduction in cardiac tissue, II. Effects of branching tissue geometry. *Circ. Res.* 83:795-805.

Lam, J.M., J.N. Hsiang, W.S. Poon. 1997. Monitoring of autoregulation using laser Doppler flowmetry in patients with head injury. *J. Neurosurg.* 86:438-445.

LeGrice, I.J. 1992. *PhD Thesis.* University of Auckland, New Zealand.

LeGrice, I.J., B.H. Smaill, L.Z. Chai, S.G. Edgar, J.B. Gavin, P.J. Hunter. 1995. Laminar structure of the heart: Ventricular myocyte arrangement and connective tissue architecture in the dog. *Am. J. Physiol.* 38:H571-H582.

Leonard, B.L, R.G. Evans, M.A. Navakatikyan, S.C. Malpas. 2000. Differential neural control of intrarenal blood flow. *Am. J. Physiol.* 279:R907-R916.

Leonard, B.L., S.C. Malpas, K.M. Denton, A.C. Madden, R.G. Evans. Neural control of intrarenal blood flow during hypoxia. *Am J. Physiol., in press.*

Lewis, T. 1915. *Lectures on the heart.* Paul B. Hoeber. New York.

Lipsius, S.L., J. Huser, L.A. Blatter. 2001. Intracellular Ca^{2+} release sparks atrial pacemaker activity. *NIPS* 16:101-106.

Mines, G.R. 1914. On circulating excitations in heart muscles and their possible relation to tachycardia and fibrillation. *Trans. R. Soc. Can.* 4:43-52.

Mironov, S., M. Vinson, S. Mulvey, A. Pertsov. 1996. Destabilization of three-dimensional rotating chemical waves in an inhomogeneous BZ reaction. *J. Phys. Chem*. 100:1975-1983.

Muzikant, A.L., C.S. Henriquez. 1998. Bipolar stimulation of a three-dimensional bidomain incorporating rotational anisotropy. *IEEE Trans on Biomed Eng* 45(4):449-463.

Najafi, K., J. Ji, K.D. Wise. 1990. Scaling limitations of silicon multichannel recording probes. *IEEE Trans. Biomed. Eng*. 37:1-11.

Neunlist, M., S. Zou, L. Tung. 1992. Design and use of an "optrode" for optical recordings of cardiac action potentials. *Pflugers Arch.* 420:611-617.

Nicolelis, M.A., A.A. Ghazanfar, B.M. Faggin, S. Votaw, L.M. Oliveira. 1997. Reconstructing the engram: simultaneous, multisite, many single neuron recordings. *Neuron.* 18:529-537.

Opie, L.H. 1998. *The heart. Physiology from cell to circulation*. Lippincott-Raven, Philadelphia. p590.

Paradis, N., H.R. Halperin, R.N. Nowaq. 1996. *Cardiac Arrest: The science and practise of resuscitation medicine.* Williams and Wilkins, Baltimore

Pawley, J.B. 1995. *Handbook of biological confocal microscopy*. Plenum Press, New York.

Plonsey, R. and R.C. Barr. 1987. Interstitial potentials and their change with depth into cardiac tissue. *Biophys. J.* 51:547-555.

Plonsey, R. and R.C. Barr. 1988. *Bioelectricity: a quantitative approach*. Plenum Press, New York.

Pouratian, N., S.Y. Bookheimer, A.M. O'Farrell, N.L. Sicotte, A.F. Cannestra, D. Becker, A.W. Toga. 2000. Optical imaging of bilingual cortical representations. Case report. *J. Neurosurg.* 93:676-681.

Pu, J. and H. Zhang. 1998. Aberrated lenses for generating flattened laser irradiance. *Appl. Optics* 37(19): 4200-4205.

Robb, J.S., R.C. Robb. 1942. The normal heart. Anatomy and physiology of the structural units. *Am. Heart J.* 23:455-467.

Roberts, D.E. and A.M. Scher. 1982. Effect of tissue anisotropy on extracellular potential fields in canine myocardium in situ. *Circ. Res.* 50:342-351.

Rohr, S., J.P. Kucera, V.G. Fast, A.G. Kleber. 1997. Paradoxical improvement of impulse conduction in cardiac tissue by partial cellular uncoupling. *Science* 275(7):841-844.

Rohr, S., and J.P. Kucera. 1998. Optical recording system based on a fiber optic image conduit: assessment of microscopic activation patterns in cardiac tissue. *Biophys. J.* 75:1062-1075.

Roth, B.J. 1997. Electrical conductivity values used with the bidomain model of cardiac tissue. *IEEE Trans. Biomed. Eng.* 44(4):326-328.

Rousche, P.J., R.A. Normann. 1998. Chornic recording capability of the Utah Intracortical Electrode Array in cat sensory cortex. *J. Neurosci. Meth.* 82:1-15.

Russ, J.C. 1995. *The image processing handbook.* CRC Press Inc. Ch9.

Sands, G. 1996. Mathematical model of ventricular activation in an anatomically accurate deforming heart. *PhD Thesis*, University of Auckland.

Sands, G., D.A. Hooks, I.J. LeGrice, B.H. Smaill. 1999. Three-dimensional spread of electrical activity in ventricular myocardium. *Faseb J.* 13(5) PartII:A1075

Schlosser, B., F. Rucker, R. Hiendl, G. ten Bruggencate, B. Sutor. 1996. Spatial pattern of evoked synaptic excitation in the mouse neostriatum in vitro. *Exp. Brain Res.* 112:452-461.

Schmitt, O.H. 1969. Biological information processing using the concept of interpenetrating domains. In: *Information Processing in the Nervous System*. Springer-Verlag. New York.

Selvester, R.H., W.L. Kirk, Jr, R.B. Pearson. 1970. Propagation velocities and voltage magnitudes in local segments of dog myocardium. *Circ. Res.* 27:619-629.

Sepulveda, N.G., and J.P. Wikswo, Jr. 1987. Electric and magnetic fields from two-dimensional anisotropic bisyncytia. *Biophys. J.* 51:557-568.

Shenasa M., M. Borggrefe, G. Breithardt. 1993. *Cardiac Mapping*. Futura Publishing Company, Inc. New York.

Shim, M.G., B.C. Wilson, E. Marple and M. Wach. 1999. Study of fiber-optic probes for *in vivo* medical raman spectroscopy. Appl. Spectroscopy 53(6):619-627.

Shmuel, A., A. Grinvald. 2000. Coexistence of linear zones and pinwheels within orientation maps in cat visual cortex. *Proc. Natl. Acad. Sci.* 97:5568-5573.

Shoham, D., D.E. Glaser, A. Arieli, T. Kenet, C. Wijnbergen, Y. Toledo, R. Hildesheim, A. Grinvald. 1999. Imaging cortical dynamics at high spatial and temporal resolution with novel blue voltage-sensitive dyes. *Neuron* 24:791-802.

Shtoyerman, E., A. Arieli, H. Slovin, I. Vanzetta, A. Grinvald. 2000. Long-term optical imaging and spectroscopy reveal mechanisms underlying the intrinsic signal and stability of cortical maps in V1 of behaving monkeys. *J. Neuroscience.* 20:8111-8121.

Skouibine, K.B., N.A. Trayanova, P.K. Moore. 1999. Anode/cathode make and break phenomena in a model of defibrillation. *IEEE Trans. Biomed. Eng.* 46(7):769-777.

Sobie, E.A., R.C. Susil, L. Tung. 1997. Generalized activating function for predicting virtual electrodes in cardiac tissue. *Biophys. J.* 73:1410-1423.

Spach, M.S., R.C. Barr, G.A. Serwer, J.M. Kootsey, E.A. Johnson. 1972. Extracellular potentials related to intracellular action potentials in the dog purkinje system. *Circ. Res.* 30(5):505-519.

Spach M.S., W.T. Miller, E. Miller-Jones, R.B. Warren, R.C. Barr. 1979. Extracellular potentials related to intracellular action potentials during impulse conduction in anisotropic canine cardiac muscle. *Circ. Res.* 45:188-204.

Spach, M.S., and P.C. Dolber. 1986. Relating extracellular potentials and their derivatives to anisotropic propagation at a microscopic level in human cardiac muscle: evidence for electrical uncoupling of side-to-side fiber connections with increasing age. *Circ. Res.* 58:356-371.

Sperelakis, N., and R.O. Banks. 1996. *Essentials of Physiology*, 2nd edn, Little Brown & Co.

Spitzer M.W., M.B. Calford, J.C. Clarey, J.D. Pettigrew, A.W. Roe. 2001. Spontaneous and stimulus-evoked intrinsic optical signals in primary auditory cortex of the cat. *J. Neurophysiol.* 85:1283-1298.

Spotnitz, H.M., W.D. Spotnitz, T.S. Cottrell, D. Spiro, E.H. Sonnenblick. 1974. Cellular basis for volume related wall thickness changes in the rat left ventricle. *Jnl. Mol. Cell Cardiol.* 6:317-331.

Steinhaus, B.M. 1989. Estimating cardiac transmembrane activation and recovery times from unipolar and bipolar extracellular electrograms: a simulation study. *Circ. Res.* 64:449-462.

Stern, M.D. 1975. In vivo evaluation of microcirculation by coherent light scattering. *Nature.* 254:56-58.

Streeter, D.D. Jr., D.L. Bassett. 1966. An engineering analysis of myocardial fiber orientation in pig's left ventricle in systole. *Anat. Rec.* 155:503-511

Sutor, B., J.J. Hablitz, F. Rucker, G. ten Bruggencate. 1994. Spread of epileptiform activity in the immature rat neocortex studied with voltage-sensitive dyes and laser s-canning microscopy. *J. Neurophysiol.* 72:1756-1768.

Trayanova, N. 1996. Discrete versus syncytial tissue behavior in a model of cardiac stimulation-II: Results of simulation. *IEEE Trans. Biomed. Eng.* 43(12):1141-1150.

Trayanova, N., K. Skouibine. 1998. Modelling defibrillation: effects of fiber curvature. *J. Electrophys.* 31(Suppl.):23-29.

Trayanova, N. 1999. Far-field stimulation of cardiac tissue. *Herzschr. Elektrophys.* 10:137-148.

Vaadia, E., D.A. Benson, R.D. Hienz, M.H. Goldstein, Jr. 1986. Unit study of monkey frontal cortex: active localization of auditory and of visual stimuli. *J. Neurophysiol*. 56:934-952.

van Horne, C.G., S. Bement, B.J. Hoffer, G.A. Gerhardt. 1990. Multichannel semiconductor-based electrodes for in vivo electrochemical and electrophysiological studies in rat CNS. *Neurosci. Lett.* 210:249-252.

Vetter, F.J., A.D. McCulloch. 1998. Three-dimensional analysis of regional cardiac function: a model of rabbit ventricular anatomy. *Prog. Biophys. Mol. Biol.* 62(2-3):157-183.

Weber, K.T., J.S. Janicki, R. Pick, J. Capasso, P. Anversa. 1990. Myocardial fibrosis and pathologic hypertrophy in the rat with renovascular hypertension. *Am. J. Cardiol.* 65:1G-7G.

Weidmann, S. 1970. Electrical constants of trabecular muscle from mammalian heart. *J. Physiol.* 210:1041-1054.

Weitz, G. 1951. Über das unterschiedliche verhalten der lage der herzmuskelfasern in kontrahiertem und dilatierem zustand. *Med. Klin. Munich* 46:1031-1032.

Wikswo, J.P. Jr., S-F. Lin, R.A. Abbas. 1995. Virtual electrodes in cardiac tissue: a common mechanism for anodal and cathodal stimulation. *Biophys. J.* 69:2195-2210.

Winfree, A.T., S. Caudle, G. Chen, P. McGuire, Z. Szilagyi. 1996. Quantitative optical tomography of chemical waves and their organizing centers. Chaos. 6(4):617-626.

Witkowski, F.X., L.J. Leon, P.A. Penkoske, R.B. Clark, M.L. Spano, W.L. Ditto, W.R. Giles. 1998(a). A method for visualizatin of ventricular fibrillation: Design of a

cooled fiberoptically coupled image intensified CCD data acquisition system incorporating wavelet shrinkage based adaptive filtering. *Chaos*. 8(1): 94-102.

Witkowski, F.X., L.J. Leon, P.A. Penkoske, R.B. W.R. Giles, M.L. Spano, W.L. Ditto, A.T. Winfree. 1998(b). Spatiotemporal evolution of ventricular fibrillation. *Nature*. 392(5):73-82.

Yoon, T.H., E.J. Hwang, D.Y. Shin, S.I. Park, S.J. Oh, S.C. Jung, H.C. Shin, S.J. Kim. 2000. A micromachined silicon depth probe for multichannel neural recording. *IEEE Trans. Biomed. Eng.* 47:1082-1087.

Young, A.A., I.J. LeGrice, M.A. Young, B.H. Smaill. 1998. Extended confocal microscopy of myocardial laminae and collagen network. *J. Microscopy* 192(2):139-150.

Zienkiewicz, O.C., R.L. Taylor. 1994. *The Finite Element Method*, 4th edn, McGraw-Hill, Berkshire.

Zhou, X., Ideker, R.E., Blitchington, T.F., Smith, W.M., Knisley, S.B. 1995. Optical transmembrane potential measurements during defibrillation-strength shocks in perfused rabbit hearts. *Circ. Res.* 77:593-602.

Zhu, Z.Y., and M.C. Yappert. 1992. Determination of effective depth and equivalent pathlength for a single-fiber fluorometric sensor. *Appl. Spectroscopy.* 46(6):912-918.

Zipes and Jalife. 2000. *Cardiac Electrophysiology: from Cell to Bedside*, 3rd edn, W.B. Saunders Company, Pennsylvania.